Daniela Donhauser

Correlation between Structural and Electronic Properties of Co-Evaporated Doped Organic Thin Films

Cuvillier Verlag Göttingen
Internationaler wissenschaftlicher Fachverlag

Correlation between Structural and Electronic Properties of Co-Evaporated Doped Organic Thin Films

Von der Fakultät für Elektrotechnik, Informationstechnik, Physik
der Technischen Universität Carolo-Wilhelmina zu Braunschweig

zur Erlangung des Grades einer Doktorin
der Ingenieurwissenschaften (Dr.-Ing.)

genehmigte Dissertation

von Dipl.-Phys. Daniela Donhauser

aus Nürnberg

eingereicht am: 25.10.2013
mündliche Prüfung am: 20.11.2013

1. Referent: Prof. Dr.-Ing. W. Kowalsky
2. Referent: Prof. Dr. rer. nat. R. R. Schröder

Druckjahr: 2014

Bibliografische Information der Deutschen Nationalbibliothek
Die Deutsche Nationalbibliothek verzeichnet diese Publikation in der Deutschen Nationalbibliographie; detaillierte bibliografische Daten sind im Internet über http://dnb.d-nb.de abrufbar.
1. Aufl. - Göttingen: Cuvillier, 2014
Zugl.: (TU) Braunschweig, Univ., Diss., 2014

Dissertation an der Technischen Universität Braunschweig
Fakultät Elektrotechnik, Informationstechnik, Physik

Nonnenstieg 8, 37075 Göttingen
Telefon: 0551-54724-0
Telefax: 0551-54724-21
www.cuvillier.de

1. Auflage, 2014
Gedruckt auf umweltfreundlichem, säurefreiem Papier aus nachhaltiger Forstwirtschaft.

ISBN 978-3-95404-830-4
eISBN 978-3-7369-4830-3

Danksagung

Die vorliegende Arbeit entstand im Rahmen meiner Tätigkeit als wissenschaftliche Mitarbeiterin am Institut für Hochfrequenztechnik der TU Braunschweig. Mein Dienstort war dabei das Innovationlab in Heidelberg, ein Spitzencluster für organische Elektronik, in dem verschiedene Universitäten und Industrieunternehmen zusammenarbeiten. Da zu Beginn dieser Arbeit keinerlei Laborflächen in Heidelberg vorhanden waren, konnte diese Arbeit nur in so kurzer Zeit fertig gestellt werden, weil eine Vielzahl an Leuten tatkräftig zusammengearbeitet und dabei auch eine gehörige Portion Pragmatismus und Eigeninitiative an den Tag gelegt haben. Im Folgenden möchte ich mich bei allen Leuten bedanken, die zum Gelingen dieser Arbeit beigetragen haben.

Mein Dank gilt Prof. Dr. Wolfgang Kowalsky, Leiter des Instituts für Hochfrequenztechnik, für die ausgezeichnete Betreuung dieser Arbeit und dafür, dass er immer ein offenes Ohr für mich hatte und mir ein sehr eigenverantwortliches wissenschaftliches Arbeiten ermöglicht hat. Daneben bin ich ihm für die Möglichkeit sehr dankbar, meine Ergebnisse bei einer so großen Anzahl an nationalen und internationalen Konferenzen vorzustellen. Weiterhin gilt mein Dank Prof. Dr. Rasmus R. Schröder (Universität Heidelberg) für die Übernahme der Zweitkorrektur sowie Prof. Dr. Achim Enders (TU Braunschweig) für die Übernahme des Prüfungsvorsitzes.

Dr. Michael Kröger hat überdurchschnittlich viel Zeit und Engagement in die Planung und den Aufbau des Innovationlabs und der Analytikgruppe gesteckt. Dafür und vor allem für die ausgezeichnete Betreuung dieser Arbeit möchte ich ihm sehr herzlich danken. Weiterhin gilt mein Dank Dr. Robert Lovrinčić für die hervorragende Betreuung dieser Arbeit in der Endphase.

Die vorliegende Arbeit entstand im Rahmen des BMBF-Projektes MESOMERIE. Auf experimenteller Seite waren an diesem Projekt neben dem Institut für Hochfrequenztechnik der TU Braunschweig auch das Institut für Oberflächenphysik und Infrarotspektroskopie der Universität Heidelberg, sowie das Institut für Oberflächenforschung der TU Darmstadt beteiligt. Dabei möchte ich vor allem Dr. Tobias Glaser, Maybritt Kühn und Dr. Eric Mankel für die tolle Zusammenarbeit danken, die erst dazu geführt hat, dass wir ein so umfassendes Verständnis der Dotierung von CBP mit MoO_3 erreichen konnten. Dr. Tobias Glaser und Sebastian Beck möchte ich daneben für die Herstellung der Filme auf den gekühlten Substraten danken.

Die in der vorliegenden Arbeit präsentierten TEM-Messungen entstanden an der Universität Heidelberg in Zusammenarbeit mit der Arbeitsgruppe von Prof. Dr. Rasmus R. Schröder, dem ich an dieser Stelle für die Möglichkeit danken möchten, dass ich eine so große Anzahl Messungen mit seiner Arbeitsgruppe durchführen konnte. Dr. Martin Pfannmöller, der für einen Großteil der TEM-Spektroskopie Messungen verantwortlich war, möchte ich für die vielen Stunden am Kronos danken, bei denen wir jedes mal mindestens einen Schritt weiter gekommen sind (wenn dem nicht technische Probleme entgegenstanden) und dafür, dass er mir stets geduldig alle TEM-Fragen beantwortet hat. Anne K. Kast hat sich mit sehr großem Engagement um den Großteil der Tomographiemessungen und Auswertungen gekümmert. Vielen Dank für die sehr nette und fruchtbare Zusammenarbeit. Im Bereich TEM möchte ich mich daneben auch bei Dr. Levin Dieterle und Dr. Katrin Schultheiß bedanken, die ebenfalls mit großem Engagement dazu beigetragen haben, dass wir soviele Daten über die Struktur der dotierten CBP-Filme sammeln konnten.

Für das kritische Korrekturlesen dieser Arbeit, bzw. Teilen davon, möchte ich Dr. Robert Lovrinčić, Anne K. Kast, Dr. Michael Kröger, Dr. Tobias Glaser und Maybritt Kühn danken.

Ebenso gebührt auch allen Studenten großer Dank für ihr Engagement sowohl beim Laboraufbau (vor allem in der Anfangszeit des iL), als auch bei ihrer wissenschaftlichen Arbeit. Namentlich genannt werden sollen hier Benjamin Martini, Markus Gölz, Alexander Müller-Brand, Ilja Vladimirov, Johannes Ostermann und Dominik Daume.

Meinem Kollegen Dr. Thomas Winkler danke ich für die tolle Einarbeitung in Braunschweig während der ersten Wochen meiner Promotion, die mir den Aufbau der Labore in Heidelberg sehr vereinfacht hat.

Allen meinen iL-Kollegen möchte ich ganz herzlich für die tolle Zeit am Innovationlab danken. Leider kann ich an dieser Stelle nicht alle aufzählen, möchte aber neben den oben bereits Genannten an dieser Stelle noch besonders Rebecca Saive, Christoph Leonhard, Janusz Schinke, Julia Maibach, Diana Nanova und Michaela Sauer erwähnen.

Meinen Eltern, ohne die ich nie soweit gekommen wäre, danke ich dafür, dass sie in jeder Lebenslage für mich da sind. Zu guter Letzt möchte ich noch meinem Freund Kay Egloff, neben der Hilfe bei der Bildbearbeitung, vor allem für seine liebevolle Unterstützung während meiner gesamten Promotion danken.

Kurzfassung

Bei Bauteilen auf Basis von organischen Halbleitern, wie zum Beispiel organischen Leuchtdioden (engl. organic light emitting diode, OLED) oder organischen Solarzellen, werden häufig elektrochemisch dotierte Transportschichten eingesetzt, wodurch die Betriebsspannung verringert werden kann. Auch wenn sich damit heutzutage sehr effiziente Bauteile realisieren lassen, fehlt eine umfassende Beschreibung der physikalischen Prozesse die der elektrochemischen Dotierung zu Grunde liegen. Beispielsweise wurde für eine Vielzahl an Materialsystemen gezeigt, dass die Dotiereffizienz, d.h. das Verhältnis von eingebrachten Dotanten und der Anzahl der erzeugten freien Ladungsträger, oft nur wenige Prozent beträgt. In der vorliegenden Arbeit wird als Modellsystem der organische Halbleiters CBP (4,4'-Bis(N-carbazolyl)-1,1'-biphenyl) dotiert mit dem Übergangsmetalloxid Molybdänoxid (MoO_3) verwendet, um der Frage nachzugehen, worin der Ursprung für die geringe Dotiereffizienz liegt.

Eine mögliche Erklärung wäre eine Agglomeration der Dotanten. Um Informationen über die strukturellen Eigenschaften der dotierten Filme zu erhalten, wurden verschiedene Messmodi der Transmissionselektronenmikroskopie (TEM) eingesetzt. Mittels TEM-Spektroskopie in zwei verschiedenen Energieregimen konnte nachgewiesen werden, dass MoO_3 agglomeriert, wenn es mit CBP koverdampft wird. Elektronentomographie zeigte eine filamentartige Struktur der MoO_3-Agglomerationen, bei der die Fäden bevorzugt senkrecht zum Substrat aufwachsen. Die Länge der Fäden kann dabei über die Substrattemperatur während des Aufdampfprozesses kontrolliert werden.

Weiterhin konnte gezeigt werden, dass die Anisotropie bezüglich der Topologie auch mit einer Anisotropie in den elektrischen Eigenschaften einhergeht. Zwei verschiedene Bauteilstrukturen wurden hergestellt, bei denen der Ladungstransport entlang und senkrecht zu den Fäden untersucht werden konnte. Es zeigte sich, dass sowohl Leitfähigkeit als auch Aktivierungsenergie richtungsabhängig sind.

Die Erkenntnisse über die Topologie der dotierten Filme, sowie ihre elektrischen Eigenschaften, wurden mit Messungen der elektronischen Struktur mittels Fourier-Transform-Infrarotspektroskopie und Photoelektronenspektroskopie (PES) verknüpft. Auf der Basis all dieser Ergebnisse wurde ein Modell entwickelt, das den Ladungstransport der dotierten Schichten in Abhängigkeit von der Dotierkonzentration beschreibt.

Neben den Untersuchungen zur p-Dotierung mittels Koverdampfung wurde im letzten

Teil der Arbeit die n-Dotierung betrachtet. Dabei wurde der Dotant LiF als dünner Film zwischen dem organischen Film und der Metallkathode aufgedampft. Die Bauteileigenschaften von OLEDs mit TPBi (1,3,5-tris (2-N-phenylbenzimidazolyl) benzene) als Elektronenleiter und einer LiF-Zwischenschicht wurden in Abhängigkeit des Aufdampfwinkels untersucht. Im Vergleich zu OLEDs die bei $0°$ oder $42°$ hergestellt wurden konnte für OLEDs bei $72°$ keine Lichtleisung mehr detektiert werden und die IV-Charakteristik wies darauf hin, dass die Ladungsträgerinjektion von einem der Kontakte unzureichend war. Daher wurde der LiF/TPBi-Kontakt mittels PES untersucht und eine, im Vergleich zum reinen TPBi, abnehmende Ferminiveauverschiebung in Richtung des TPBi LUMO (engl. lowest unoccupied molecular orbital) mit größer werdendem Depositionswinkel gemessen. Diese Beobachtung weist darauf hin, dass der Grad der n-Dotierung mit steigendem Aufdampfwinkel abnimmt, was die Fehlfunktion der OLED erklären kann.

Abstract

Devices based on organic semiconductors, like organic light emitting diodes (OLEDs) or organic solar cells, often comprise electrochemically doped charge transport layers, which lower the operating voltage of these devices. Although very efficient devices can be realized nowadays, a comprehensive description of the physical processes taking place in electrochemically doped thin films is still missing. For instance, it was shown for a variety of different material systems that the doping efficiency, defined as the number of free charge carriers compared to the number of incorporated dopants, often amounts to only a few per cent. In the present thesis, the organic semiconductor CBP (4,4'-Bis(N-carbazolyl)-1,1'-biphenyl), doped with the transition metal oxide molybdenum oxide (MoO_3), is used as a model system to investigate the origin for this low doping efficiency.

One explanation for the low doping efficiencies would be clustering of the dopants. To gain information about the structure of the doped films, different measurement modes of transmission electron microscopy (TEM) were applied. Using TEM spectroscopy in two different energy regimes, it could be proven that MoO_3 agglomerates, when it is co-evaporated with CBP. Electron tomography revealed filamentous structures, with filaments preferentially oriented perpendicular to the substrate. Furthermore, it was shown that the length of the filaments can be controlled by the substrate temperature during film deposition.

The structural anisotropy was found to correlate with an electrical anisotropy. Two different device structures were fabricated which allowed for measuring current transport parallel and perpendicular to the filaments and conductivity as well as activation energy were found to be direction-dependent.

The findings about the topology of doped films, as well as their electrical properties, were correlated with measurements of the electronic properties, obtained by Fourier transform infrared spectroscopy and photoelectron spectroscopy (PES). Based on all results, a model was developed to describe charge transport in MoO_3-doped CBP films as a function of the doping concentration.

Beside the investigations about p-type doping of co-evaporated thin films, n-doping via interface doping was considered in the last part of the present thesis. Here, the dopant LiF was inserted as thin layer between organic film and the metal cathode. The device

performance of OLEDs with TPBi (1,3,5-tris (2-N-phenylbenzimidazolyl) benzene) as electron transport layer and a LiF interlayer was investigated as a function of evaporation angle. Compared to OLEDs which were fabricated at $0°$ and $42°$ deposition angle, OLEDs which were deposited at $72°$ did not emit light and IV characteristics which are typical for single-carrier devices were found. Therefore, the LiF/TPBi interface was investigated using PES. Compared to pristine TPBi, a decreasing Fermi level shift towards the TPBi LUMO (lowest unoccupied molecular orbital) was found for increasing deposition angle. This indicates weaker n-type doping for increasing deposition angle, which can explain the failure of the device.

Contents

List of Abbreviations

AFM	atomic force microscopy
BHJ	bulk heterojunction
DFT	density functional theory
DOS	density of states
EELS	electron energy loss spectroscopy
ESI	electron spectroscopic imaging
FIB	focused ion beam
FTIR	Fourier transform infrared spectroscopy
IPES	inverse photoemission
ITO	indium tin oxide
OLED	organic light emitting diode
PES	photoelectron spectroscopy
PSD	power spectral density
SEM	scanning electron microscopy
STM	scanning tunneling microscopy
TEM	transmission electron microscope
TMO	transition metal oxide
UHV	ultra high vacuum
UPS	ultraviolet photoelectron spectroscopy
XPS	x-ray photoelectron spectroscopy

1 Introduction

Since the discovery of electroluminescence in organic materials in 1955 by Bernanose[1], enormous progress has been made in enhancing efficiencies for electric devices based on organic semiconductors like organic light emitting diodes (OLEDs). The first OLED was already realized by Helfrich et al. in 1965[2]. As the antracen crystals used in this work were several microns in thickness, operating voltages of several hundred volts were required. The breakthrough came with Tang and vanSlyke, who presented the first organic light emitting thin film device based on organic small molecules deposited via thermal evaporation in 1987[3]. The bilayer structure of diamine and Alq_3[1] had operating voltages below $5\,\mathrm{V}$, making the field of organic electronics also interesting for technical applications. Since then, the efficiency increased continuously and products based on organic semiconductors finally captured the market. Nowadays, for example cell phones are equipped with OLED displays and also curved OLED TVs are already commercially available.

Even though the semiconductor industry is still dominated by inorganic materials like silicon or gallium arsenide, organic semiconductors have outstanding properties making them superior to inorganics for specific applications. They can, for instance, be processed via simple deposition techniques like thermal evaporation, spincoating or printing. Compared to inorganics, no lattice matching of the used materials is required so that deposition on almost any kind of substrate (e.g. glass or flexible plastic foils) is feasible. This offers the possibility to fabricate bendable[4] as well as translucent electrical devices[5,6]. Since an almost unlimited number of organic compounds is available and properties of these materials can quite easily be changed, for instance by modifying or adding side groups[7], it is conceivable to provide tailored materials with all kinds of functionalities.

In the early days the performance of organic devices was quite limited since intrinsic

[1] Only the abbreviations commonly used for organic semiconductors are mentioned throughout the text. The correct chemical formulae can be found in appendix A, where also the molecular structure for all materials used for experiments in this work is depicted.

organic layers exhibit very low charge carrier densities as well as low mobilities. After introducing the concept of electrochemical doping, as it is commonly used for inorganic devices, the performance of organic components could be enhanced significantly. Efficient state-of-the-art devices like small molecule organic solar cells, as well as organic light emitting diodes, are often realized by employing p-i-n structures where an intrinsic layer is sandwiched between n- and p-doped transport layers[8,9].

For electrochemical doping various concepts have been reported in literature. As first demonstrated by Shirakawa in 1977 for Polyacetylene[10], exposure to oxidizing gases like iodine, oxygen or bromine can lead to an increase of conductivity due to p-type doping[11–14]. Because for n-type doping materials with very high lying HOMO levels are required, which are very unstable against oxygen, it is more difficult to find suitable materials[8]. One approach is the use of alkali metals like lithium or cesium. They are normally deposited as a very thin film between the organic layer and the metal cathode[8,15–17], but can also be co-evaporated with the organic host material[18]. Since such small dopants can easily diffuse through the device, problems regarding stability and processability can occur[17,19].

Therefore, another approach, which leads to better device stability[8], is introducing organic molecular dopants, most commonly via co-evaporation with the organic host material. Several molecular dopants have been successfully applied in the past. Molecules used for n-type doping are, for example, TTN[20] or $CoCp_2$[21]. For p-type doping, for instance, DDQ, TCNQ[22] or F_4-TCNQ were applied, with the latter being the most prominent one. F_4-TCNQ was shown to be a very efficient dopant for a various organic materials like 1-TNATA[23], ZnPc[24], m-MTDATA[25] or VOPc[26]. Nonetheless, it turned out that F_4-TCNQ is quite inefficient for doping wide-band gap materials with very deep lying HOMO levels like CBP, α-NPD or TCTA[23]. This is probably due to the fact that the HOMO levels of these materials are significantly higher than the LUMO of F_4-TCNQ (5.24 eV[24]). Instead, transition metal oxides (TMOs) like WO_3[27], ReO_3[28], or MoO_3[29,30] were found to be a suitable material class for efficient p-type doping of materials because of their very deep lying LUMO levels.

The control of the doping process and other improvements like introducing new device architectures and materials have led to very efficient organic devices. For example, white OLEDs were recently reported to achieve over $100\ \mathrm{lm/W}$ at $1000\ \mathrm{cd/m^2}$[31]. Nonethe-

less, there is still a lack of detailed understanding of the fundamental processes which take place in organic devices.

1.1 Motivation

Although for inorganic semiconductors doping concentrations in the range of ppm are commonly used, the doping concentrations employed in organic devices are usually much higher. When F_4-TCNQ is used as dopant, a few mol% are typically applied[24,25], whereas for TMOs even up to several ten mol% doping concentration are employed[27–29,32]. It is not well understood why such high doping concentrations are needed, because a comprehensive and detailed understanding of the doping process in organic semiconductors is still missing.

For various organic-organic and organic-inorganic material systems the free charge carrier density was determined with different measurement techniques. From the charge carrier density, the doping efficiency, defined as the number of free charge carriers compared to the number of incorporated dopant molecules, can be calculated. The doping efficiency was determined for a variety of different material systems and very low doping efficiencies in the range of only a few per cent were often reported.

For polymer-small molecule systems like P3HT[33] or MEH-PPV[34] doped with F_4-TCNQ doping efficiencies of $5\ \%$ and $1\ \%$, respectively, were determined from impedance spectroscopy measurements. A low doping efficiency was also found for the small molecule-based systems α-NPD doped with $Mo(tfd)_3$ or F_4-TCNQ where impedance spectroscopy revealed a doping efficiency of $3.7\ \%$ and $0.9\ \%$, respectively[35].

In the present thesis, the material system CBP doped with MoO_3 is examined. As depicted in Figure 1.1, the HOMO of CBP ($6.23\ \mathrm{eV}$[36]) is slightly higher than the LUMO-level of MoO_3 ($6.7\ \mathrm{eV}$[36]). Therefore, an efficient charge transfer would be expected between these two materials. The values in this energy diagram were determined by ultraviolet photoelectron spectroscopy (UPS) and inverse photoemission (IPES) measurements[36]. It was found that the Fermi level shifts towards the HOMO edge with increasing doping concentration and IV measurements revealed that the conductivity increases for increasing doping concentrations[36]. Up to that point all results are expected for a doped system, but also for this material system the doping efficiency, which was determined via Kelvin-

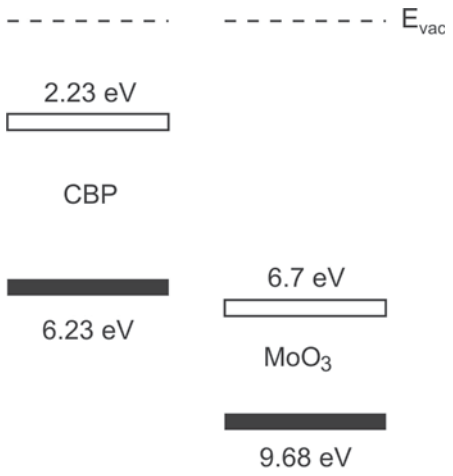

Figure 1.1: Energy levels of neat CBP and MoO_3 measured with UPS and IPES[36].

Probe analysis, turned out to be surprisingly low ($\approx 1-2\ \%$[37]). Similar results were for found for spiro-CBP doped with MoO_3 using capacitance-voltage analysis and polaron induced optical absorption[38] which revealed doping efficiencies of $2\ \%$ - $4.5\ \%$.
The commonly used assumption, that it is sufficient for effective p-type doping that the HOMO level of the dopant is higher than the LUMO of the matrix of course neglects various effects and can also not explain why doping efficiencies for doped organic semiconductors are often found to be unexpectedly low. Factors influencing the doping process which are normally not taken into account might be of structural or electronic origin.
From an energetic point of view the above mentioned picture is very simplified, since the knowledge of the energy levels of the single materials does not provide sufficient information about the electronic structure at the interface, for instance about the formation of interface dipoles. To gain information about the energetics at contacts between two materials, UPS and IPES measurements can be applied (see section 4.2.1). As will be explained in more detail in section 2.3.2 and 4.2.2.1 intermolecular hybridization, which leads to the formation of charge transfer complexes, might also change the energetic conditions at the interface in such a way that charge transfer is not as likely to occur as it would be expected on first sight and might also cause bound charge carriers at the interfaces which cannot contribute to the current flow.
It is well known that also morphological issues play a role when discussing electronic and electrical properties of organic semiconductors. For example, for crystalline and

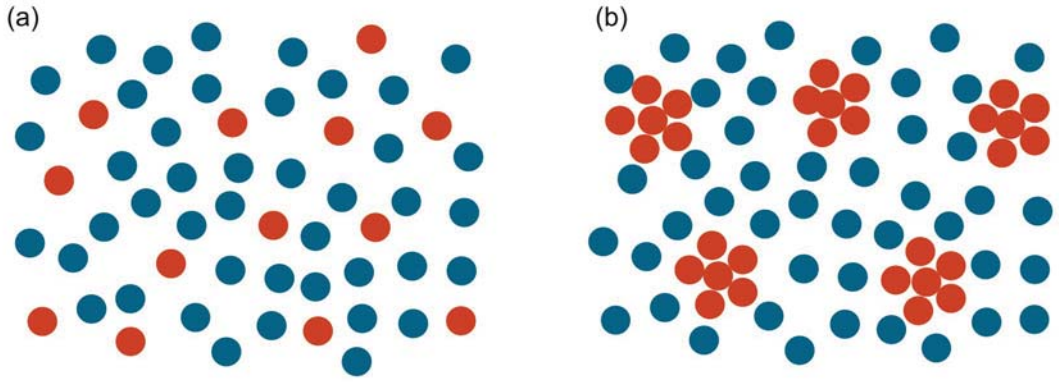

Figure 1.2: (a) Homogeneously dispersed molecules of two co-evaporated materials. (b) Agglomeration of dopants (red) could explain the low doping efficiency found for various material systems.

amorphous materials entirely different models have to be applied to describe the charge transport[39]. However, what is normally not taken into account is the potential influence of the topology. Instead it is commonly thought that by co-evaporation of two materials, for electrochemical doping or incorporation of dyes, the molecules of both components are dispersed homogenously, as schematically shown in Figure 1.2 (a). But it might also be that, depending on the material system, this assumption is wrong and agglomeration of the dopants occurs. As schematically depicted in Figure 1.2 (b) only a fraction of the dopants would then be in contact with the matrix molecules and only for these a charge transfer would be expected. Further analysis of the doping mechanisms and the correlation of morphology and electronic properties is crucial to improve device performance. Therefore, the present thesis tries to shine some light on the issue of low doping efficiencies with the intention to correlate structural with electronic and electrical properties.

1.2 Outline

The present work is organized as follows. In section 2 the theoretical background necessary to understand this thesis is presented. Chapter 3 describes the integrated UHV system where devices and thin films were prepared and where most of the measurements

presented in this thesis were conducted. Following, a brief introduction to all measurement methods used throughout this work is given and the sample preparation is depicted. Chapter 4 shows experimental results of MoO_3-doped CBP thin films. In section 4.1 the topology of the doped films is investigated using different measurement techniques of transmission electron microscopy (TEM), i.e. bright-field TEM, TEM spectroscopy and electron tomography to gain information about the distribution of the MoO_3 dopants within the CBP matrix. Furthermore, it is investigated to what extent the topology can be controlled by changing the substrate temperature during the evaporation process. The section ends with a description of the growth process of the observed MoO_3 agglomerations. Next, the results obtained from FTIR and XPS measurements acquired by Maybritt Kühn and Tobias Glaser within the scope of their respective diploma and PhD theses are summarized to gain insight into the electronic properties of CBP-films doped with MoO_3 (section 4.2). In section 4.3, the influence of the topology on the electrical properties is studied by measuring the IV characteristics of hole-only devices. To probe a possible electrical anisotropy, measurements perpendicular and parallel to the growth direction of the thin films are conducted for different doping concentrations. Furthermore, activation energies of doped films are determined from cryo-IV measurements and the influence of the substrate temperature onto the electrical properties is examined. By correlating the structural, electronic and electrical measurements, a model to describe the charge transport of MoO_3-doped CBP films is presented in section 4.4. In chapter 5, the influence of the deposition angle on the performance of OLEDs is investigated and in particular the organic/LiF interface is analyzed. The thesis is concluded with a short summary and an outlook on possible future work in chapter 6.

2 Theoretical Background

In the following chapter, the theoretical background, needed to understand the present thesis, will be presented. The chapter starts with an introduction to organic semiconductors, followed by the basic theory of charge transport in disordered organic semiconductors and models used to describe the doping process. Next, expressions to describe the IV characteristics of unipolar devices are presented and charge injection for different kinds of interlayers is elaborated. Finally, basic theory about OLEDs is depicted.

2.1 Organic Semiconductors

Organic semiconductors are based on carbon compounds with conjugated double bonds. In such systems, usually sp^2-hybridization occurs to minimize bond energies. One s-orbital, as well as two p-orbitals (p_x and p_y), form three mixed orbitals, which arrange in one plane with an angle of $120°$ to each other, while the fourth valence electron of the carbon atom occupies the p_z-orbital, which is oriented perpendicular to that plane. In a molecule, the sp^2-orbitals of neighboring molecules form so-called σ-bonds. Due to the strong orbital overlap, large splitting into binding σ- and antibinding σ^*-orbitals occurs, where electrons are highly localized. Figure 2.1 (a) depicts the energy levels in the case of sp^2-hybridization. As an example for an organic molecule, a schematic drawing of the hybrid orbitals of benzene is shown in Figure 2.1 (b). No interaction with radiation in the visible spectral range can take place, since the energy difference of occupied σ- and unoccupied σ^*-orbitals is too high. By contrast, superposition of the p_z-orbitals leads to weak, conjugated π-bonds. Because of the low binding energy of these bonds, electrons are delocalized along the whole conjugation length. Due to the weak overlap of the p_z-orbitals, only minor splitting of the p_z-states occurs and binding π- and antibinding π^*-orbitals are formed. The highest occupied π-state of a molecule is commonly denoted as HOMO (highest occupied molecular orbital), whereas the lowest unoccupied π^*-orbital is called LUMO (lowest unoccupied molecular orbital). Since the energy gap between

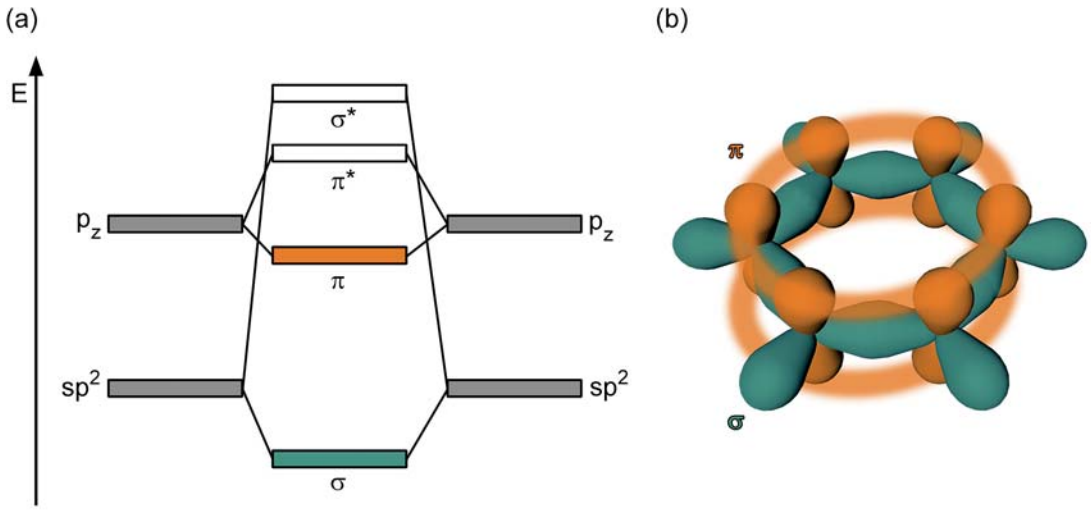

Figure 2.1: (a) Schematic illustration of the binding- and antibinding states in an organic molecule.
(b) Schematic drawing of the hybrid orbitals of benzene with σ- and π-bonds. The sp^2-hybridized orbitals form so-called σ-bonds, while the p_z-orbitals are only weakly bound via π-bonds.

HOMO and LUMO lies in the range of several eV, it covers the visible part of the optical spectrum and makes organic semiconductors suitable for optical applications like OLEDs or organic solar cells.

2.2 Theory of Charge Transport in Disordered Organic Semiconductors

The present section will give an overview of different models, which were developed to describe charge transport in amorphous organic semiconductors. To a great extent it follows the outline taken in Ref. [40].
In well ordered systems, like inorganic semiconductors or to a certain extent also organic crystals, band transport takes place. In contrast, only weak intermolecular coupling between the molecules exists in disordered amorphous semiconductors. Therefore, no band formation occurs, but instead charge transport proceeds via so called hopping transport between adjacent molecules. This process requires thermal activation to overcome energy

differences between different sites[40]. The mobility μ is related to the activation energy E_a, the temperature T and the Boltzmann constant k via[41]

$$\mu \propto \exp(-E_a/kT). \tag{2.2.1}$$

A basic model to describe hopping transport is the so-called Gaussian disorder model (GDM) introduced by Bässler[42]. An array of uncorrelated hopping sites with a cubic symmetry is considered. The energy ϵ of each site is given by a Gaussian density of states (DOS) with variance σ[42]:

$$D(\epsilon) = \frac{1}{\sqrt{2\pi\sigma^2}} \exp\left(-\frac{\epsilon^2}{2\sigma^2}\right). \tag{2.2.2}$$

σ is a measure for the amount of disorder and is mainly due to fluctuations of the lattice polarization energies in the case of small molecule systems[42].
The hopping rate ν_{ij} between the sites i and j can be described in different ways, with the most simple one being the so-called Miller-Abrahams form[40,42,43]

$$\nu_{ij} = \nu_0 \exp\left(-2\gamma a \frac{\Delta R_{ij}}{a}\right) \begin{cases} \exp\left(-\frac{\epsilon_j - \epsilon_i}{kT}\right) & \text{if } \epsilon_j > \epsilon_i, \\ 1 & \text{if } \epsilon_j \leq \epsilon_i. \end{cases} \tag{2.2.3}$$

with a pre-factor ν_0, the average lattice distance a, the inverse localization radius between adjacent sites γ, the distance between the sites i and j denoted as ΔR_{ij} and the temperature T.
Additionally, the so called positional disorder, described by the parameter Σ, must be considered. Σ is due to variation of intersite distances and variation in coupling of adjacent molecules due to different mutual molecule orientations[42]. The charge carrier mobility μ can be expressed in dependence of the temperature T, the electric field E and the two disorder parameters σ and Σ by[42]:

$$\mu(\sigma, \Sigma, E, T) = \mu_0 \exp\left(-\frac{4\widehat{\sigma}^2}{9}\right) \begin{cases} \exp\left(C(\widehat{\sigma}^2 - \Sigma^2)\sqrt{E}\right) & \text{if } \Sigma \geq 1.5, \\ \exp\left(C(\widehat{\sigma}^2 - 2.25)\sqrt{E}\right) & \text{if } \Sigma \leq 1.5. \end{cases} \tag{2.2.4}$$

with $\widehat{\sigma} = \sigma/kT$ and the constant C, which depends on the site separation[40].
According to equation (2.2.4), charge carriers might also move against the field direction, since for $\widehat{\sigma} < \Sigma$ respectively $\Sigma > 1.5$ the mobility becomes negative. This effect, which can only occur at low electric fields, is due to an interplay between positional disorder Σ and energetic disorder σ, leading to situations where this behavior is energetically favorable[40,44].
The electrical field dependence can be described by a Poole-Frenkel like behavior of the form $\mu \propto \exp\sqrt{E}$. Experimentally, this Poole-Frenkel like dependence was found to be valid for a wider range of electrical fields than predicted by equation (2.2.4). To account for this deviation, Gartstein and Conwell introduced the so called correlated Gaussian disorder model (CGDM), where additionally spatial correlation of the energetic disorder is assumed which is due to dipole interactions of charged species with adjacent sites[45].
Charge carriers relax towards the tail states of the DOS and tend to occupy a so-called occupational-DOS (ODOS) in quasi-equilibrium. The center of this ODOS is displaced by $\varepsilon_0 = \sigma/kT$ from the maximum of the DOS[46,47] (see Figure 2.2 (a)). For small carrier densities, the Fermi energy E_F is located deep in the band gap, well below σ/kT, and does therefore not play a role for charge transport. Since the transport energy E_t is located close to the maximum of the DOS, the activation energy equals approximately σ/kT and is independent of the charge carrier density (see Figure 2.2 (a)). In conjunction with equation (2.2.1) this results in a non-Arrhenius-like dependence of the mobility with respect to the temperature, namely $\log\mu \propto 1/T^2$ [40,42].

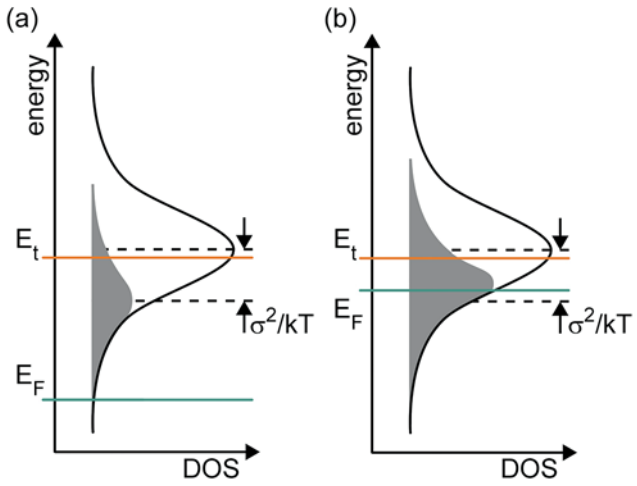

Figure 2.2: (a) In the case of a low charge carrier density the activation energy E_a equals approximately σ/kT, since the transport energy E_t is roughly the maximum of the DOS. This results in a $\log\mu \propto 1/T^2$ dependence of the mobility.
(b) For high charge carrier densities, the activation energy is determined by difference between the transport energy and the Fermi level E_F, which leads to a $\log\mu \propto 1/T$ dependence of the mobility.

2.3 Doping of Organic Semiconductors

In this section models, developed to describe doping of organic semiconductors will be presented. The first part covers the commonly used integer charge transfer doping model. This simple model is then extended by the idea of hybridization and the internal interface charge transfer doping model. Finally, the influence of doping on the mobility is explained.

2.3.1 Integer Charge Transfer Model

Doping is defined as incorporation of impurities into a semiconductor to enhance the number of free charge carriers. This leads to an enhancement of the conductivity σ, which is related to the charge carrier density n and the mobility μ, according to:

$$\sigma = en\mu. \tag{2.3.1}$$

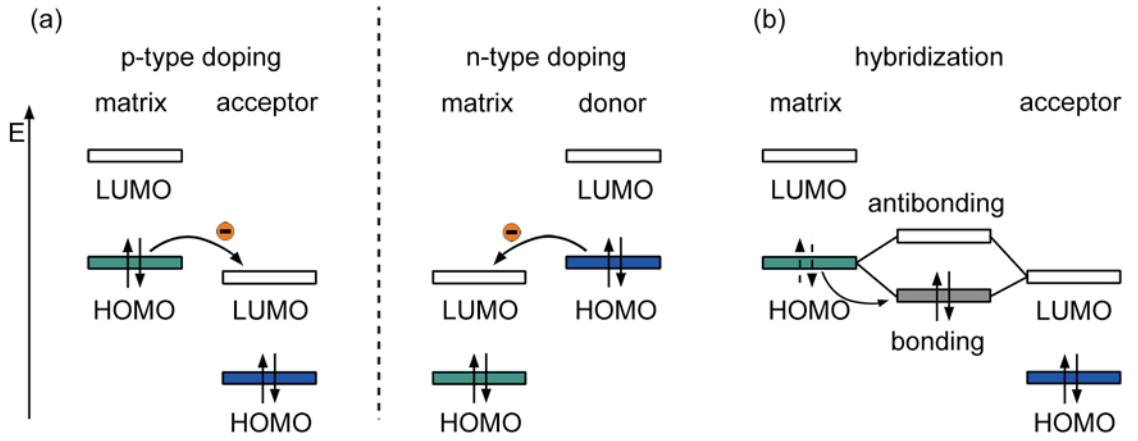

Figure 2.3: (a) Schematic drawing of the integer charge transfer doping model. In the case of p-type doping, an electron is transferred from the HOMO of the matrix molecule to the LUMO of the dopant, while for n-type doping an electron jumps from the dopant LUMO to the matrix HOMO.
(b) In the case of p-type doping, hybridization of the matrix HOMO with the dopant LUMO leads to the formation of a bonding and an antibonding hybrid orbital, which are the HOMO respectively LUMO of the charge transfer complex. The HOMO of the charge transfer complex is doubly occupied with the electrons of the former matrix HOMO, while the antibonding molecule orbital is empty[50].

For doping of inorganic semiconductors single atoms are incorporated into the crystal structure of the host material were they replace host material atoms. In the case of p-type doping, the dopants posses one valence electron less than the host material. Because of the low dielectric constant of inorganic semiconductors the coulomb interaction between valence electrons and the atomic nucleus is low and allows ionization already at room temperature where electrons of the host materials are gathered by the dopant atoms, which leads to free holes. However, this concept does not work for organic materials. For example, if one of the carbon atoms of benzene is replaced by a nitrogen atom, no enhancement of charge carriers occurs, but a new molecule, pyrilene, is formed[48,49]. Therefore, instead of substituting single atoms, normally complete molecules are incorporated for doping organic semiconductors.
In the simplest doping model, which is commonly considered for an organic semiconductor, a mutual ionization process is assumed. An electron is transferred from the HOMO

of the matrix molecule to the LUMO of the dopant in the case of p-type doping, while for n-type doping an electron moves from the dopant LUMO to the matrix HOMO, as depicted in Figure 2.3 (a)[51,52]. In the following, only p-type doping will be considered. In this case it is commonly thought, that this process results in an electron localized at the dopant and a mobile hole in the organic matrix, leading to an increased charge carrier density and hence to a higher conductivity. Furthermore, it is commonly expected that for efficient doping it is sufficient to have matrix-dopant couples with the ionization energy (IE) of the host molecules being larger than the electron affinity (EA) of the dopants in the case of p-type doping and that a higher work function difference leads to a more effective doping process due to the higher driving force for the charge transfer. This was, for example, shown by Lee et al.[53] who investigated CuI, MoO_3, and ReO_3 doped into 2-TNATA. This assumption might be successfully applied to many situations but cannot be assumed generally. As already mentioned in section 1.1, another aspect which is often not taken into account when discussing energetic issues for doping, is the fact that interface dipoles can be present which lower the work function difference at the interface. The formation of the interface dipole might be influenced by several factors like chemical interactions, the presence of interface states, orientation of organic molecules or charge transfer across the interface[54]. To study the band alignment of a material interface an interface experiment can be conducted were one material is deposited onto another one in a stepwise fashion and after each deposition step the sample is characterized using XPS and UPS to gain information about the interface energetics[54,55].

2.3.2 Intermolecular Orbital Hybridization

In various organic material systems broad excitations were observed upon doping using optical spectroscopy[32,35,56–59]. The appearance of these excitations are explained by the formation of charge transfer complexes between host and dopant, which can be excited optically. Charges are transferred between the two species (as described in the previous section) which are first bound in the charge transfer complex as electron-hole pair. Depending on the energy landscape in the vicinity of the charge transfer complex, the bound charges can dissociate with a certain probability, creating free charge carriers[60]. Since organic materials have a lower dielectric constant than inorganic semiconductors[1]

screening through neighboring molecules is lower. This causes a lower dissociation probability for organic systems compared to inorganics. One speaks about a partial charge transfer if the transferred electron also has a certain probability of presence at the matrix molecule[62].

To explain the underlying physical process in more detail, a doping model based on intermolecular orbital hybridization was suggested[50,63], as depicted in Figure 2.3(b). The formation of charge transfer complexes is explained by hybridization of the matrix HOMO with the dopant LUMO which leads to the formation of a bonding and an antibonding supramolecular hybrid orbital, which are the HOMO respectively LUMO of the charge transfer complex. The HOMO of the charge transfer complex is doubly occupied with the electrons of the former matrix HOMO, while the antibonding molecule orbital is empty (see Figure 2.3 (b)). The proposed model could also be confirmed by correlation of experimental findings with density functional theory (DFT) calculations[50]. In the DFT calculations orbital overlap was found to cause substantial splitting of bonding and antibonding hybrid orbitals. Furthermore, it was shown that the orientation of the two species relative to each other influences the amount of splitting[50]. The calculations revealed a higher ionization energy compared to the undoped material and a reduced energy-gap because of the hybridization process[50]. The latter could also be confirmed by Salzmann et al. for pentacene doped with F_4-TCNQ using UV-VIS[2] spectroscopy[50]. Evidence for such splitting has also been found for other material systems[63–66].

This model also provides an additional possible explanation for low doping efficiencies often found in doped organic semiconductors (see section 1.1). Since the empty bonding hybrid state is still several ten meV above the HOMO of the host material, and the occupancy takes place according to Fermi-Dirac statistics, only a fraction of the charge transfer complexes are ionized at room temperature[50]. This gives an explanation why such high doping concentrations have to be applied for organic materials to give a reasonable rise in conductivity. For inorganic semiconductors, acceptor states are typically only a few meV above the valence band edge, so that almost all dopants are already ionized at room temperature.

[1] $\varepsilon_{\text{silicon}}$=11.7 eV $\varepsilon_{\text{germanium}}$=15.8 eV[61] $\varepsilon_{\text{organic}}$=$3-4$ eV[40,60]

[2] Optical spectroscopy in the ultraviolet (UV) and visible (VIS) range.

2.3.3 Internal Interface Charge Transfer Doping Model

Mayer et al.[67] suggested the so-called internal interface charge transfer doping model, which is based on the assumption that the dopants form agglomerations within the organic matrix. As it will be shown in section 4.1, this is the case for CBP doped with MoO_3. The model assumes that charge transfer occurs by thermodynamic alignment of the Fermi levels of matrix and dopant at the internal interfaces. The work function difference $\Delta\Phi = \Phi_{\text{matrix}} - \Phi_{\text{dopant}}$ of the single materials is then compensated by two contributions. The first contribution is an interface dipole δ, which lowers the work function difference of matrix and dopant and therefore reduces the driving force for the charge transfer. The remaining contribution of the work function difference is then compensated by a long-range charge transfer. This causes the formation of space charge regions which lead to bend bending at the interface. The maximum band bending for matrix respectively dopant is depicted as eV_{bb}^{M} and eV_{bb}^{D}, so that the following relation holds:

$$\Delta\Phi = eV_{\text{bb}}^{\text{M}} + eV_{\text{bb}}^{\text{D}} + \delta. \tag{2.3.2}$$

The assumption that for a particular material combination only a single value for the interface dipole δ exists, is of course an oversimplification. Since different crystallographic or morphological interfaces lead to different interface dipole magnitudes, the value for δ in equation (2.3.2) must be seen as a mean value[67].
The internal interface charge transfer doping assumes that the value of the dipole is the same at the measured bilayer and at the internal interfaces in a composite. Then, the maximum Fermi level variation $\Delta E_{\text{F}}^{\text{matrix}}$ respectively $\Delta E_{\text{F}}^{\text{dopant}}$ in a composite is equal to the maximum band bending of each phase of the bilayer, following:

$$\Delta E_{\text{F}}^{\text{matrix}} = eV_{\text{BB}}^{\text{M}}, \tag{2.3.3a}$$

$$\Delta E_{\text{F}}^{\text{dopant}} = eV_{\text{BB}}^{\text{D}}. \tag{2.3.3b}$$

Mayer et al. could show with PES, that for interfaces of WO_3 and CuPc, as well as F_4-TCNQ and CuPc, different deposition sequences lead to different values for the interface dipole. This might, for example, be due to different source temperatures which affect the

temperature of the substrate during deposition or different amounts of diffusivity. They could also show that the internal interface charge transfer doping model can be correlated with these PES interface experiments, because the maximum Fermi level change of composites lies in between those obtained by interface experiments of the bilayer measurements with different deposition orders.

2.3.4 Influence of Doping on Mobility

The models presented in section 2.2 can be applied under the assumption of a negligible interaction between the charge carriers[40]. However, this is no longer valid when doped systems are examined, which exhibit high charge carrier densities. In this case, additional factors, influencing the charge transport, have to be taken into account.
With increasing charge carrier density, energetically deep lying trap states become filled[68]. Recently, this was demonstrated experimentally and it was shown that for C_{60} doped with the n-type dopant $[RuCp^*(mes)]_2$ filling of traps occurs up to about 10^{-2} mol% doping concentration[69].
For increasing charge carrier densities, the Fermi energy moves towards the transport energy and passes $\varepsilon_0 = \sigma/kT$ for high carrier concentrations[70] (see Figure 2.2 (b)). Then, E_F serves as new starting point for the hopping process[41] and the activation energy equals the difference between E_F and the transport energy E_t. Compared to the case of low charge carrier density (see section 2.2), E_a depends on the charge carrier density. Since the activation energy does not depend on the temperature anymore, this results in a weaker temperature dependence of the mobility than in the case of low charge carrier densities (see section 2.2). Using equation (2.2.1), a $1/T$ dependence of the mobility ($\mu \propto \exp(1/T)$) is found[40,71].
In section 4.3.2, activation energies of doped systems will be investigated by measuring temperature-dependent IV characteristics and the activation energy E_a will be calculated, under the assumption of a temperature-independent charge carrier density n, according to:

$$I = I_0 \exp\left(-\frac{E_\mathrm{a}}{kT}\right). \tag{2.3.4}$$

To describe the dependence of the charge carrier density on the mobility due to filling of tail states, Pasveer et al.[72] presented a unified theoretical description, which takes into account the influence of temperature T, electrical field E and charge carrier density p, the so called extended Gaussian disorder model (EGDM).
According to Arkipov et al.[73], the mobility in doped semiconductors is also affected by coulombically bound electron-hole pairs, which arise due to the charge transfer between host and dopant. The condition mentioned above, that in the case of p-type doping the HOMO of the dopant must be energetically higher than the LUMO of the matrix, must then not compulsory be fulfilled, as long as the energy difference can be compensated by the gain in Coulomb energy upon charge transfer. The Coulomb interaction creates additional energetic disorder due to the random distribution of the dopant ions. This causes a broadening of the DOS which increases the number of deep states. Therefore, two competitive effects occur upon doping: An increase of the charge carrier density shifts up the Fermi level and enhances the conductivity, while the creation of deep traps suppresses a conductivity enhancement. Mityashin et al.[60] pointed out, that a threshold for the dissociation probability of coulombically bound electron-hole pairs exists. Only for doping concentrations beyond this threshold the electron-hole pairs can be separated, because dissociation pathways are formed due to the energetic disorder which is introduced by adjacent dopants. For pentacene doped with F_4-TNCQ they calculated a threshold density of $1\ \%$ in the case of negligible positional disorder[60].

2.4 IV Characteristics

One possibility to gain insight into the charge transport properties experimentally is measuring the IV characteristics. The conductivity σ can then be determined from the current density j and the electrical field E according to:

$$j = \sigma E. \tag{2.4.1}$$

An exemplarily IV characteristic of a unipolar device is depicted in Figure 2.4. At low voltages U, the current is dominated by intrinsic, thermally activated charge carriers,

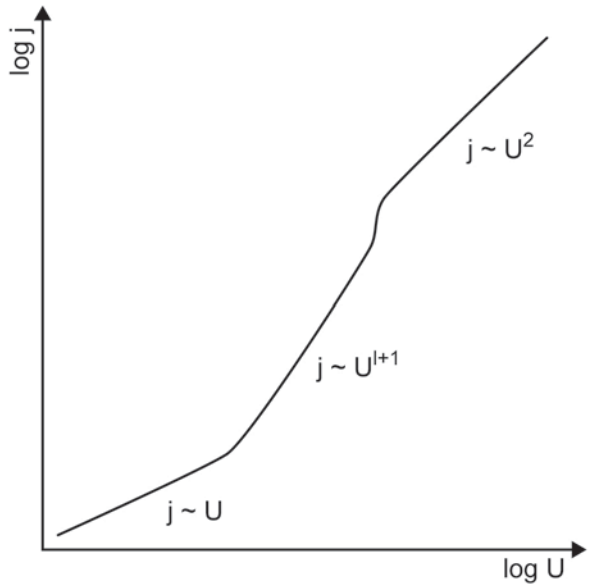

Figure 2.4: Current density j versus voltage U dependence of a unipolar device.

which are already present in the film. In this case of an Ohmic conduction, the current density j of a film with thickness d can be calculated according to the following relation:

$$j = en\mu\frac{U}{d}. \tag{2.4.2}$$

Applying higher voltages, the current is dominated by injected charge carriers. In the idealized case of a trap-free space charge limited current with a constant mobility, the Mott-Gurney relation holds, often also referred to as Child's law:

$$j = \frac{9}{8}\epsilon\epsilon_0\mu\frac{U^2}{d^3}. \tag{2.4.3}$$

Assuming a constant mobility with one discrete trapping level $G_\mathrm{t}(E) = N_\mathrm{t}\delta(E - E_\mathrm{t})$ with N_t being the density of the shallow traps and E_t being their depth, leads to the same relation as depicted in equation (2.4.3) for high current densities. However, for small current densities μ must be replaced by $\mu_\mathrm{eff} = \mu\Theta$ with $\Theta^{-1} = 1 + N_\mathrm{t}/N_\mathrm{e}\exp(E_\mathrm{t}/kT)$. N_t denotes the number of molecules per unit volume[74].

For intermediate voltages, filling of traps influences the IV characteristics. In the case of an exponential trapping distribution, the current density can be calculated using the following relation[74]:

$$j = e\mu N_{\mathrm{e}} \left(\frac{2l+1}{l+1}\right)^{l+1} \left(\frac{l}{l+1}\frac{\epsilon\epsilon_0}{eN_{\mathrm{t}}}\right)^{l} \frac{U^{l+1}}{d^{2l+1}} \tag{2.4.4}$$

with $l := E_{\mathrm{t}}/kT$. This equation is valid in the voltage range where no significant amount of the trapping states is filled and is often referred to as the trap charge limited current region. The case of a Gaussian trapping distribution can only be distinguished from the exponential case, if the temperature is varied over a wide range, since it is formally identical to equation (2.4.4)[74].

2.5 Charge Injection at Contacts

To obtain highly efficient devices with low operating voltages, the energetic barriers for charge carrier injection at the electrodes have to be reduced. A simple approach to enhance carrier injection is the introduction of injection layers between the electrode and the organic transport layers. In this section, contacts which are used throughout this work to enhance or investigate charge injection will be described. In section 2.5.1 aspects important for injection, using MoO_3 layers, are covered. Section 2.5.2 describes what is known about LiF injection layers.

2.5.1 MoO_3 Injection Layers

It was shown that MoO_3 can serve as a very efficient hole injection layer, e.g. for OLEDs[75–78] or OPV[79,80]. In the present work, MoO_3 is used as injection layer for hole only devices and OLEDs.

Because of the very high ionization energy of MoO_3 ($9.68\ \mathrm{eV}$[36]), hole injection and transport is very unlikely to occur via the valence band. Instead, as schematically depicted in Figure 2.5, a charge generation process takes place under positive bias, where hole injection proceeds via electron transfer from the HOMO level of the organic layer to the conduction band of the TMO, from where it is collected by the electrode[81–83]. The energy barrier which has to be overcome in this case is the difference of the HOMO of

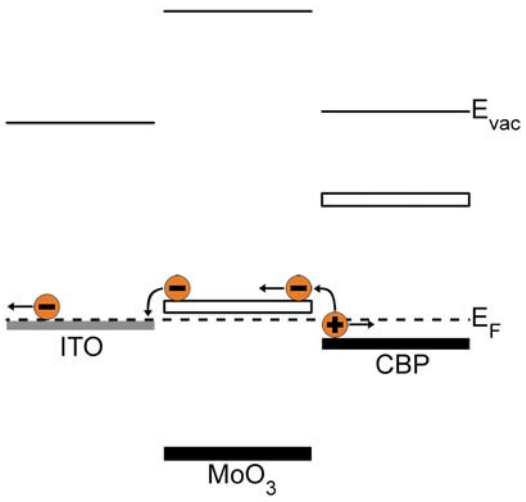

Figure 2.5: Mechanism of charge injection with MoO_3 interlayers. Hole injection proceeds via electron transfer from the HOMO level of the organic layer to the conduction band of the TMO, from where it is collected by the electrode[81].

the organic material and the conduction band minimum of the TMO.
The model described above was also used to explain the charge generation mechanism in so called charge generation layers (CGLs). These are often applied in stacked OLEDs[84,85].

2.5.2 LiF Injection Layers

Thin LiF injection layers in conjunction with an aluminum cathode are commonly used for OLEDs[15,86] and also OPV[87] to significantly enhance electron injection. Instead of LiF, also other materials, like CaF_2[88] or MgF_2[89] can be applied, which show a similar function. The first OLED with an LiF interlayer was presented by Hung et al.[15] in 1997. Since then, several studies have been presented to reveal the mechanisms which lead to the enhanced device performance. Nonetheless, a comprehensive picture, describing the process of contact formation for this material, is still missing.
One given explanation was that tunneling of electrons into the LUMO of the electron transporting organic material is possible, since a voltage drop across the insulating LiF layer leads to Fermi level alignment and thus decreases the injection barrier between the electron transporting organic semiconductor and the cathode[86]. Ihm et al.[90] investigated the Alq_3/LiF interface with PES and found that the Fermi level shifts towards the

LUMO for increasing LiF coverage. A saturation of the Fermi level shift was found to occur at about $2.6\ \mathrm{nm}$ LiF thickness. They deduced that the Fermi level shift is due to band bending caused by the work function difference of the two materials which leads to a charge redistribution, which lowers the injection barrier.
The influence of the deposition of aluminum onto LiF was studied in Ref. [91]. Secondary ion mass spectroscopy (SIMS) depth profiles were acquired and revealed that, upon aluminum deposition, a chemical reaction of aluminum and LiF takes place in the presence of water. This leads to single lithium atoms, which can diffuse into the organic Alq_3 layer and act as dopant. For a reversed deposition sequence (LiF on top of aluminum) less enhancement of the electron injection was observed, indicating that the kinetic energy of the aluminum atoms is crucial. That the chemical reaction depends on the deposition sequence was also confirmed by Xie et al.[92] using synchrotron radiation PES.

2.6 OLED Theory

In the following section the operating principle of OLEDs will be depicted. Furthermore, the OLED stack which is used as basis for the experiments in chapter 5 will be introduced.

2.6.1 Working Principle of OLEDs

State-of-the-art OLEDs normally consist of a multitude of different layers. Figure 2.6 shows the schematic structure of a working OLED device with a sequence of functional organic layers sandwiched between two electrodes. Under positive bias, holes are injected from the anode into the hole transport layer (HTL) and electrons are injected from the cathode into the electron transport layer (ETL). The injected charge carriers drift through the transport layers, recombine to form excitons and finally decay radiatively with a certain probability in the so called emission layer (EML). Since the light has to be outcoupled through at least one of the electrodes, normally indium tin oxide (ITO) is used as transparent anode for bottom-emitting OLEDs.
For high efficiencies low potential barriers between the contacts and the transport layers are required. Therefore, often hole injection layers (HIL) and electron injection layers (EIL) are inserted between the contacts and HTL as well as ETL. These can consist of very thin layers, like MoO_3 or LiF, as was elaborated in more detail in section 2.5.1 and 2.5.2.

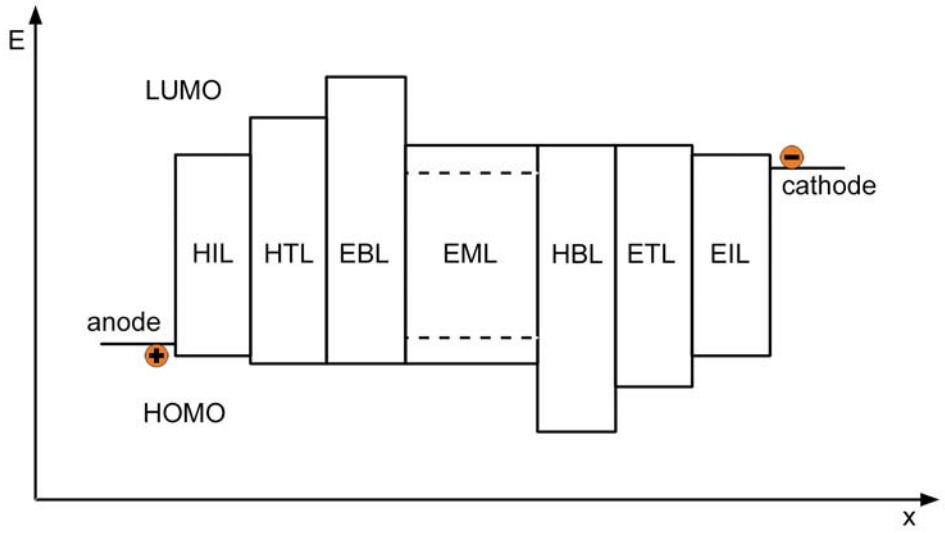

Figure 2.6: Schematic structure of an OLED layer stack.

Another common approach is the insertion of electrochemically doped layers which lead to thin depletion regions where charge carriers can easily tunnel through[93]. To localize the emission zone, ensure an optimal electron-hole balance and prevent exciton quenching, often electron blocking (EBL) and hole blocking (HBL) layers are introduced, which can also serve as exciton blocker. The desired properties of EBL and ETL respectively HBL and HTL can often be fulfilled by the same materials.

The major issue nowadays, which determines the overall performance of OLEDs, is the outcoupling efficiency of the light which is produced inside the device. To address this topic, various concepts such as micro-lens arrays[94] or scattering films[95] have been developed.

The light outcoupling of an OLED is determined by measuring the radiative flux ϕ_r. The corresponding photometric quantity is the so called luminous flux ϕ_p, which is defined as follows:

$$\phi_\mathrm{p} = K_\mathrm{m} \int_{380\ \mathrm{nm}}^{780\ \mathrm{nm}} \phi_\mathrm{r} V(\lambda) d\lambda \tag{2.6.1}$$

with $K_\mathrm{m} = 683\,\mathrm{lm/W}$. ϕ_p takes the wavelength λ-dependent sensitivity of the human eye, described by the eye sensitivity curve $V(\lambda)$, into account. The luminous flux per

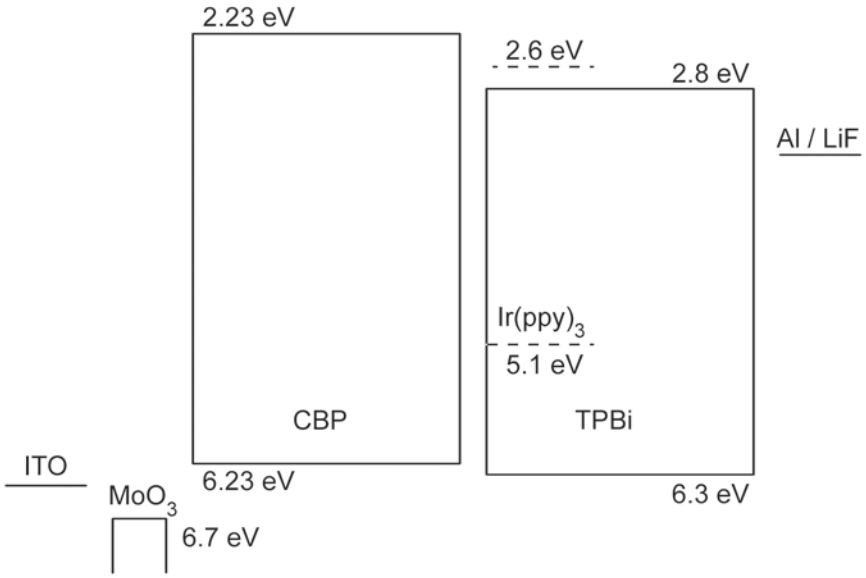

Figure 2.7: Structure of the OLED stack used in this work based with energy values of the single materials. The energy values were taken from Refs. [36] and [96].

solid angle element $\Delta\Omega$ of an emitter, referred to its emitter area A, is called luminance L. To convert photometric and radiometric quantities the conversion factor K, called luminous efficacy of radiation

$$K = \frac{K_\mathrm{m} \int_{380\,\mathrm{nm}}^{780\,\mathrm{nm}} \phi_\mathrm{r} V(\lambda) d\lambda}{\int_{380\,\mathrm{nm}}^{780\,\mathrm{nm}} \phi_\mathrm{r} d\lambda} \tag{2.6.2}$$

is used, which is unique for each emitter spectrum.

2.6.2 OLED Stack Employed in this Work

The OLEDs presented in chapter 5 are based on the stack proposed by Meyer et al.[96]. The layer sequence and the HOMO and LUMO levels of the single materials are sketched in Figure 2.7. As anode transparent ITO is used. As described in section 2.5.1, a thin TMO interlayer between aluminum and the hole transport layer can be used to enhance charge injection. Since the present work deals with MoO_3, tungsten oxide (WO_3), which was used in Ref. [96], was replaced by MoO_3 ($10\,\mathrm{nm}$). To also enhance electron injection, a LiF/aluminum contact is applied as cathode, with a LiF-thickness of $2\,\mathrm{nm}$ and

the aluminum contact being $100\ \mathrm{nm}$ in thickness. In section 5 this contact is investigated more closely. TCTA ($50\ \mathrm{nm}$) serves as hole transport layer at the anode side, whereas a $30\ \mathrm{nm}$ thick TPBi layer is applied as electron transport and exciton blocking layer at the cathode side. The green phosphorescent emitter $Ir(ppy)_3$ is doped with a concentration of $7\ \mathrm{vol}\%$ into a $20\ \mathrm{nm}$ thick TPBi layer between the ETL and HTL to define the emission zone.

3 Experimental Details

In the first part of this chapter the integrated UHV systems is introduced where all samples for this thesis were fabricated and many of the presented measurements were acquired. The second part gives a short overview on all analytical methods applied in this work. Finally, sample preparation is described in the last part.

3.1 The Clustertool: An Integrated UHV System

All samples were prepared in an integrated ultra-high vacuum (UHV) system, called clustertool, which is sketched in Figure 3.1. It allows sample preparation as well as the application of several complementary analytical methods, to address different issues in the field of organic electronics.
A glovebox with nitrogen atmosphere can be used for changing shadow masks for devices as well as for wet processing of films via spincoating. From there the sample holders can be introduced into the UHV system via a load lock. Three distributor chambers allow to move samples into each part of the system without breaking the vacuum.
For thin film growth, three evaporation chambers are available, which were setup within the scope of the presented work, one for metals (metal chamber) and two for organics and metal oxides (organic chamber 1 and 2). Each of the two organic chambers can be equipped with up to eight evaporation cells. Films are grown by thermal evaporation of powders from Knudsen cells, consisting of quartz crucibles indirectly heated via tantalum wires. The effusion cells are controlled by adjusting the applied electrical power. Aside, it is also possible to measure the temperature with a thermocouple (type K), which is attached to a small pit at the bottom of the quartz crucible. The metal chamber allows to evaporate four different metals from evaporation boats which are directly resistively heated. To ensure uniform film coverage, the sample holders are rotated during depo-

sition in all deposition chambers with a frequency of about $1\ \mathrm{Hz}$[1]. In all chambers the thickness of the evaporated layers can be monitored using calibrated oscillating quartz crystals which are water-cooled to ensure better stability. To allow for co-evapoaration in the organic chambers, oscillating crystals are positioned in such a way that opposite evaporation cells do only deposit onto one of the oscillating crystals, allowing for independent control of the two material rates.

Several analysis chambers exist, which are operated by three different research groups from the universities of Heidelberg, Darmstadt and Braunschweig within the scope of the BMBF project MESOMERIE [2] at InnovationLab in Heidelberg. The group of Prof. Pucci from the University of Heidelberg operates a Fourier transform infrared (FTIR) spectrometer, where IR spectra can be acquired in absorption and reflection mode. The setup allows to measure FTIR spectra during thin film growth, since the chamber is also equipped with two evaporators. An oscillating crystal is used prior to film deposition to adjust the evaporation rates and replaced by the sample holder during the deposition process. Furthermore, it is possible to cool the substrate during film deposition down to about $120\ \mathrm{K}$. The group of Prof. Jägermann from the TU Darmstadt is responsible for the photoelectron spectroscopy (PES) setup, which allows to measure x-ray (XPS) and ultraviolet photoelectron spectroscopy (UPS) spectra and also offers the possibility to perform IPES experiments. Beside, an UHV atomic force microscope (AFM), the TU Braunschweig operates a crossbeam-system, consisting of a scanning electron microscope (SEM) combined with a focused ion beam (FIB) and a gas injection system (GIS) to mill cross sections and prepare TEM lamellae. Additionally, it is possible to exchange the 6-axis table of the SEM by an AFM, so that AFM measurements can be performed on FIB-milled cross sections and the scanning process can be monitored during the measurements. Both AFMs are also capable of performing scanning Kelvin probe microscopy (SKPM) and scanning tunneling microscopy (STM) measurements.

[1] The film thickness in organic chamber 1 was measured to vary by less than $3\ \%$ at the areas relevant for sample preparation [97].

[2] Morphologie und elektronische Struktur von Organik/Organik und Organik/Metalloxid Hybridsystemen.

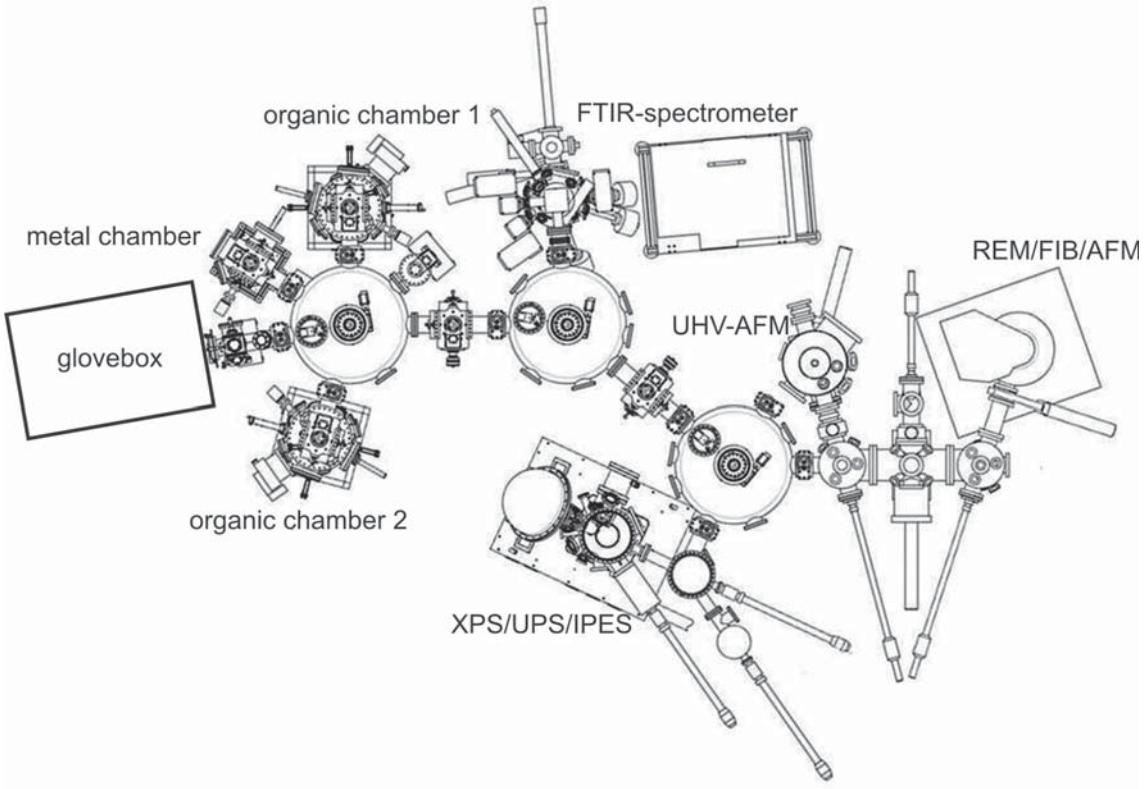

Figure 3.1: Schematic drawing of the clustertool at Innovationlab in Heidelberg. For sample preparation a glovebox and three evaporation chambers are available. Additionally, various analytical methods can be applied, namely FTIR spectroscopy, photoelectron spectroscopy and scanning probe methods.

3.2 Analytical Methods

In the following section the measurement principles of all analytical methods applied throughout this work are explained. The first part covers the basic principles of different TEM measurement techniques. This includes bright-field TEM, TEM spectroscopy and electron tomography. Also a short overview of the technical parameters of the microscopes, which were used for data acquisition, are given. The second part deals with measurement techniques from which information about the electronic properties can be inferred, namely FTIR and PES. Details of the electrical measurements are described in the last part.

3.2.1 Transmission Electron Microscopy

In a TEM a quasimonochromatic electron beam is transmitted through a very thin specimen. For imaging with electrons, a very high resolution can be achieved, which lies within the range of atomic distances, due to the small de Broglie wavelengths of the electrons.

Electrons can interact with the sample in two ways: elastic and inelastic scattering. In the case of elastic scattering, the electrons do not lose energy. Usually, elastically scattered electrons are coherent and scattered into low angles (about $1°$-$10°$ [98]). However, they can also be scattered into larger angles and become incoherent. Inelastic scattering processes can also take place, where electrons lose energy after having caused, for instance, electronic or plasmonic excitations. In this case, electrons are scattered under an angle of less than $1°$ and are coherent [98].

Bright-field TEM is the most common imaging mode, where either all electrons are detected or electrons scattered under high angles do not contribute to the image because they are filtered out by an objective aperture. The latter improves the contrast since the effect of the spherical aberration is reduced. Additionally, zero-loss filtering is often applied, where only electrons which have suffered no or only minor energy loss, i.e. elastically scattered electrons or electrons which have not interacted with the sample at all, are detected. Zero-loss filtering also enhances the contrast.

To determine the layer thickness of the investigated films, so-called thickness maps can be acquired, where a bright-field image as well as a zero-loss filtered bright-field image

are recorded. The thickness d of the specimen is related to the intensity of a pixel in the bright-field image I and the intensity of the corresponding pixel in the zero-loss filtered image I_0 via:

$$I = I_0 e^{-d/\lambda}. \tag{3.2.1}$$

From this relation, the thickness d can be determined, if the mean free electron path λ is known. If λ is unknown, only the relative thickness I/I_0 can be derived.
Beside bright-field imaging, various other TEM imaging methods can be applied. Their basic principles will be explained in the following sections.

3.2.1.1 TEM Spectroscopy

The contrast in bright-field TEM can be a material contrast, but can also originate from other effects like thickness variations or the existence of crystalline and amorphous domains. To identify different materials, analytical electron microscopy can be applied. A schematic drawing of this method is depicted in Figure 3.2. Electrons of the incident electron beam interact with the molecules of the sample via inelastic scattering processes, which cause the electrons to lose energy. This results in a polychromatic beam with electrons exhibiting specific loss energies according to the respective processes.
To collect spectral information of the whole illuminated sample area, electron energy loss spectroscopy (EELS) can be applied, where the intensity of the electron beam is measured as a function of the loss energy. With EELS, very high energetic resolution can be achieved. For example, an incident electron energy of $60\ \mathrm{kV}$ leads to an energy resolution of about $80\ \mathrm{meV}$, depending on the sample.
To spatially discriminate local chemical distributions, electron spectroscopic imaging (ESI) can be performed, where only electrons at a certain loss energy are detected, resulting in monochromatic images. Adequate image analysis can then be used to obtain chemical contrast[99,100]. ESI can be applied in two energy regimes, which will be described in the following sections.

Core Loss ESI
Chemical contrast can be obtained by applying ESI in the core loss regime. Incident electrons can ionize tightly bound core electrons. With this process, the incident electrons

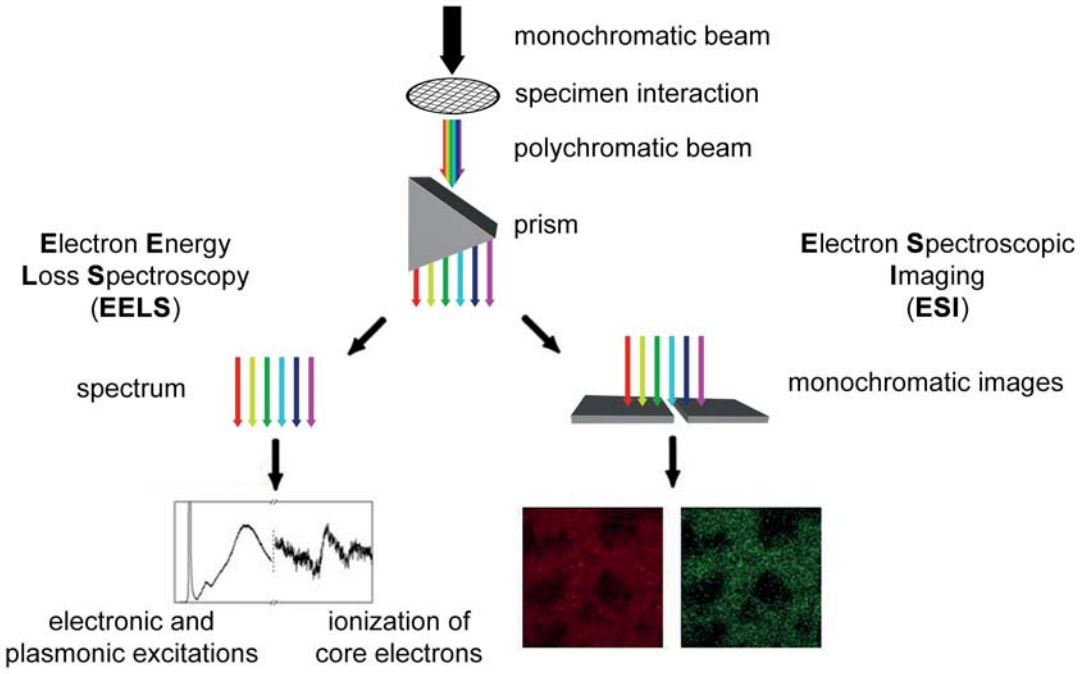

Figure 3.2: Measurement principle of TEM spectroscopy. Since electrons of the incident beam interact with the molecules of the sample, they lose energy according to the respective interaction processes. The emerging polychromatic beam can then be measured as a function of the loss energy (EELS) or an image can be acquired where only electrons at a certain loss energy are detected (ESI).

lose energy and an ionization edge, located at the binding energy of the ionized core electron, appears in the loss spectrum. Core loss ESI can be used to differentiate between different elements and is often applied for elemental mapping of inorganic samples. Although interpretation of the measurement results is quite simple, there are still various disadvantages of imaging in this energy regime. The low ionization cross section causes poor signal-to-noise ratio. Therefore, long data collection times are required which lead to high beam doses. This can damage sensitive organic thin films and also induce distortions in the sample. Furthermore, it is quite difficult to achieve nanometer resolution since the influence of spatial sample drift increases when long data collection times are applied.

As can be seen in Figure 3.3 (a), the ionization edges, which appear in the EEL spectra, are superimposed on a background, mainly originating from multiple inelastic electron scat-

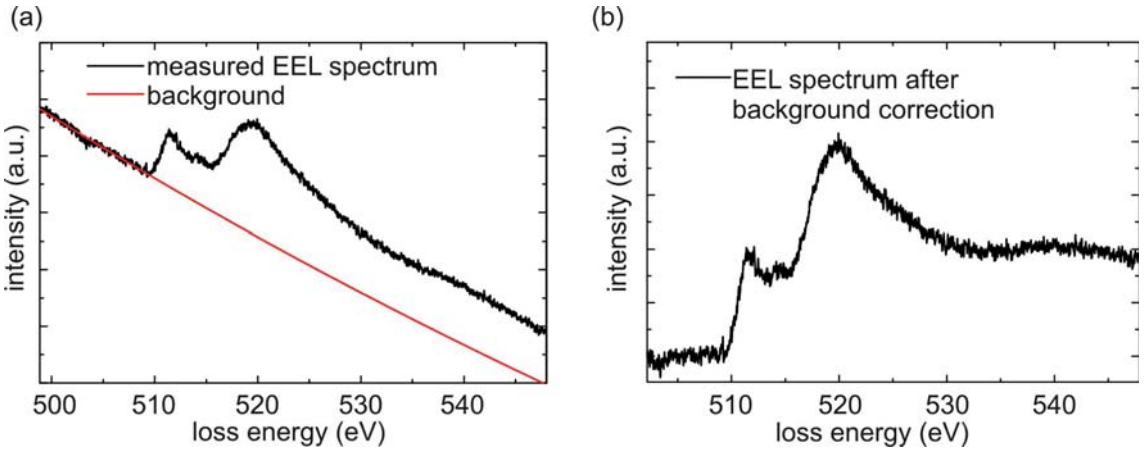

Figure 3.3: (a) Example of a core loss EEL spectrum with an ionization edge as well as a background which is mainly due to plural inelastic electron-scattering processes (black line). The background can be fitted at an energy window prior to the ionization edge, extrapolated to higher energies (red line) and subtracted from the spectrum.
(b) Core loss EEL spectrum after background correction.

tering processes. To subtract this background, a function is fitted at an energy window prior to the ionization edge (see red solid line in Figure 3.3 (a)). Different expressions can be used to describe this functional behavior[98,101]. For the most common function, also applied in the present work, the background intensity I, as a function of the loss energy E, is fitted using a power-law with two fitting constants A and r[98]:

$$I = A \cdot E^r. \tag{3.2.2}$$

The obtained function is then extrapolated to higher energies and subtracted from the spectrum. An example for a resulting background-corrected spectrum is depicted in Figure 3.3 (b).

For analyzing the ESI core loss measurements, the three-window method is used[98,102,103] in order to subtract the signal caused by inelastic scattering processes and take effects like varied sample thickness into account. In addition to the image acquired at the ionization edge energy (called post-edge image), two images at energies prior to the examined peak are acquired (denoted as pre-edge images). All three images have to be acquired with a certain energy width to ensure a good signal-to-noise ratio. After alignment of the three

images, each pixel of the two pre-edge images is fitted according to equation (3.2.2) and the extrapolated background is subtracted from the post-edge image to obtain a so-called elemental map.

Low Loss ESI

To resolve the problems described in the previous section, ESI in the so-called low loss regime, which is usually assigned to energies between $0\ \mathrm{eV}$ and $60\ \mathrm{eV}$, can be applied. In this energy range, electronic and plasmonic excitations take place. Since the cross section of these excitations is much higher, data collection times can be shorter than for core loss ESI, which leads to less problems due to beam damage and sample drift. Provided that adequate image analysis is applied, as it is described below, low loss ESI allows for discrimination of materials and phases with very similar spectral characteristics[104]. The main features of a low loss spectrum are the so-called zero-loss peak at $0\ \mathrm{eV}$ energy loss, as well as electronic excitations and a broad plasmon excitation.

Instead of measuring one image at a certain energy window to map individual elements, like for core loss spectroscopy, it is required to acquire a whole stack of images at different loss energies. A three-dimensional data set is obtained where the xy-plane contains the ESI images, while the z-direction denotes the loss energy. From a different point of view, the three-dimensional data set provides a spectrum for each image point. These spectra can then be analyzed.

After image alignment and before further processing, each pixel is normalized by dividing the pixel intensity value by the integral of the spectrum of the respective pixel to account for thickness variations. As described in Ref. [104], an analysis can be applied, which is based on nonlinear multivariate statistics and machine learning, to categorize each image pixel into specific spectral classes. The classification into distinct classes can be due to different reasons. For example, different elements, but also changes in morphology or other material properties, which influence electronic interactions and therefore the low loss spectrum, can lead to different classes[104]. When analyzing material composites, the electron excitation features of the averaged spectra for each spectral class can be compared with the EEL spectra of the neat materials to assign them to specific materials and material compositions.

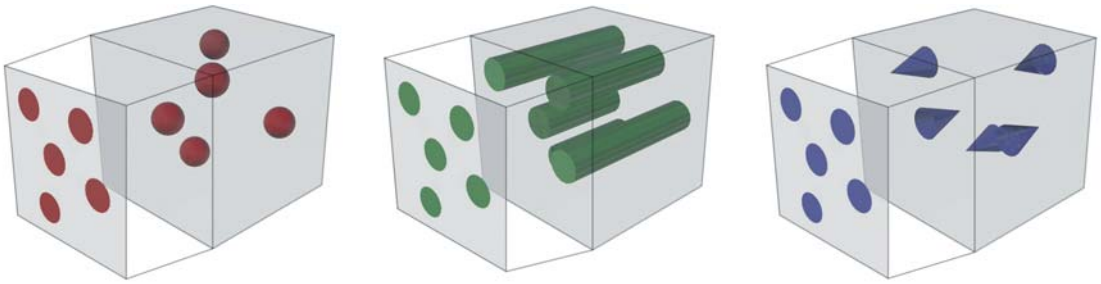

Figure 3.4: TEM images show projections of the sample. However, if this projection shows circles, the real objects might, for example, consist of sphericals, rods or cones.

3.2.1.2 Electron Tomography

Since bright-field images only show a projection of the specimen, they cannot provide information about the three-dimensional structure of the investigated thin films[105]. If circles appear in the image, the sample might consist of sphericals, but, for instance, rods or cones would also be supposable. This is schematically illustrated in Figure 3.4. To obtain three-dimensional information, electron tomography can be applied. One data collection scheme, which is often used, is the single axis tilt series. There, the sample is successively tilted into multiple angles (usually from $-60°$ to $+60°$ [105]) around one axis and at each angle, a TEM image is taken. To allow for image alignment and to take potential film deformations into account, gold nanoparticles, so-called gold-fiducials, are dispersed on both sides of the film. To be able to apply electron tomography, the projection requirement must be fulfilled. It states that the measured signal has to be a monotonic function of an object property[106]. Hence, for bright-field tomography, the sample has to be amorphous. If it would be crystalline, the beam intensity would depend on the angle of the impinging electron beam, because at certain angles, the condition for constructive interference would be fulfilled.

From the acquired tilt series, which provides projections at different angles, a reconstruction of the three-dimensional volume can be obtained. A variety of different algorithms exists to calculate this volume. In this work, the weighted backprojection algorithm[107,108] was used for the samples with $30\ \mathrm{nm}$ thickness. Backprojection is a Fourier reconstruction method, where the Fourier transforms of the projections are used to restore the Fourier transform of the object. Using inverse Fourier transformation, the real-space distribution

of the object is obtained. Due to the discrete sampling of projection angles there are more data points for low than for high frequencies. In the case of weighted backprojection, frequencies are weighted in such a way, that a balanced number of data points for all frequency ranges is obtained.
For reconstructions of samples with $100\ \mathrm{nm}$ thickness, presented in this work, application of the weighted backprojection algorithm led to severe distortions in the reconstructions. This issue was overcome by application of the TxBR algorithm, which is a further development of the weighted backprojection algorithm. Additionally, TxBR also led to a better contrast[109]. TxBR takes into account that electrons travel on curvilinear, rather than straight, trajectories, as well as the fact that the sample moves through inhomogeneous magnetic fields while being tilted. Comparison of the $30\ \mathrm{nm}$ thick sample, reconstructed with the weighted backprojection algorithm, with the $100\ \mathrm{nm}$ thick sample, reconstructed with TxBR, did not reveal significant differences. All samples with $30\ \mathrm{nm}$ thickness were reconstructed with the weighted backprojection algorithm, while for all $100\ \mathrm{nm}$ thick samples TxBR was applied.
Application of the reconstruction algorithm provides a three-dimensional image stack. With an isosurface function of a graphical software all pixels which have a grayscale value lower than a certain limit can be connected, so that a three-dimensional image is obtained.

3.2.1.3 Microscopes

Most TEM measurements, which will be described in section 4.1, were performed with a Libra 200 MC Cryo DMU (Carl Zeiss Microscopy) which provides high spatial and energetic resolution due to the combination of a monochromator and an in-column energy filter[110]. The TEM can be operated with acceleration voltages of $60\ \mathrm{kV}$ and $200\ \mathrm{kV}$. For $60\ \mathrm{kV}$ acceleration voltage the cross section, as well as the dispersion, is higher than for $200\ \mathrm{kV}$. Since this leads to an improved energy resolution for the ESI data set, low loss ESI measurements were performed at $60\ \mathrm{kV}$ acceleration voltage. However, higher acceleration voltages lead to longer mean free electron paths, thus reducing multiple scattering events[111]. Therefore, core loss spectroscopy measurements were acquired with $200\ \mathrm{kV}$. With regard to electron tomography, the effective thickness roughly doubles for the highest tilt angle and thickness effects become a severe issue for these measurements.

Since the samples mostly had a thickness of $100\ \mathrm{nm}$, electron tomography measurements were also performed with $200\ \mathrm{kV}$.
The goniometer of the Libra 200, which allows for tilting the samples during electron tomography measurements, exhibited technical difficulties at some point, which could not be solved until the end of the present work. Hence, electron tomography for two of the three $100\ \mathrm{nm}$ thick CBP samples doped with MoO_3 (see sections 4.1.3 and 4.1.4) was performed with the FEI Titan Krios™, also operated at an acceleration voltage of $200\ \mathrm{kV}$. The Titan Krios™ is a cryo microscope, where samples are held at a temperature of $100\ \mathrm{K}$ during the measurements. This is achieved by cooling of the copper wires, which are attached to the sample holder, using liquid nitrogen.
Since it could be deduced from FTIR measurements that cooling down the doped film does not have an impact on the topology of the sample, but only warming up influences the topology (see section 4.1.4), the different measurement temperatures of the two microscopes should not have affected the results. In addition, the reconstructions of two samples with $9\ \mathrm{vol}\%$ MoO_3 concentration and thicknesses of $100\ \mathrm{nm}$ respectively $30\ \mathrm{nm}$ were compared. No significant change in topology was observed, even though the first tilt series was acquired using the Libra 200 at room temperature while for the latter the Titan Krios was used at $100\ \mathrm{K}$.

3.2.2 Probing Electronic Properties

In the theses of Maybritt Kühn[49] (University of Darmstadt) and Tobias Glaser[112] (University of Heidelberg) PES and FTIR measurements were applied to probe the electronic properties of MoO_3-doped CBP layers. Since their results will be correlated with the results obtained within the scope of the current thesis, the working principles of these measurement techniques will be shortly summarized in the next two sections.

3.2.2.1 Photoelectron Spectroscopy

The underlying principle of PES is the photoelectric effect, where electromagnetic radiation is applied to knock out electrons into the vacuum. A schematic drawing, explaining the measurement principle, is depicted in Figure 3.5. Energy conservation requires that the incident photon energy $h\nu$ equals the sum of the binding energy of the electron with

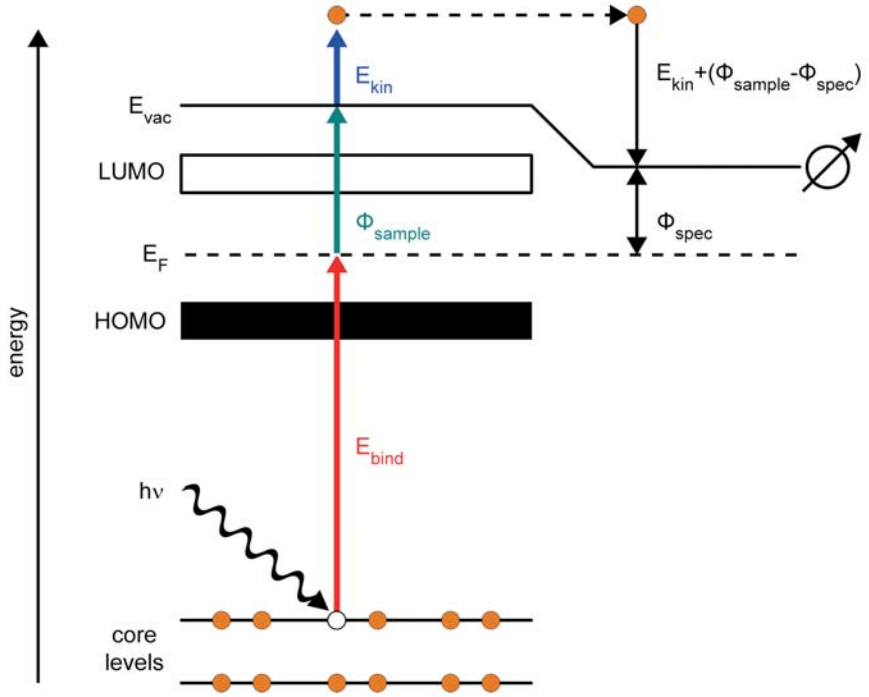

Figure 3.5: Principle of photoelectron spectroscopy. Energy conservation requires that the energy of the incident radiation equals the sum of the binding energy of the electron, the work function of the sample ϕ_{sample} and the kinetic energy of the detected electron E_{kin}. Additionally, also the work function difference of sample and analyzer has to be overcome.

regard to the Fermi level E_{bind}, the work function of the sample ϕ_{sample} and the kinetic energy of the detected electron E_{kin}, so that $h\nu = E_{\text{bind}} + \phi_{\text{sample}} + E_{\text{kin}}$ holds. Since spectrometer and sample are in electrical contact, the photoelectron has to overcome a contact potential difference of ϕ_{sample} - ϕ_{spec} on its way to the spectrometer. Therefore, the detected kinetic energy of the electron equals $\tilde{E}_{\text{kin}} = E_{\text{kin}} + (\phi_{\text{sample}} - \phi_{\text{spec}})$. After determining the work function of the spectrometer, by measuring a sample with a known work function (for instance a silver standard), the binding energy can be determined using the following correlation:

$$E_{\text{bind}} = h\nu - \tilde{E}_{\text{kin}} - \phi_{\text{spec}} \tag{3.2.3}$$

and is therefore independent of the sample work function.
Depending of the energy of the incident light one speaks about XPS or UPS. For UPS (ultraviolet photoelectron spectroscopy) ultraviolet light is applied to obtain information

about valence states. In the case of XPS (x-ray photoelectron spectroscopy) x-rays are used to probe the energies of deep lying core levels. Core level emission lines of XPS measurements are normally fitted using so-called Voigt functions[3]. The binding energy also depends on the chemical environments of the atoms. This is often referred to as chemical shift.
PES is a very surface-sensitive technique, since the mean free path of photoelectrons λ at the applied energies is quite low. For UPS it typically amounts to about $3\lambda \approx 15$ Å[55,113]. If a thin layer with a thickness d is evaporated onto a substrate, the integral intensity of the substrate emission line is reduced. With I_0 being the intensity of the substrate emission line before film deposition, the damped intensity I is given by:

$$I = I_0 e^{-d/\lambda}. \tag{3.2.4}$$

This equation can be used for determination of layer thicknesses of the investigated films from the damping of peak intensities.
A more detailed description about PES theory can, for example, be found in Refs. [114] and [115], whereas information about the experimental setup, used for measurements shown in this work, can be found in Ref. [116].

3.2.2.2 FTIR Spectroscopy

Another method to investigate electronic properties of organic thin films is FTIR spectroscopy. For the measurements shown in this work, a Michelson interferometer setup was used, where the incoming IR radiation is divided into two beams by a beam splitter. After reflection of one beam at a fixed mirror, while the other one is reflected at a movable mirror, both beams are merged and interfere. In the case of transmission mode, the interfered radiation is transmitted through the sample and its intensity is measured as a function of the mirror position. For spectral decomposition of the IR radiation, Fourier transformation is applied to the acquired interferogram, to obtain a spectrum (intensity as a function of the wave number). A more detailed description about FTIR theory can, for example, be found in Refs. [117] and [112]. The latter also contains a detailed description of the experimental setup.

[3] A superposition of a Gauss curve with a Lorentz function.

An experimentally obtained FTIR spectrum of an organic film exhibits absorption peaks caused by excitations of molecular vibrations in the so-called fingerprint region ($600\ \mathrm{cm}^{-1}$ to $1700\ \mathrm{cm}^{-1}$), whereas broad absorptions can be found at higher wave numbers, which are due to electronic excitations. The energetic positions of the vibrational bands depend in a simple model on the binding strengths of the molecular bonds, as well as the mass of the participating atoms.
The IR spectrum of single molecules in the gas phase can also be calculated quantumchemically using DFT. Comparison of the measurements with the calculations can lead to a better understanding of the experimental spectra. Reasons for deviations of theory and experiment might, for example, be due to intermolecular interaction and inharmonic effects, which are usually taken into account in the DFT calculations. The exact parameters used for the quantumchemical calculations can be found in Refs. [112] and [118].

3.2.3 Electrical Measurements

In the present section the experimental setups for electrical measurements will be described. Prior to all electrical measurements, silver conductive paint was applied to the device contacts. Except for the cryo-IV measurements, all electrical measurements were performed in ambient air and the devices were contacted using a manual point probe station.

3.2.3.1 IV and Cryo-IV Measurements

The IV characteristics, which will be shown in section 4.3.1, were conducted using a semiconductor parameter analyzer (4155C from Agilent), whereas the measurements of the hole-only devices, presented in section 4.3.3, were acquired with a Keithley 2400 source meter[4]. In both cases three consecutive measurements were performed to ensure that no degradation occurred during measurements. Additionally, a check for hysteresis effects starting from $0\ \mathrm{V}$ was performed, to check whether the IV characteristics were symmetric for forward and reverse bias.

[4]The Keithley 2400 was used at the beginning of this thesis, since the laboratory, where all measurements presented in this work were conducted, had to be set up first and the semiconductor parameter analyzer was not available from the beginning.

Additionally to the IV measurements performed at room temperature, measurements at various temperatures were conducted for selected samples, to determine activation energies (see section 4.3.2). The samples were cooled down in vacuum inside a cryostat (Model ST-100 Supertran System of Janis Research) using liquid nitrogen. To ensure good thermal contact, grease (Apiezon type N) was applied to the back of the sample. The temperature was adjusted via counter heating using a temperature controller (Lake Shore Model 331). For measurements of the IV characteristics a source meter (Keithley Model 2636A), was used. The IV characteristics were measured three times for each temperature to test for degradation.

3.2.3.2 OLEDs

LIV[5] characteristics of OLEDs were recorded under ambient conditions using a Keithley 2400 source meter. For the measurements of the optical power, outcoupled through the ITO-back contact, a silicon photodiode (Newport, Model 818-UV) which was located below the probe station and connected to a powermeter (model 1936) was used. To allow for conversion into photometric units, calibration measurements were performed with a luminance meter (Konica Minolta, CS-200).

3.3 Sample Preparation

In the following section the sample preparation will be described. This includes general aspects of thin film growth, a short overview of the materials, which were used for doped films, and a description of the preparation of TEM samples as well as electrical devices.

3.3.1 Thin Film Growth

Prior to thin film growth or spincoating, all substrates where cleaned for $10\ \mathrm{min}$ with acetone and isopropanol in an ultrasonic bath and afterwards blown off with gaseous nitrogen. The final cleaning step was an ozone treatment for $10\ \mathrm{min}$ to remove organic contaminants. Instead of the ozone treatment, the OLEDs shown in chapter 5 were exposed to oxygen plasma for $5\ \mathrm{min}$ (Plasma technology, $300\ \mathrm{W}$)[119]. Plasma treatment is

[5] Luminance L, Current I, Voltage V

also known to enhance the work function of ITO, which might allow better hole injection and therefore increase the efficiency. Basically the same effect can also be achieved with ozone treatment, but was found to be less effective[119].
Samples were grown via thermal evaporation from effusion cells in the integrated UHV system described in section 3.1. The organic and co-evaporated layers of the hole-only devices where fabricated in OLED chamber 2 (base pressure: 10^{-8} mbar), for OLEDs organic chamber 1 (base pressure: 10^{-9} mbar) was used. MoO_3 injection layers were evaporated from evaporation boats in the metal chamber, where also aluminum electrodes and LiF injection layers were processed.
Doped samples were prepared via co-evaporation of the single materials where the rates of the two materials could be monitored with two independent quartz crystals. Neat films were evaporated with a growth rate of 50 Å/min. Only for the samples, which were prepared in the FTIR chamber, a deposition rate of 30 Å/min had to be chosen due to restrictions of the evaporation cells used in this chamber. For the doped films the deposition rate of CBP was kept constant at 50 Å/min and the MoO_3 rate was adapted accordingly to attain the desired doping concentration.
To calculate the doping concentration in volume per cent $C_{\text{vol\%}}$ from the film thicknesses of the matrix d_{matrix} and the dopant d_{dopant} the following equation was used:

$$C_{\text{vol\%}} = \frac{d_{\text{dopant}}}{d_{\text{dopant}} + d_{\text{matrix}}} \cdot 100. \tag{3.3.1}$$

For the discussion about charge transport and doping efficiency it is more suitable to consider the molar particle ratio. Using mass spectroscopy, Berkowitz et al.[120] found that, when thermally evaporated, the MoO_3 vapor consists mainly of Mo_3O_9 clusters. Therefore, all molar doping concentrations in this work are referred to Mo_3O_9 trimers. From the thicknesses of the two materials the molar doping concentration $C_{\text{mol\%}}$ can be calculated if the densities of matrix ρ_{matrix} and dopant ρ_{dopant} as well as their molar masses M_{matrix} and M_{dopant} are known:

$$C_{\text{mol\%}} = \frac{\frac{d_{\text{dopant}} \cdot \rho_{\text{dopant}}}{3 \cdot M_{\text{dopant}}}}{\frac{d_{\text{dopant}} \cdot \rho_{\text{dopant}}}{3 \cdot M_{\text{dopant}}} + \frac{d_{\text{matrix}} \cdot \rho_{\text{matrix}}}{M_{\text{matrix}}}} \cdot 100 \tag{3.3.2}$$

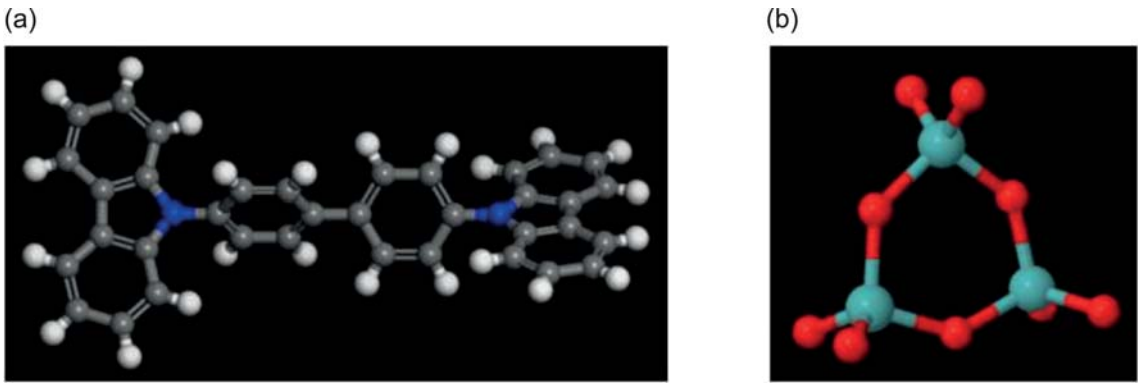

Figure 3.6: (a) Structure of the organic matrix material CBP.
(b) Structure of the dopant molybdenum oxide. It was found that molybdenum oxide mainly evaporates as Mo_3O_9 clusters[120].

According to the manufacturer, the molar masses are $M_{\mathrm{CBP}} = 484.59\ \mathrm{g/mol}$ and $M_{\mathrm{MoO_3}} = 143.94\ \mathrm{g/mol}$. Following Refs. [112] and [121], the material densities $\rho_{\mathrm{CBP}} = 1.7\ \mathrm{g/cm^3}$ and $\rho_{\mathrm{MoO_3}} = 4.1\ \mathrm{g/cm^3}$ were assumed.

3.3.2 Materials

The material system, mainly studied in this work, is the organic host material CBP and the dopant molybdenum oxide. In this section a short description of these two materials is presented.

3.3.2.1 CBP

In the present work, CBP is used as organic host material for electrochemically doped layers, which are p-type doped with molybdenum oxide. The elemental formula of CBP is $C_{36}H_{24}N_2$ and its chemical structure is shown in Figure 3.6 (a). CBP acts as a representative of a whole class of organic wide-bandgap materials, as, for example, TCTA or α-NPD[6] and is widely employed in phosphorescent OLEDs. There, it is often used as host for the green phosphorescent emitter $Ir(ppy)_3$[23,122,123], but also as host for electrochemically doped charge transport layers[32,77]. Since the mobility for both, holes ($2 \cdot 10^{-3}\ \mathrm{cm^2/Vs}$[124]) and electrons ($3 \cdot 10^{-4}\ \mathrm{cm^2/Vs}$[124]), is comparable, CBP is an ambipolar material capable of transporting holes as well as electrons.

[6] For α-NPD sometimes also the abbreviation NPB is used.

3.3.2.2 MoO_3

Semiconducting TMOs like MoO_3, WO_3, V_2O_5 or ReO_3 are compatible with the field of organic electronics since they can be evaporated from the same simple effusion cells as organic semiconductors and even wet-processing from a nanoparticle dispersion is possible[79,125]. Besides, they possess high transparency in the visible spectral range[82]. TMOs are most widely applied as thin injection layers for OLEDs and OPV. The first MoO_3 injection layer was reported in 1996[75]. In addition, TMOs can also be applied as p-type dopant for organic semiconductors with very deep lying HOMO levels due to their high electron affinities. In the present work, molybdenum oxide is used because of its low sublimation temperature of only about $400°C$, which does not require special high-temperature effusion cells as for the other TMOs mentioned above, and due to its low costs. According to the terminology usually used in literature, also in this work molybdenum oxide will usually be abbreviated by MoO_3, even though it is assumed throughout the whole thesis that mainly Mo_3O_9 clusters are present (see Figure 3.6 (b)).

3.3.3 Preparation of TEM Samples

For the preparation of the TEM samples, filtered ($45\ \mu m$ particle filters) PEDOT:PSS was spincoated under ambient conditions onto ITO-coated borofloat glass with $2500\ rpm$. Afterwards, the organic film was evaporated on top of the PEDOT:PSS in the integrated UHV system, which was described in section 3.1.
After evaporation, the sample was placed in demineralized water. Since PEDOT:PSS is water-soluble, the evaporated film swims on top of the water and can then be picked up with a TEM grid. So called Quantifoil® grids were used, which consist of a copper grid, coated with a thin holey carbon film for support.
For pure MoO_3 the floating process did not work since the film fell apart into very small pieces on the water surface, which were not big enough to be picked up with a TEM grid. Therefore, to obtain EEL spectra of neat MoO_3, a sample with $70\ nm$ MoO_3, evaporated onto a $20\ nm$ thick CBP film, acting as supporting layer, was fabricated. CBP does not contain any oxygen. Hence, this sample was suitable for acquiring core loss spectra of neat MoO_3, which then only contained signal from the MoO_3 film and not from CBP. In the low loss regime one would get signal from both materials, i.e. CBP and MoO_3.

Therefore, the MoO_3 film was directly deposited onto the Quantifoil® grid, so that the spectra had to be recorded with Quantifoil® background. To ensure comparability, low loss EEL spectra of neat CBP were also recorded with Quantifoil® background, floated as usual.
For electron tomography, gold fiducials were applied on both sides of the film after the floating process. A nanoparticle solution, purchased from Aurion, containing gold nanoparticles with a nominal diameter of about $6\ \mathrm{nm}$, was used. The nanoparticle solution was mixed with deionized water at a concentration of 1:1. To achieve homogeneously dispersed gold fiducials on the sample surface, the film was exposed to oxygen plasma[7] ($50\ \mathrm{W}$) for $6\ \mathrm{s}$ prior to application of the gold nanoparticles. To ensure that the samples were not damaged and no structural changes occurred during the whole process, a bright-field image was acquired after each process step.

Influence of Floating Process on Film Thickness

Significant discrepancies between layer thicknesses, determined via oscillating crystals during evaporation and by electron tomography, were found. For a sample with $30\ \mathrm{nm}$, electron tomography revealed a thickness of about $15\ \mathrm{nm}$[8], whereas reconstructions of three films with $100\ \mathrm{nm}$ thickness revealed thicknesses of about $60\ \mathrm{nm}$ to $80\ \mathrm{nm}$ in the tomography. Therefore, the question arises, what the origin of these quite big discrepancies is.
One possible explanation would be, that during the plasma treatment prior to application of the gold fiducials or in the application process of the gold fiducials itself, parts of the organic films were removed. This supposition was disproved since thickness maps, acquired before and after the described processes, did not reveal significant thickness changes.
Usually glass is used as substrate for tooling of the evaporation cells, not PEDOT:PSS. Therefore, a different substrate might also influence the sample thickness. However, this assumption was also disproved by an experiment where $100\ \mathrm{nm}$ thick films of neat CBP respectively MoO_3 were evaporated onto a glass, as well as an ITO substrate covered with

[7] Gatan Solarus (Model 950) Advanced Plasma Cleaning System
[8] Because the contrast between CBP and air in the electron tomography results is not very good, the exact sample thickness can only be estimated with the use of the gold fiducials.

PEDOT:PSS. For both substrates, profilometer measurements revealed the same sample thickness, namely about $100\ \mathrm{nm}$.
Another explanation could be that the floating process already influences the sample thickness. To check whether this is the case, film thicknesses were determined from FIB-milled cross sections, which were prepared in the Auriga system of the clustertool. Two samples were prepared by evaporating a $100\ \mathrm{nm}$ thick CBP:MoO_3 film with $45\ \mathrm{vol}\%$ doping concentration onto PEDOT:PSS-coated ITO glass. For one of the two samples the organic film was first floated off onto a TEM grid, as described earlier in this section. Using carbon tape, it was then attached to a piece of glass for fixture. A $100\ \mathrm{nm}$ thick aluminum layer was evaporated on top of both samples to protect the underlying organic layer and obtain sharp, milled edges. A cross section of the unfloated film revealed a thickness of about $100\ \mathrm{nm}$. Figure 3.7 (a) shows an overview of the floated TEM sample, where the Quantifoil® grid is covered by floated CBP:MoO_3 film fragments. In Figure 3.7 (b), a FIB cross section, which was milled through the carbon support film of the Quantifoil® grid and one of its holes is shown. It can be seen that the organic film, supported by the carbon film, covers the hole. Milling of crossections at different positions of the samples revealed thicknesses between $50\ \mathrm{nm}$ and $70\ \mathrm{nm}$. This is in accordance with the discrepancies observed by electron tomography, as mentioned above. The differences of the measured film thicknesses of the floated sample are probably due to the fact that the film distortion has a quite high deviation, depending, for instance, on the size of the floated film fragments. In addition, the method does not allow to determine thicknesses with a nm accuracy, but there is a discrepancy of approximately $5\ \mathrm{nm}$ due to the weak contrast between the investigated materials. Nonetheless, the result reveals that the film is extended during the floating process. It can be expected that the observed topology does not change but only a deformation occurs. Therefore, for interpretation of TEM images of floated films, possible distortions must always be taken into account.

3.3.4 Device Fabrication

All substrates used for devices had a thickness of $0.7\ \mathrm{mm}$ and were $25\ \mathrm{mm}$ x $25\ \mathrm{mm}$ in size. The sample holders used in organic chamber 1 and 2, as well as in the metal chamber, were able to carry two of these substrates at the same time. For device fabrication, laser-cutted shadow masks with a thickness of $300\ \mu\mathrm{m}$ and a lateral accuracy of $2-3\ \mu\mathrm{m}$,

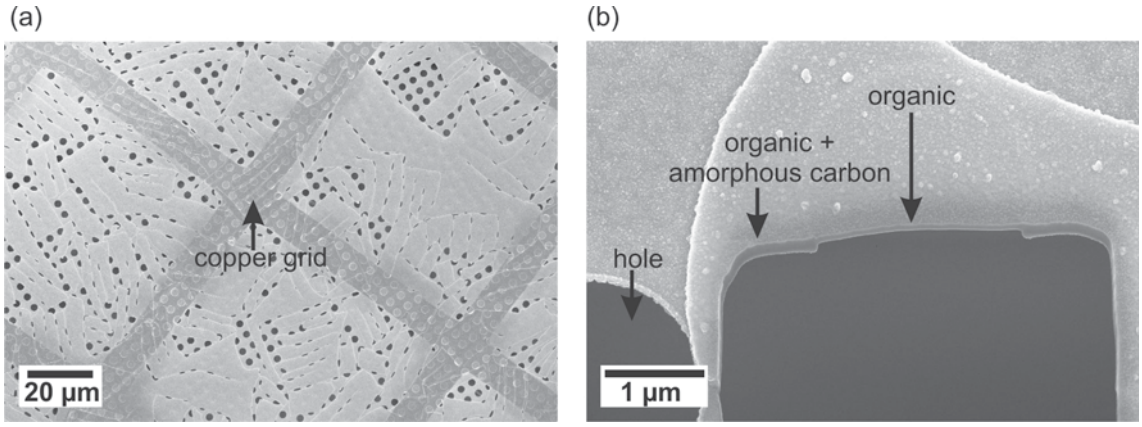

Figure 3.7: (a) SEM image which shows an overview of a floated sample. The Quantifoil® grid, consisting of a copper grid coated by a thin holey carbon film for support is covered by floated CBP:MoO_3 film fragments.
(b) FIB crossection, milled through the carbon-support film of the Quantifoil® grid and one of its holes, which is covered by the floated CBP:MoO_3 film.

were used to define active areas and contacts. The masks were fixed onto the sample holders with small screws and exchanged under nitrogen atmosphere in the glovebox of the integrated UHV system.

3.3.4.1 Hole-Only Devices

For hole-only devices, borofloat glass from Schott was used as substrate. Two different kinds of device structures were fabricated. Anode, organic layer and cathode were defined with shadow masks, respectively.
The first device structure was a so-called stripe structure, which is schematically shown in Figure 3.8 (a). The anode stripe was defined by a shadow mask (red). Afterwards, the mask was changed and the organic layer was evaporated (green). The cathode, consisting of a stripe perpendicularly oriented to the anode stripe, was defined by a third shadow mask (orange) in the last step. Because of the low lateral conductivity of the organic layers, the active zone is defined by the overlap of the two electrodes and current flow occurs perpendicularly to the substrate, when a voltage is applied between the two contacts. The second structure was a so-called finger structure. As depicted in figure 3.8 (c), it consists of an organic layer (green) and an electrode with interdigitated metal stripes (orange). In

this case, current transport takes place parallel to the substrate, when a voltage is applied between the two contacts. On each substrate, four devices of the same structure were fabricated simultaneously. Since the sample holder of the FTIR chamber is just capable of carrying one substrate of the size $12.5\ \mathrm{mm}$ x $12.5\ \mathrm{mm}$, only two devices with the stripe structure could be fabricated there.

The layer sequences are illustrated in Figure 3.8 (b) and (d). For the stripe structure, positive bias was applied to the bottom electrode, which consisted of aluminum and a thin MoO_3 layer to enhance hole injection, as described in section 2.5.1. Electron injection from the top electrode is negligible, since the high injection barrier for electrons between the aluminum top contact and CBP is even increased by inserting another thin MoO_3 interlayer. Therefore, injection issues should only play a minor role, so that mainly the current transport through the doped layer can be investigated. Considering transport within the CBP matrix, it can be assumed that only hole transport takes place in these devices[36]. In order to obtain a stack with the same material sequence, the finger structure consisted of a $100\ \mathrm{nm}$ thick organic layer, followed by a $5\ \mathrm{nm}$ thick MoO_3 layer and a $100\ \mathrm{nm}$ thick aluminum electrode. To allow for a better comparison of stripe and finger devices, the organic layers of both device structures, as well as the cathodes of the stripe devices and the electrodes of the finger devices, were prepared simultaneously on the same sample holder for each doping concentration. Sometimes only one kind of device structure was fabricated, for example because a TEM sample was fabricated within the same evaporation process and the sample holder did not allow to additionally fix two device substrates.

Various factors can influence the measured IV characteristics. In Ref. [126], the influence of the evaporation rate, which goes along with a variation of the evaporation temperature, was studied. It was found that when MoO_3 is deposited at low deposition rates, the work function was lower and more oxygen deficiencies were present than for high deposition rates, where MoO_3 became almost stoichiometric. It was also demonstrated that the evaporation temperature influences the charge transport properties, since OLEDs with a MoO_3 injection layer evaporated at low temperatures exhibited higher currents at the same voltage levels than OLEDs where MoO_3 was evaporated at a high temperature[126]. Because different rates were used for different MoO_3 concentrations in this work (the CBP rate was kept constant during evaporation for all films (see section 3.3.1)) and the evaporation temperature might also depend on the filling level of the evaporation cells,

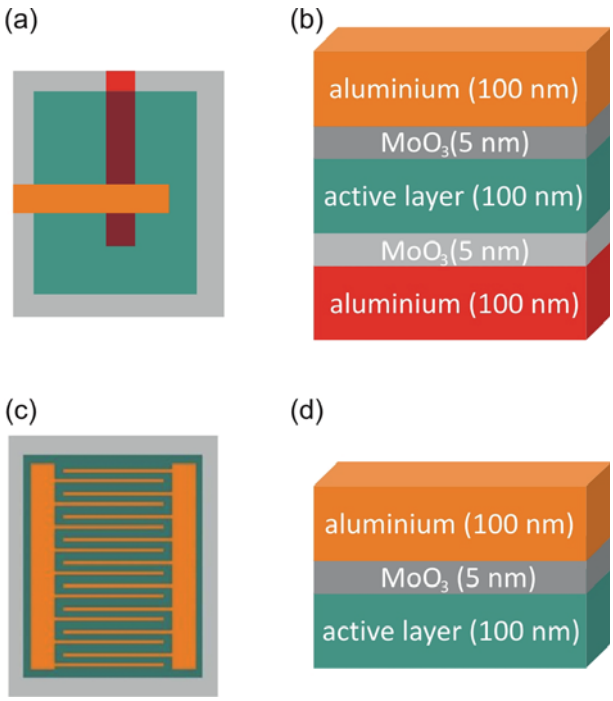

Figure 3.8: Structures of hole-only devices where (a) current flows perpendicular to the substrate (stripe structure) or (c) parallel to the substrate (finger structure) when a voltage is applied. Layer sequences for (b) the stripe structure and (d) the finger structure.

this might influence the measured IV characteristics. However, since the active layers of finger and stripe devices were deposited simultaneously for each doping concentration, the above mentioned effects are not expected to severely influence the results regarding the differences in conductivity of finger and stripe structures.

Measurements in this work were conducted in ambient air. It is known that electronic properties of organic materials and TMOs might change upon exposure to air. Meyer et al. showed, that exposure of MoO_3 to ambient air for a few minutes already reduces the work function by about $1\ \mathrm{eV}$[127]. For polymer films doped with MoO_3 it was also shown that conductivity and mobility of doped films, as well as bandgap and work function of MoO_3, depend on the degree of nitrogen exposure[128]. However, it was shown that charge injection from MoO_3 into high-work function materials as, for example, α-NPD or TFB is not significantly affected by air exposure, since the lowering in work function

only changes the interface dipole, but does not affect the energy barrier between the two materials[127].

For the first fabricated stripe devices, a device structure with an active area of $7\ \mathrm{mm}^2$ was used. However, it turned out that for high doping concentrations, which result in high conductivities, i.e. low resistances, the measurements were influenced by contact resistance effects. This means that the sample resistance was higher than or at least comparable with the resistance of the measurement setup, including contact pins and wiring, so that a superposition of both was measured. The effect was found to be even stronger for the temperature dependent IV measurements, which will be presented in section 4.3.2, since the setup used there exhibits a higher contact resistance. Therefore, a new device layout was introduced later with an active area of $0.0625\ \mathrm{mm}^2$, to enhance the resistance. The contact resistance effect could be demonstrated, for example, for a sample with $33\ \mathrm{vol}\%$ MoO_3 concentration, where no significant temperature dependence regarding the IV characteristics was found for the old layout, whereas the new one showed a characteristic temperature dependence. However, for low doping concentrations, no significant discrepancy between the two layouts was found.

There is also a lower limit for current measurements, which is also more severe for temperature dependent measurements. This is due to the fact that the sample resistance increases significantly for lower temperatures because of the temperature activated hopping transport. It might then be difficult to measure such low currents since the measurement is limited by the accuracy of the analyzer. Another factor which has to be taken into account is that the sample can be considered as a capacitor. Therefore, it requires a certain charging time τ, which depends on the resistance R and the capacitance C. This leads to an additional charging current which overlaps with the actual current and increases the measured signal. The effect becomes important for small currents. This could be verified for the cryo-IV setup (see section 3.2.3.1) by enhancing the hold time, i.e. the time between applying a voltage and measuring the respective current, for each data point, where the above described effect became weaker. Additionally, there must also be other effects which influence the measurements, like the presence of small leakage currents which become significant for low measurement currents.

3.3.4.2 OLEDs

For the OLEDs described in chapter 5, commercially fabricated substrates[9] with ITO anodes were used. The active area was already pre-patterned with a photoresist passivation, which defines 16 active areas with a size of $4\ \mathrm{mm}^2$. Each ITO anode is connected to a metal contact at the substrate edge. A shadow mask, which covers anode and cathode contacts, was used during growth of the MoO_3 injection layers and the organic layers. During deposition of the LiF/aluminum contact, another mask was used, which covered the anode contacts and left the metal pads for contacting the cathode contacts blank. Since the evaporated metal cathodes were opaque, light outcoupling mainly occurred through the transparent ITO anode.

[9] The substrate structure was designed by Osram OS and provided by BASF SE.

4 MoO_3-Doped CBP Thin Films

In the first part of this chapter, the topology of MoO_3-doped CBP films is investigated with different measurement techniques of transmission electron microscopy. The second section summarizes the main results on the electronic properties of CBP:MoO_3 composites inferred from FTIR and PES measurements. Then electrical measurements of doped CBP films are presented. In the last part, a comprehensive picture, considering all experimental findings of the previous sections, regarding structural, electronic and electrical results, is drawn.

4.1 Structural Investigations

In the following section, TEM results will be presented to reveal information about the topology of co-evaporated CBP films doped with MoO_3. First, bright-field TEM was used, which will be shown to point towards agglomeration of the dopants in the organic matrix. To verify that the observed agglomeration structures consist of MoO_3, TEM spectroscopy in the core loss and in the low loss regime was applied. In the next step, electron tomography was employed to obtain three-dimensional structural information. Furthermore, the influence of the substrate temperature on the topology was examined. Based on all investigations, a model for the agglomeration growth will be developed. All TEM measurements were performed and to a large part also analyzed at the University of Heidelberg in the group of Prof. Rasmus R. Schröder, mainly by Martin Pfannmöller, Anne K. Kast and Dr. Levin Dieterle.

4.1.1 Bright-Field TEM

As already mentioned in section 1.1, one explanation for the low doping efficiency observed in MoO_3-doped CBP films would be agglomeration of the dopants. Evidence for clustering of MoO_3 was already found by Ha et al.[129]. STM measurements on the sur-

face of samples with MoO_3 deposited onto pentacene revealed small MoO_3 clusters with a height of $4 - 6$ Å and a diameter of $15 - 20$ Å, as well as larger clusters, 25 Å in height and up to 90 Å in width. Since STM is a surface-sensitive technique, only insight about the surface topology can be obtained. To investigate the bulk properties of doped films, transmission electron microscopy was therefore applied within the scope of this work.
Figure 4.1 shows TEM bright-field micrographs of CBP samples with 0.6 vol%, 2 vol%, 9 vol% and 33 vol% in plane-view perspective. All samples had a thickness of 30 nm. Since the samples possess negligible phase contrast, the images in Figure 4.1 were acquired with slight under focus to enhance contrast. As all bright-field images presented in this work, they were zero-loss filtered. This means the images were recorded using only electrons from the zero-loss peak, thus eliminating information from inelastic scattering processes.
In the bright-field images, dark spots could be observed which potentially represent MoO_3 agglomerations. This also confirms results of Lee et al.[131] who performed HAADF measurements and reported the same effect for CBP and α-NPD doped with MoO_3 and ReO_3. Also for CuPc doped with WO_3 dopant precipitates could be observed via HAADF measurements[67].
To estimate the size distribution and mean distance of the agglomerates, power spectral density (PSD) analysis was applied, as described in Ref. [132]. In the PSD spectra, shown in Figure 4.2, two main peaks can be identified. The fact that a spread of agglomeration sizes and distances is present in the images is reflected in broad peaks and the values given below should therefore only be seen as mean values. The feature at higher frequencies can be assigned to the mean lateral agglomeration size, which is almost the same for all investigated doping concentrations (see dashed line) and amounts to about 1 nm. The peaks at lower frequencies belong to the mean distance of the agglomerations and are 12.7 nm, 7.1 nm and 4.6 nm for 2 vol%, 9 vol% and 33 vol%, respectively (solid lines). This indicates that the agglomeration density increases with increasing doping concentration. For 0.6 vol% no peak, which represents the agglomeration distance, can be identified. This is probably due to the fact that there is a quite high spread in distances and that the distance is higher than the resolution limit of the PSD. Section 4.1.5 will go into more detail whether the diameters determined from bright-field images reflect the exact agglomeration size.

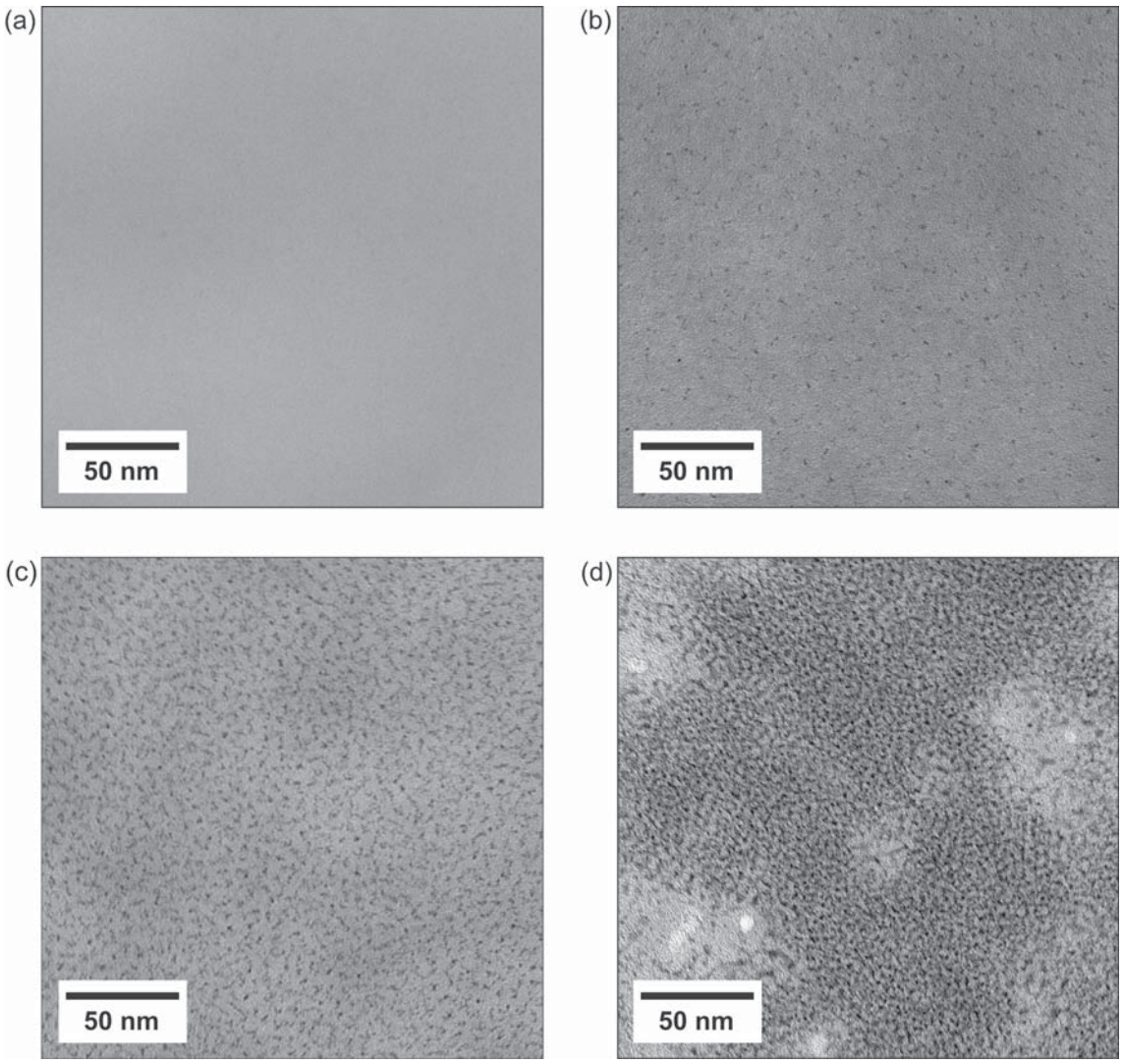

Figure 4.1: Zero-loss filtered TEM bright-field micrographs of CBP films doped with (a) 0.6 vol%, (b) 2 vol%, (c) 9 vol% and (d) 33 vol% MoO_3. All films had a thickness of 30 nm.[130]

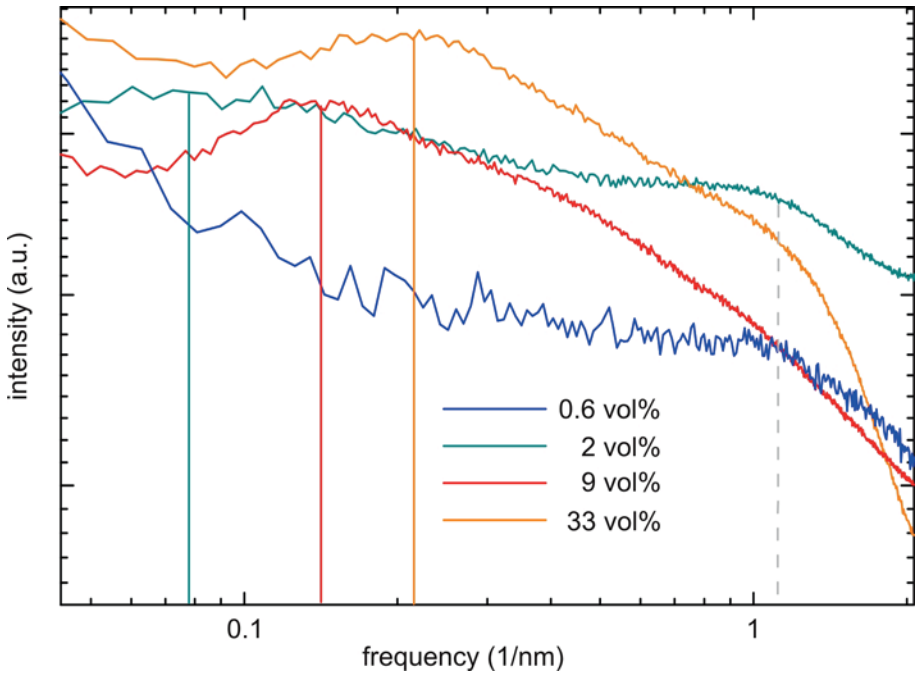

Figure 4.2: Power spectral density calculations of the bright-field images shown in Figure 4.1 reveal a filament diameter of about $1\ \mathrm{nm}$ for all doping concentrations and an increasing mean agglomeration size for increasing doping concentration.

To investigate the morphology of neat and doped films, they were analyzed using Debye electron diffraction. Zero-loss filtered diffraction patterns were acquired for different doping concentrations. The contrast inverted result for a CBP sample with $9\ \mathrm{vol\%}$ MoO_3 concentration is displayed in Figure 4.3. Comparable results were obtained for neat CBP and MoO_3 films and for a doped film with $33\ \mathrm{vol\%}$ doping concentration (not shown here). In all diffraction patterns only diffuse concentric circles appear, indicating that neat films, as well as doped films, are widely amorphous.

4.1.2 TEM Spectroscopy

As already described in section 3.2.1.1, the contrast in a bright-field image can be due to various effects. Therefore, energy-filtered TEM was applied to clearly identify MoO_3 in the bright-field micrographs.

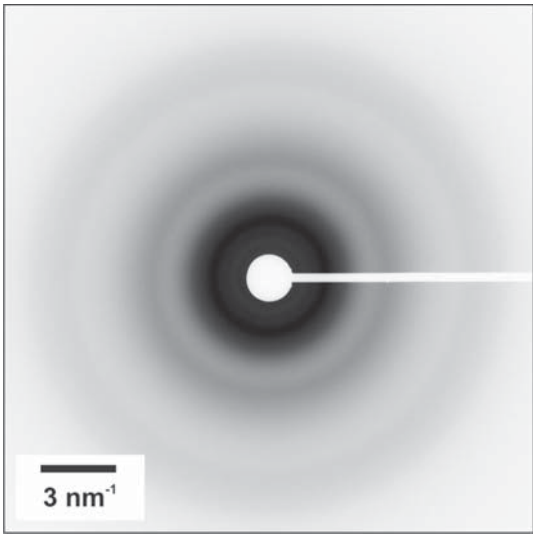

Figure 4.3: Zero-loss filtered diffraction pattern for a CBP sample doped with 9 vol% MoO_3.[130]

4.1.2.1 ESI in the Core Loss Regime

As described in section 3.2.1.1, core loss spectroscopy is one possibility to obtain chemical contrast in a TEM image. Since CBP does not contain any oxygen, the oxygen K-edge of MoO_3 at 532 eV[111,133] was used to map the MoO_3 distribution within the CBP matrix. Figure 4.4 shows background corrected EEL spectra of the oxygen K-edge at around 532 eV for neat CBP and MoO_3 films, as well as for a CBP film doped with 33 vol% MoO_3. All spectra were normalized with respect to the peak labeled with A. For pure MoO_3, a very distinct energy loss spectrum can be detected. Two features appear at 532 eV and 541 eV and are labeled with markers A and B. Compared to the neat MoO_3 film, the spectrum of the doped film only shows minor differences in the intensity ratio of peak A and B. Since no fundamental spectral shifts or changes in spectral intensity occur, when comparing neat and doped films, it can be concluded that co-evaporation does not significantly influence the stoichiometry of MoO_3[133]. As expected, the CBP spectrum does not show any feature in this energy range. Hence, for ESI imaging the energy of the oxygen K-edge of MoO_3 can be applied to study the oxygen distribution and therefore the distribution of MoO_3 .

As elaborated in section 3.2.1.1, the three-window method was used with an energy window of 30 eV, and pre-edge images at 484 eV and 514 eV. The result of the ESI measurement is displayed in Figure 4.5 (b), where regions with low spectral intensity are assigned to CBP and depicted in black, whereas regions with high spectral intensity are assigned

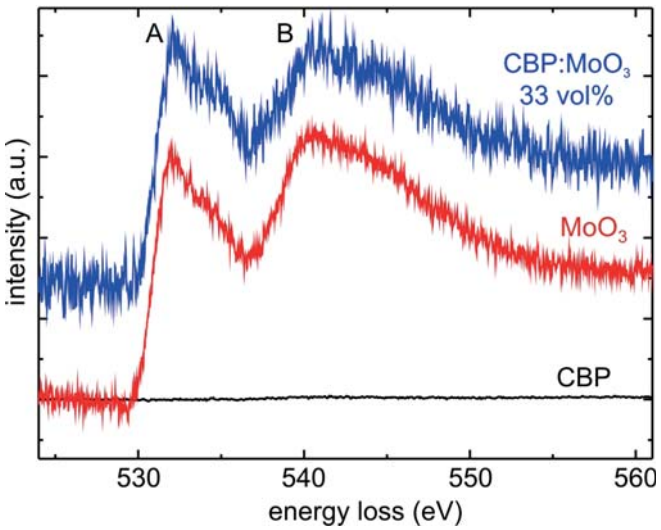

Figure 4.4: Background-corrected EEL spectra of the oxygen K-edge of 70 nm thick pristine CBP (black) and MoO_3 (red) films. The doped CBP:MoO_3 film with 33 vol% (blue) had a thickness of 30 nm. All spectra were normalized with respect to the peak labeled with A. Because for the pure MoO_3 film the floating process did not work (see section 3.3.3), 20 nm CBP was deposited underneath the MoO_3 film.[130]

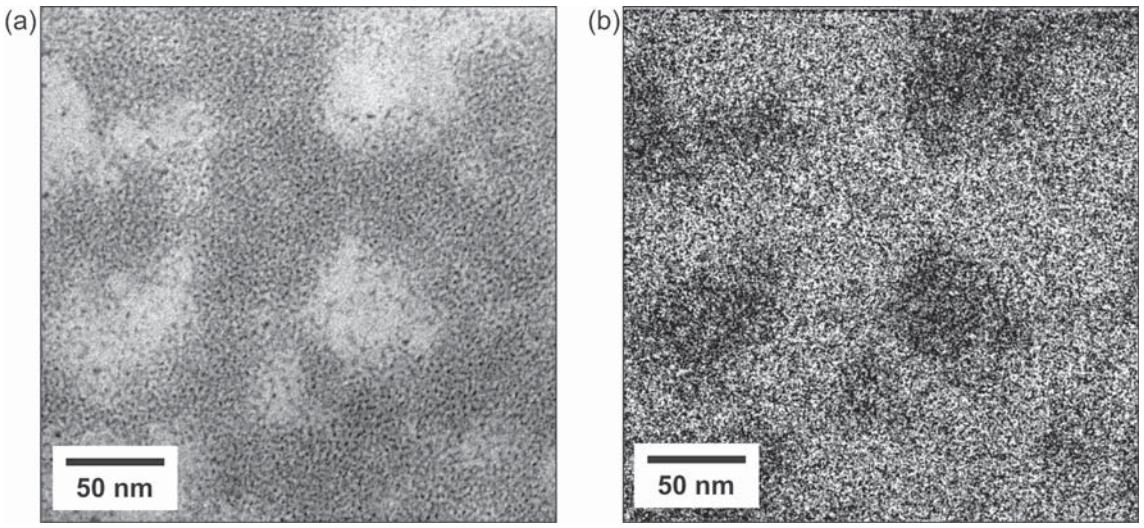

Figure 4.5: (a) Bright-field image of a CBP sample with 33 vol% MoO_3.
(b) Corresponding ESI core loss map of the oxygen K-edge, where bright regions can be assigned to MoO_3, whereas dark regions depict CBP.[130]

to MoO_3 and depicted in white. This result can be compared with the corresponding bright-field image in Figure 4.5 (a). A very good correlation between both measurements is found, since the areas with high spectral intensity correlate with the dark spots in the bright field image and less signal in the ESI image is obtained at the brighter regions of the bright-field image. This leads to the conclusion that the contrast in the bright-field image is really due to different materials and that MoO_3 and CBP can already be discriminated from the information in the bright-field images.

4.1.2.2 ESI in the Low Loss Regime

The ESI results presented in the previous section were quite noisy since core loss spectroscopy exhibits different difficulties as described in section 3.2.1.1. The most severe problem is that sample drift becomes crucial in this measurement mode due to long data collection times which are needed for core loss ESI. To overcome this problem, low loss ESI can be performed instead, where much shorter acquisition times are required.
As described in section 3.2.1.1, a stack of images was acquired for energies between $3\ \mathrm{eV}$ and $60\ \mathrm{eV}$ in $1\ \mathrm{eV}$ steps with a slit aperture of $1\ \mathrm{eV}$. The resulting raw data set can be found in the Supporting Information of Ref. [110] where each image represents a specific loss energy, starting with $3\ \mathrm{eV}$. Data analysis of this image stack was performed as described in section 3.2.1.1. Figure 4.6 shows a three-dimensional projection of the multidimensional data stack where three of the lowest five dimensions are plotted and each image pixel is represented by one point. In the analysis used here, the dimensions do not have an intuitive meaning like, for instance, in principal component analysis[104]. Hence, they cannot be assigned to specific features of the EEL spectra. In Ref. [104] bulk-heterojunction solar cells made of P3HT and PCBM were investigated and beside two phases of the single materials also a third mixed phase was found. In contrast, only two individual data clouds could be identified here which can be assigned to MoO_3 (red) and CBP (black).
Figure 4.7 (b) shows the resulting classification map of the analysis with pixels of the MoO_3 class depicted in white and pixels corresponding to the material class of CBP in black. As already shown in the previous section for the CBP sample with $33\ \mathrm{vol\%}$ doping concentration, also here a very good correlation between the bright-field image shown in Figure 4.7 (a) and the ESI measurement in Figure 4.7 (b) can be found.

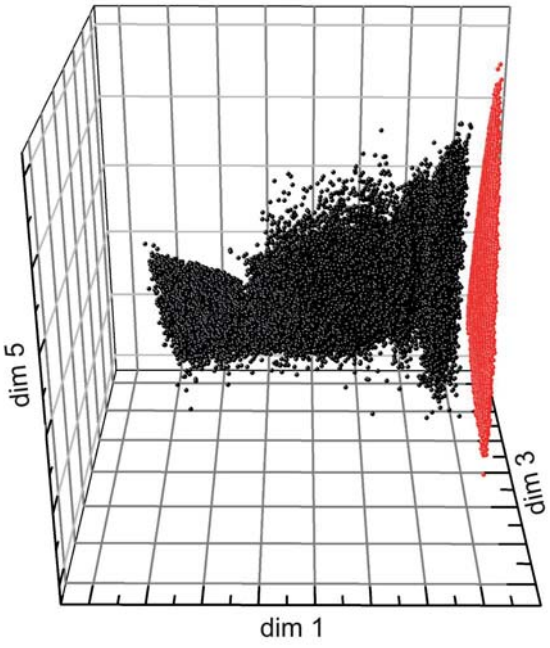

Figure 4.6: Three-dimensional projection of the multi-dimensional data stack obtained from low loss ESI analysis. Three of the lowest five dimensions are depicted and each image pixel is represented by one data point. Two individual data clouds can be identified and assigned to MoO_3 (red) and CBP (black).[130]

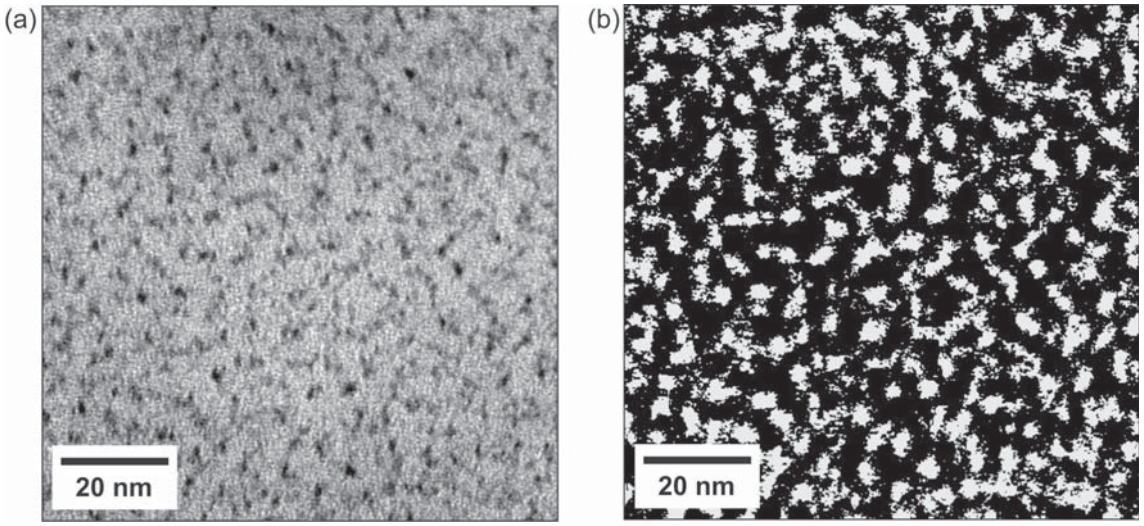

Figure 4.7: (a) Bright-field image of a CBP film with 9 vol% MoO_3.
(b) Corresponding classification map of low loss analysis where the MoO_3 class is depicted in white and the class of CBP in black.[130]

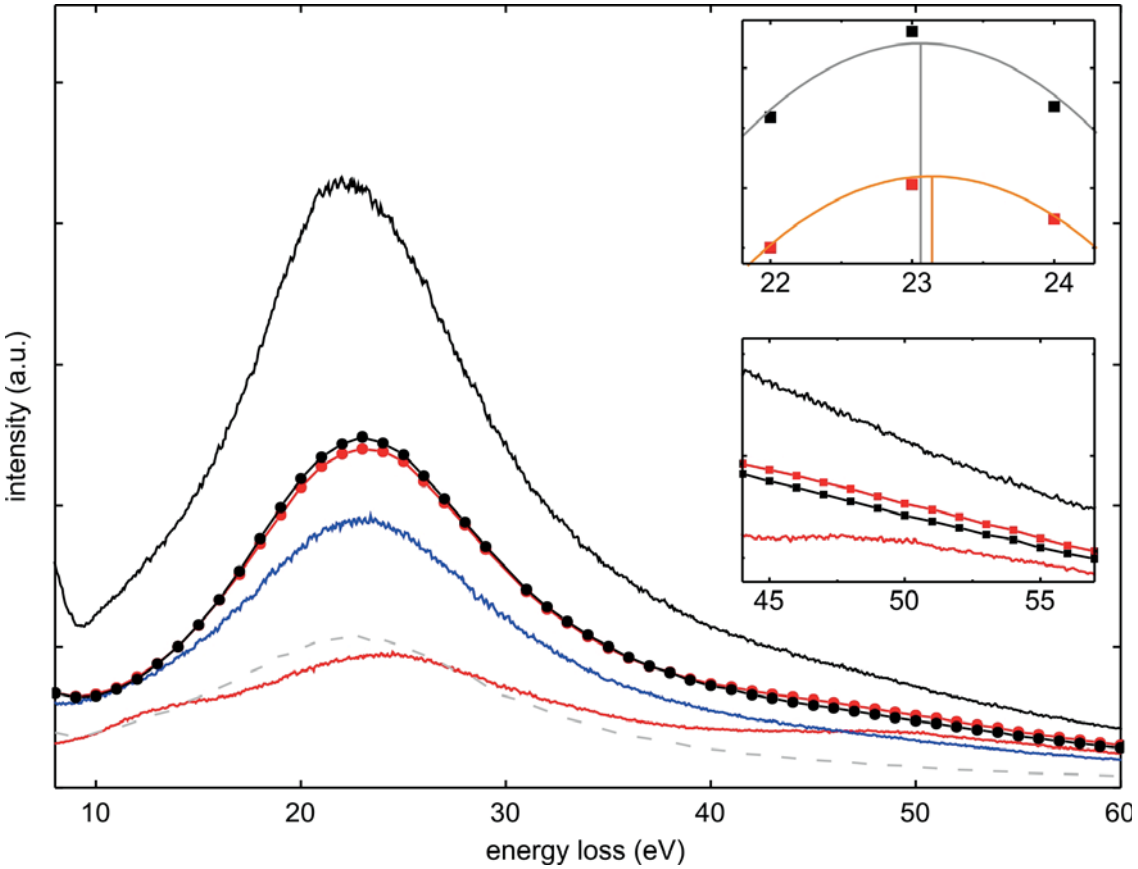

Figure 4.8: Measured EEL spectra in the low loss regime of neat CBP (black solid line) and MoO_3 (red solid line) as well as a doped film with 9 vol% MoO_3 concentration (blue solid line). The films of the pristine materials both contain a Quantifoil background, consisting of amorphous carbon, since the floating process did not work for MoO_3 (see section 3.3.3). The spectrum of the Quantifoil film is depicted as grey dashed line. The averaged spectra obtained by the classification are displayed as dotted lines for CBP (black) and MoO_3 (red). The insets show the main features which led to the material contrast in Figure 4.7, i.e. a small shift in plasmon energy and an ionization edge (Mo-N2,3[111]).[130]

In the following, it will be explained which spectral features led to the observed material contrast. The solid lines of Figure 4.8 show EEL spectra of neat CBP (black solid line) and MoO_3 (red solid line) films in the low loss regime. As described in section 3.3.3, the floating process did not work for MoO_3. Therefore, also the EEL spectrum of CBP was acquired with a Quantifoil background, which consisted of amorphous carbon, to ensure better comparability. In addition, also the spectrum of the neat Quantifoil carbon support film is displayed as grey dashed line. The EEL spectrum of the CBP sample doped with $9\ \mathrm{vol}\%$ MoO_3 concentration is depicted as blue solid line. In dotted lines the averaged spectra obtained by the classification for CBP (black) and MoO_3 (red) are shown. The insets in figure 4.8 show a zoom-in of the features which led to the observed material contrast. The lower inset depicts that in the MoO_3 spectrum an ionization edge (Mo-N2,3[111]) at around $50\ \mathrm{eV}$ appears, which is absent in the CBP spectrum. The other difference is a small shift in Plasmon peak position[111], as can be seen in the upper inset. Gaussian fits of the plasmon peaks revealed peak energies of $23.06\ \mathrm{eV}$ for CBP and $23.14\ \mathrm{eV}$ for MoO_3. The peak position difference is much smaller than one would expect from the experimentally obtained EEL spectra of the neat films, since for the spectra of the pure CBP and MoO_3 films with a carbon background, plasmon peak energies of $22.3\ \mathrm{eV}$ and $23.9\ \mathrm{eV}$ were found. This discrepancy might be due to the fact that a mixed signal originating from both materials is measured, when MoO_3 is embedded in the CBP matrix. Another reason could be that MoO_3 in the bulk phase reveals a different plasmon excitation energy than the nano-sized MoO_3 agglomerations.
In summary, it can be concluded from core loss as well as low loss characterization results that MoO_3 can already be identified in the bright-field image. This proves the suggested hypothesis that MoO_3 agglomerates within the CBP matrix.

4.1.3 Electron Tomography

To gain information about the three-dimensional structure of the MoO_3 agglomerations, as well as their spatial distribution, electron tomography was applied. Since it was demonstrated in the previous sections that bright-field images of CBP:MoO_3 composites show true material contrast and negligible diffraction contrast, the projection requirement was fulfilled and no spectroscopic imaging was necessary. Instead, recording of zero-loss filtered bright-field images was sufficient. As described in section 3.2.1.2, a single axis tilt series was acquired with tilt angles between $-60°$ and $+60°$.

A sample with $30\ \mathrm{nm}$ film thickness and $9\ \mathrm{vol\%}$ doping concentration was fabricated. The electron tomography results of this specimen were already published in Ref. [110]. Additionally, to get more insight into the thickness dependence of the topology, two thicker samples with $100\ \mathrm{nm}$ thickness were prepared with doping concentrations of $0.6\ \mathrm{vol\%}$ and $9\ \mathrm{vol\%}$.

As an example, the entire tilt series of the sample with $30\ \mathrm{nm}$ can be found as movie in the Supporting Information of Ref. [110]. A tilt series can already give an impression about the three-dimensional nature of the sample. Looking at the acquired tilt series, it could already be expected that the MoO_3 agglomerations are not spherically shaped, as speculated in Ref. [131], but have an elongated structure. From the tilt series, which provides projections at different angles, a three-dimensional volume can be obtained, as described in section 3.2.1.2.

Figures 4.9 and 4.10 show slices through the reconstructions for the two $100\ \mathrm{nm}$[1] thick specimens in xy-plane, i.e. in the plane perpendicular to the incident electron beam. Also two slices perpendicular to the xy-plane are shown (xz- and yz-plane). As described in section 3.3.3, gold fiducials were applied to enable alignment of the image series for further processing. These appear in the xz- and yz-planes as large dark spots at the top and at the bottom of the sample. From their positions, the thickness of the film can be determined, since the contrast between vacuum and CBP is negligible.

In both views and for either doping concentration, the three-dimensional reconstructions reveal filamental-shaped dopant structures, preferentially oriented perpendicular to the substrate with longer filaments for $9\ \mathrm{vol\%}$ than for $0.6\ \mathrm{vol\%}$. The slices parallel to the xy-plane reveal small dark spots with a diameter of about $1\ \mathrm{nm}$ for both doping concentrations. The agglomeration density is higher for $9\ \mathrm{vol\%}$ than for the $0.6\ \mathrm{vol\%}$. These results are comparable with the bright-field images presented in section 4.1.1. However, one difference exists. For the $0.6\ \mathrm{vol\%}$ sample the contrast between MoO_3 and CBP is much better in the reconstruction than in the bright-field images. On the contrary, the contrast of the $9\ \mathrm{vol\%}$ sample is similar in the bright-field images and in the reconstruction. This can be explained by the different filament lengths for varied doping concentrations.

[1] As will be pointed out in section 4.1.5, there exists a discrepancy between the evaporated layer thickness and the thickness measured in the TEM. The evaporated film thicknesses are given in the text, if not stated differently.

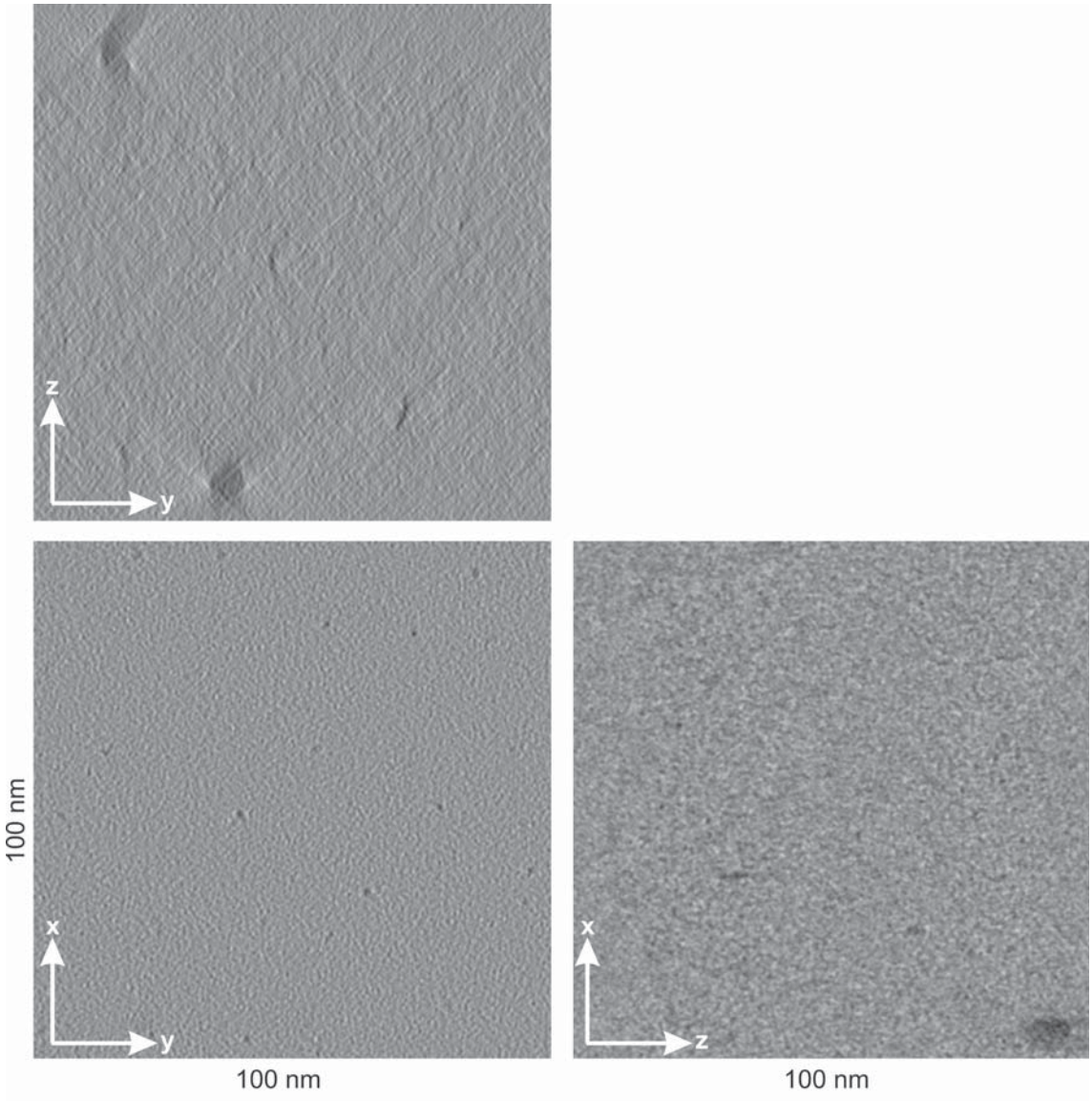

Figure 4.9: Slices through the reconstruction from a tilt series of a $100\ \mathrm{nm}$ thick CBP film with $0.6\ \mathrm{vol}\%$ MoO_3 concentration. Short MoO_3 filaments can be detected in xz- and yz-plane. The xy-plane reveals dark spots with a diameter of about $1\ \mathrm{nm}$, similar to the bright-field image shown in Figure 4.1 (a). Some of the applied fiducials moved during the tilt series acquisition. Therefore, these were excluded for aligning the images for the reconstruction. As can be seen in the yz-slice, such a fiducial appears distorted in the reconstruction.

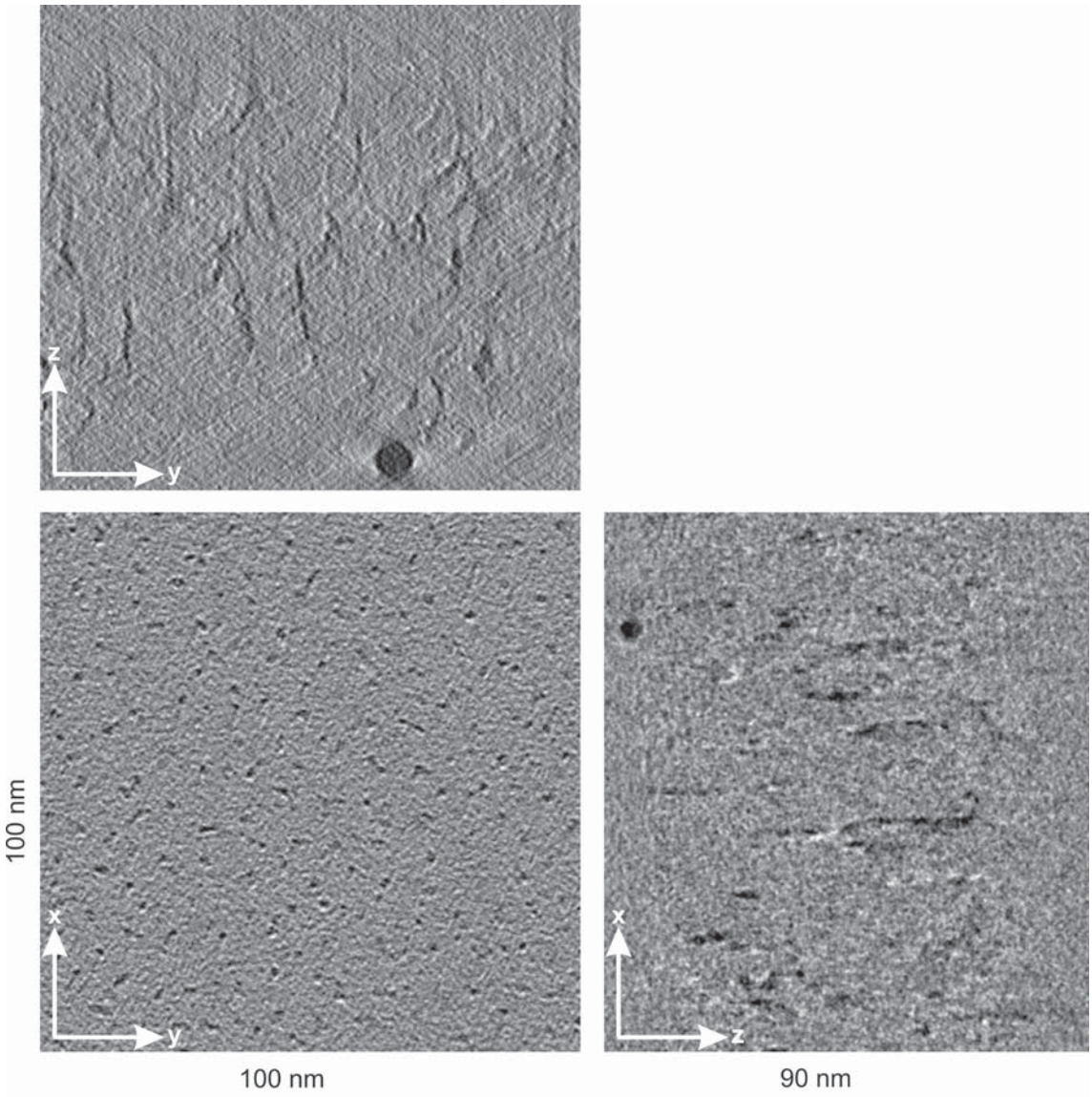

Figure 4.10: Slices through the reconstruction from a tilt series of a $100\ \mathrm{nm}$ thick CBP film with $9\ \mathrm{vol}\%$ MoO_3 concentration. Compared to the filaments of Figure 4.9, longer filaments can be identified with a higher density in the xz- and yz-plane. The dark spots in the xy-plane reveal a diameter of about $1\ \mathrm{nm}$, similar to the bright-field image shown in Figure 4.1 (c).

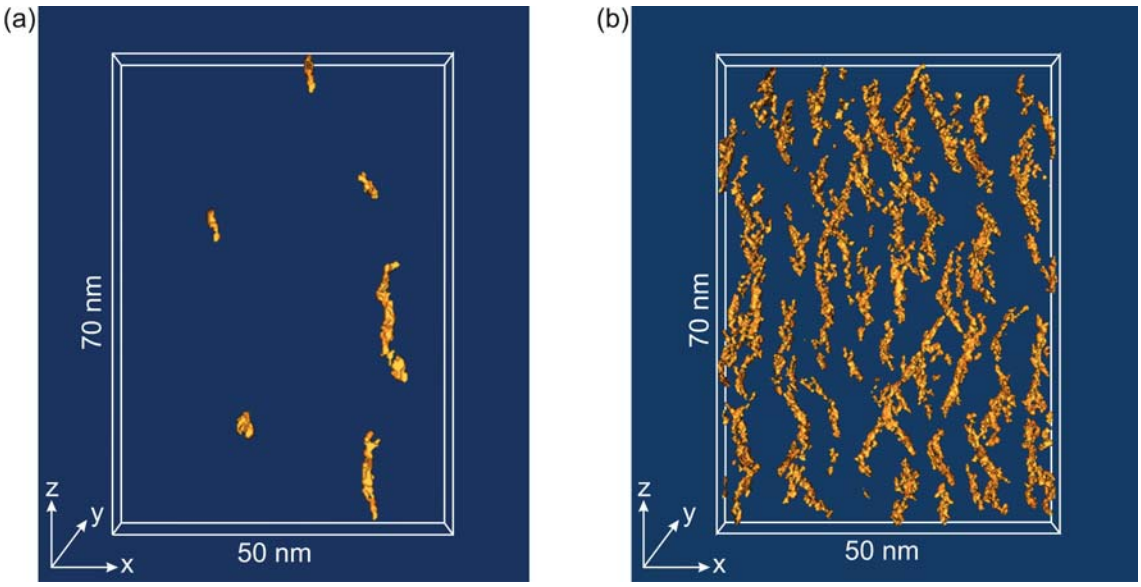

Figure 4.11: Isosurface representation of reconstructions shown in Figures 4.9 and 4.10 of CBP films doped with (a) 0.6 vol% and (b) 9 vol% MoO_3 doping concentration. The length in y-direction is 5 nm.

The bright-field image shows a projection of the sample, where short filaments embedded in a thick CBP matrix lead to worse contrast in comparison to long filaments embedded in a CBP matrix of the same thickness. Since the three-dimensional reconstruction does not show a projection but slices through the volume, the contrast is not influenced by the filament length.

In order to obtain a better visualization of the reconstruction, a certain threshold can be chosen and all pixels with a grayscale value higher than this threshold can be depicted with the same color. This is called an isosurface representation. Of course, such a representation is highly subjective, since the chosen threshold value strongly influences the resulting representation. Therefore, it had to be carefully chosen after detailed consideration of the reconstruction results shown in Figures 4.9 and 4.10. Isosurface representations of both samples are shown in Figures 4.11 (a) and (b). The z-direction with a length 70 nm represents the film thickness. A thickness of only 5 nm in y-direction was chosen, since for a larger thickness no single filaments would be observable for the higher doped sample. For the sample with 9 vol% MoO_3 concentration this gives a good impression of the sample topology, whereas for 0.6 vol% doping concentration only very few filaments

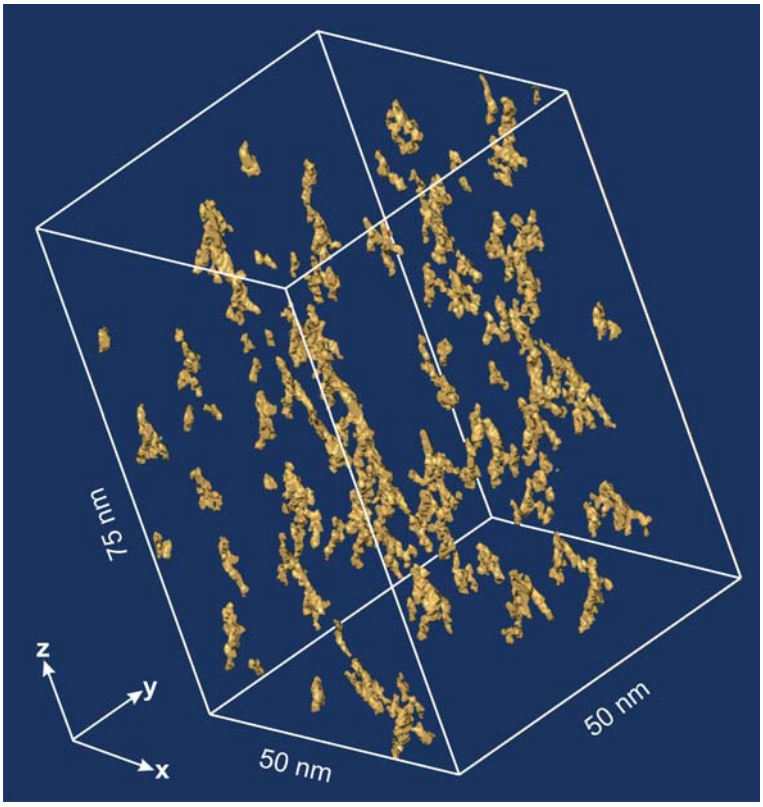

Figure 4.12: Isosurface representation of a CBP film with 0.6 vol% MoO_3 concentration. Compared to Figure 4.11 (a), a larger section of the reconstruction is shown here.

are included in the chosen section. To obtain a better overview of the filament distribution of the 0.6 vol% sample, a so called isometric view is additionally depicted in Figure 4.12. Since in the reconstruction the observed nanofilaments do not exactly proceed perpendicular to the substrate, adjacent slices have to be considered for measuring the filament length from the reconstruction. The filament length was estimated with the line measurement tool of the software Fiji. For both doping concentrations, 20 filament lengths were measured. For 0.6 vol% MoO_3 concentration, lengths between 4 nm and 24 nm were found, whereas the average length amounted to about 12 ± 5 nm[2]. The film with 9 vol% revealed an even more complicated structure. Beside relatively short filaments with a length of around 15 nm, also filaments almost going through the whole sample thickness

[2]Standard deviation

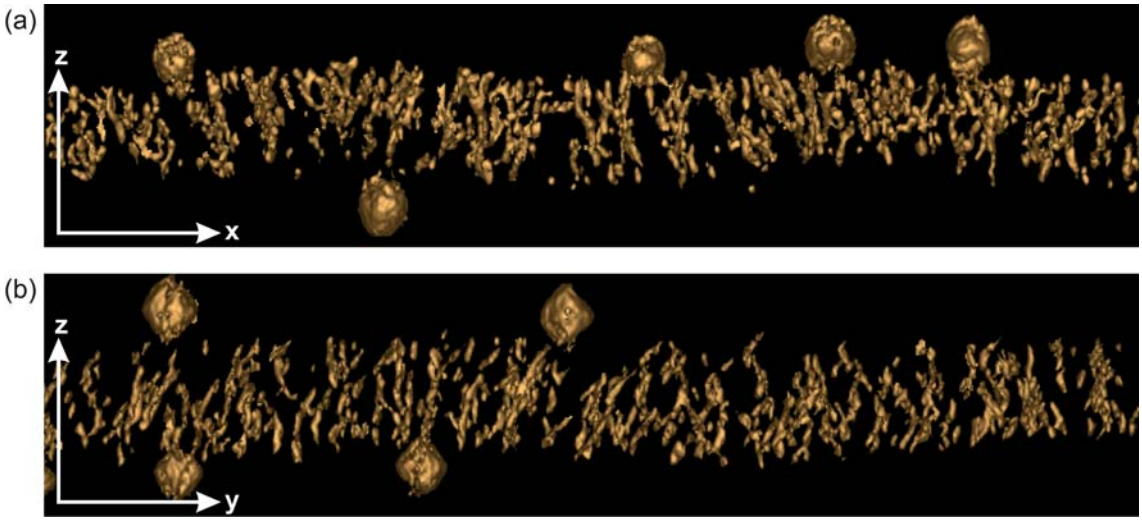

Figure 4.13: Isosurface representation of slices through the reconstruction of a CBP:MoO_3 sample with $30\ \mathrm{nm}$ thickness and $9\ \mathrm{vol\%}$ doping concentration. The xz- and yz-directions are shown to illustrate the missing wedge effect in electron tomography reconstructions from single-axis scans.

occur with a length of up to $55\ \mathrm{nm}$. What makes the topology description for this doping concentration even more complicated is the fact that filaments sometimes also branch out. The average filament length was determined to amount to $35 \pm 13\ \mathrm{nm}$. Of course, this method comprises quite high uncertainties, but it can still be concluded that the filaments in the $9\ \mathrm{vol\%}$ film are longer than for $0.6\ \mathrm{vol\%}$ doping concentration.

As already mentioned in section 3.2.1.2, the acquired single-axis scan contains artifacts. The so called missing-wedge effect is illustrated in Figure 4.13, where, as an example, the reconstruction of the $30\ \mathrm{nm}$ sample with $9\ \mathrm{vol\%}$ MoO_3 concentration is shown from two sides perpendicular to each other. The gold fiducials at the top and at the bottom of the film have a spherical shape. If one looks from the side in which the sample is tilted (Figure 4.13 (a)) the fiducials indeed look spherically shaped, but from the view $90°$ apart the gold fiducials seem to be cut at the edges. This visualizes that not all sample information was collected during data recording. Additionally, acquisition of thickness maps revealed that the thickness decreased during the tilt series measurements. For the film with $9\ \mathrm{vol\%}$ evaporated onto a substrate at $120\ \mathrm{K}$ (see section 4.1.4) the value for the relative thickness according to equation (3.2.1) was found to amount to 0.41 before and

0.32 after data acquisition. This decrease in thickness is probably due to mass loss caused by electron beam damage and also influences the reconstruction.
Therefore, it can be concluded from the obtained reconstruction that MoO_3 forms filaments preferentially oriented perpendicular to the substrate, but not the detailed structure of these filaments. It must also be mentioned that a change of the threshold value (see section 3.2.1.2) can change the presentation of the reconstruction significantly.
To receive more specific information about the dopant structure, a double-axis tilt series could be acquired to reduce the missing wedge effect to a missing pyramid effect[134]. Furthermore, to decrease beam damage, the discrete algebraic reconstruction technique (DART)[135] could be applied for reconstruction, which requires less images than the reconstruction algorithms applied here.
To investigate whether the nanofilament growth is substrate dependent, a $30\ \mathrm{nm}$ multilayer structure was fabricated, consisting of $10\ \mathrm{nm}$ CBP doped with $9\ \mathrm{vol}\%$ MoO_3, followed by a $10\ \mathrm{nm}$ neat CBP layer and again finished with $10\ \mathrm{nm}$ of doped CBP. The reconstruction, which is shown in Figure 4.14, reveals that nanofilament growth occurs in both doped layers. The reconstruction gives the impression that the doped layer at the top is thicker than the doped layer underneath the neat CBP layer. This effect is caused by increased surface roughness with increasing film thickness, leading to a wider spread in the spatial distribution of the doped layers from the side perspective. This result also indicates that nanofilament growth is not limited to growth on PEDOT:PSS, since it also occurs in the same way when CBP serves as substrate.

Morphology Evolution in Dependence of Dopant Concentration inferred from XPS Measurements

Since electron tomography is an extremely time-consuming method, it is not possible to acquire tomograms for various doping concentrations to find out how the topology relates to the doping concentration. In the following, it will be shown that XPS results, which give information about the electronic structure, can be correlated with the observed dopant topology and therefore also used to obtain information about the topology evolution for increasing doping concentrations. All measurements presented in this section were performed and analyzed by M. Kühn[49].
Mo3d spectra of composites with different doping concentrations were acquired via XPS.

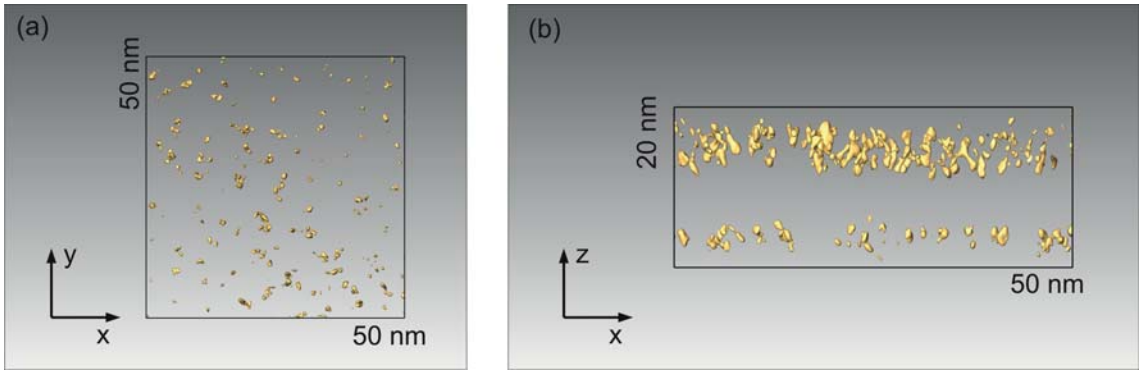

Figure 4.14: Isosurface representation of the reconstruction of a $30\ \mathrm{nm}$ multilayer structure, consisting of $10\ \mathrm{nm}$ CBP doped with $9\ \mathrm{vol\%}$ MoO_3, followed by a $10\ \mathrm{nm}$ thick layer of pure CBP and finished with another $10\ \mathrm{nm}$ thick layer of doped CBP. The upper doped part seems to be thicker because of an increased surface roughness with increasing film thickness, which leads to a wider spread in the spatial distribution of the doped layers from the side perspective. (a) Top-view of xy-plane. (b) Side-view of xz-plane.[130]

In Figure 4.15, the Mo3d spectrum of a composite with $45\ \mathrm{mol\%}$[3] is depicted exemplary. The main feature of this spectrum is a doublet which is expected for pure MoO_3 because of spin orbit coupling. Besides, a shoulder can be identified at the low energetic side of each of the two emission lines of the doublet. This shoulder is due to the reduced component of MoO_3 since after the charge transfer from CBP to MoO_3 the electrons are weaker bound to molybdenum oxide than in the uncharged species[49]. Based on DFT calculations compared with PES experiments[136], d-orbital aromaticity can be assumed. This means that the transferred electron is evenly distributed over all three molybdenum atoms of the Mo_3O_9 cluster. Since the oxidation state of uncharged molybdenum amounts to +6 the charge transfer leads to an oxidation state of +6-$\frac{1}{3}$ = +$\frac{17}{3}$ for each molybdenum atom[136]. This fact will become important in section 4.2.2.2 where the number of charged Mo_3O_9 clusters will be determined and is only explained in this context to be able to use the right terminology. In the following, uncharged molybdenum oxide will be depicted

[3]For discussing electronic properties where normally charge carriers are considered, it makes more sense to specify the doping concentration in mol%, whereas for topography investigations the volume fraction given in vol% seems to be more meaningful. Therefore, the doping concentrations for TEM results are normally given in vol%, whereas, when referring to electrical or electronic measurements, mol% is used. Where necessary, both quantities are indicated according to equations (3.3.1) and (3.3.2) in section 3.3.1

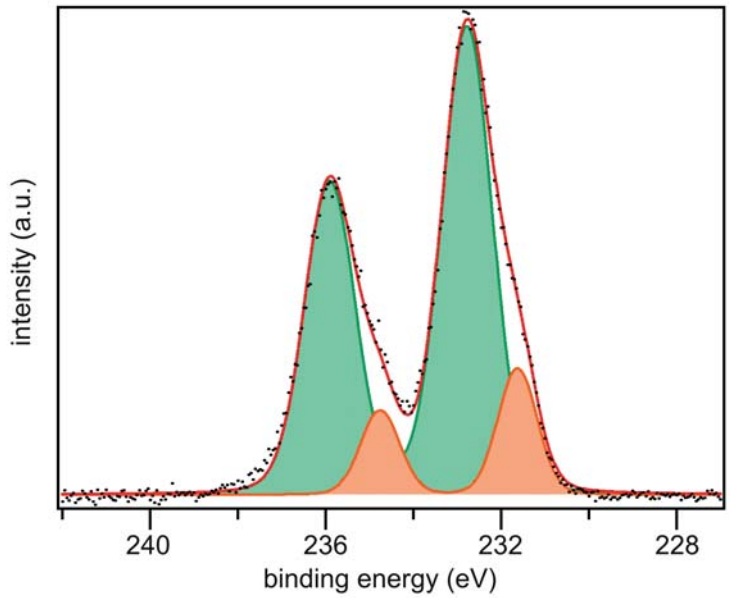

Figure 4.15: Mo3d emission line of a CBP film doped with $45.3\ \mathrm{mol}\%$ Mo_3O_9. Beside the doublet of Mo^{6+}, a shoulder at lower binding energies can be identified which was assigned to the reduced component of MoO_3. Both doublets are fitted with voigt-functions, to determine their respective intensities. The doublet which belongs to Mo^{red} is shown in orange and the doublet which belongs to Mo^{6+} is depicted in green. The measurement is displayed in black dots and the sum curve over both doublets is shown in red. The displayed data was measured and analyzed by M. Kühn and the image is taken from Ref. [49].

as Mo^{6+}, whereas the charged molybdenum species with the oxidation state $+\frac{17}{3}$ will be labeled as Mo^{red}.

The ratio of Mo^{6+} and Mo^{red} was determined by fitting voigt functions (see section 3.2.2.1) to the spectra of the Mo3d emission lines for different doping concentrations. Each emission spectrum was described by two doublets which were shifted against each other, one for Mo^{6+} and one for Mo^{red}. An example for such a fit is depicted in Figure 4.15 (red graph). A factor γ was defined as

$$\gamma = \frac{A(\mathrm{Mo^{red}})}{A(\mathrm{Mo^{red}}) + A(\mathrm{Mo^{6+}})} \tag{4.1.1}$$

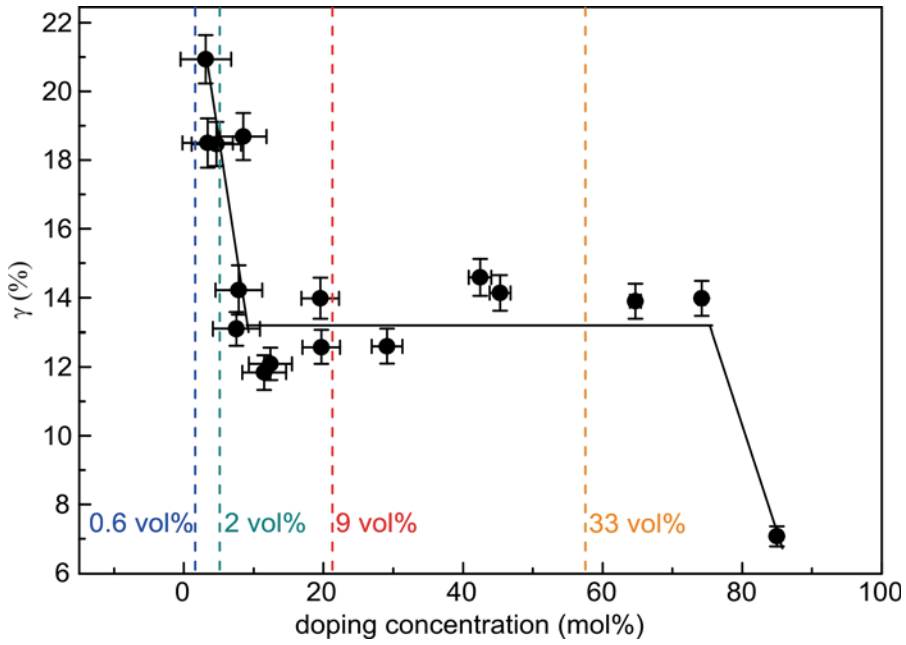

Figure 4.16: The surface-to-volume ratio γ, which was calculated using equation (4.1.1), is displayed as a function of the doping concentration and three regimes can be identified. Up to about $9\ \mathrm{mol\%}$ MoO_3 concentration, γ decreases continuously. This first regime is followed by a constant regime, whereas for the highest doping concentration γ drops. The displayed data was measured and analyzed by M. Kühn.

with $A(\mathrm{Mo^{6+}})$ and $A(\mathrm{Mo^{red}})$ being the integrated intensities for the doublet which belongs to $\mathrm{Mo^{6+}}$ and $\mathrm{Mo^{red}}$, respectively. The intensity of both doublets can be seen as a measure for the number of the respective species.

In Figure 4.16, γ is shown in dependence of the doping concentration. Three regimes can be identified. In the first regime up to about $9\ \mathrm{mol\%}$ Mo_3O_9 concentration, γ decreases continuously, followed by a constant regime up to about $77\ \mathrm{mol\%}$. For even higher doping concentrations, only one measurement was acquired where γ decreased dramatically. An angle-dependent XPS interface experiment showed that $\mathrm{Mo^{red}}$ is located at the interface. Therefore, γ can be interpreted as a measure for the surface-to-volume ratio since it is defined as the ratio of $\mathrm{Mo^{red}}$, which is a measure for the surface, and the total molybdenum content ($\mathrm{Mo^{6+}}$+ $\mathrm{Mo^{red}}$) which is a measure for the volume.

In section 4.1.1 it was shown that for CBP samples doped with $0.6\ \mathrm{vol\%}$, $2\ \mathrm{vol\%}$, $9\ \mathrm{vol\%}$ and $33\ \mathrm{vol\%}$ MoO_3 the agglomeration diameter is constant. Assuming that there is a con-

stant filament diameter for all doping concentrations and assuming that the surface charge density is independent of the doping concentration, the result of Figure 4.16 could be interpreted as follows. For the regime up to $9\ \mathrm{mol\%}$ where the surface-to-volume ratio decreases there must be shorter filaments present in the film which become longer with increasing doping concentration. Then, for lower doping concentrations the surface-to-volume ratio is higher since there is additional surface from the top and bottom parts of the filaments. In the second regime from $9\ \mathrm{mol\%}$ to $77\ \mathrm{mol\%}$ the surface-to volume ratio stays constant. This means for the assumption of a constant filament diameter that only the number of filaments increases with increasing doping concentrations but the filament length stays the same. This interpretation is in accordance with the electron tomography results discussed before where the filament length of the $0.6\ \mathrm{vol\%}$ sample were significantly shorter than for $9\ \mathrm{vol\%}$. For the measurement at $85\ \mathrm{mol\%}$ which has a much lower surface-to-volume ratio, the interpretation assuming a constant filament diameter would be crosslinking of the MoO_3 filaments, so that MoO_3 forms a network structure, which decreases the surface-to-volume ratio. Of course the model presented above is somehow simplified since the filament structure does not just consist of columns oriented perpendicular to the substrate surface, but as far as it can be seen from the TEM tomography, there are also side branches present.

4.1.4 Influence of the Substrate Temperature

To gain information about the growth process of the observed nanofilaments, a CBP sample doped with $9\ \mathrm{vol\%}$ MoO_3 was evaporated in the FTIR tool (see section 3.1) onto a substrate cooled down to approximately $120\ \mathrm{K}$ during the evaporation process at a pressure below $2 \cdot 10^{-9}\ \mathrm{mbar}$ during evaporation. As already mentioned in section 3.3.1, for this sample an evaporation rate of $30\ \mathrm{\AA/min}$ had to be chosen, instead of $50\ \mathrm{\AA/min}$, which was used for almost all samples prepared at room temperature in organic chamber 1 and 2.

Therefore, the question arises if different growth rates used for the cooled and the uncooled sample have an influence on the topology. Glaser et al. investigated whether the growth rate has an influence on the electronic properties, which could be expected for a

diffusion driven and therefore time-dependent process[112]. CBP films doped with MoO_3 were prepared with CBP growth rates of $20\ \text{Å}/\text{min}$ and $59\ \text{Å}/\text{min}$, respectively. No significant changes were detected in the fingerprint region (frequency range from $1100\ \text{cm}^{-1}$ to $1700\ \text{cm}^{-1}$) and at higher frequencies, where electronic excitations are found in the FTIR spectra. Since the strength of the electronic excitations will be shown in section 4.2.2.1 to depend on the interface area of MoO_3 filaments and CBP, it can be expected that a change of growth rate in this range ($30\ \text{Å}/\text{min}$ and $50\ \text{Å}/\text{min}$) does not have a major impact on the topology.

The bright-field image of the cooled sample is shown in Figure 4.17 (b). For better comparison to the sample prepared at room temperature, Figure 4.1 (c) is again depicted in 4.17 (a). Comparing these two images reveals, that only few MoO_3 features can be detected in the cooled sample, compared to the one evaporated at room temperature. This leads to the conclusion that the MoO_3 is dispersed more homogeneously for the sample grown at the lower temperature than for the room temperature sample. The result shows that it is possible to control the topology and the amount of agglomeration just by changing the substrate temperature during the evaporation process.

Figure 4.18 shows EEL spectra of both doped films as well as the spectrum of a neat MoO_3 film. All spectra were background-corrected and normalized with respect to the peak at $532\ \text{eV}$ like in Figure 4.4. The fact that the same energy loss features can be found in the doped films and in the neat MoO_3 film indicates that the electronic structure of MoO_3 in the bulk phase and MoO_3 incorporated as dopant is comparable. Because the spectra of both doped films show similar peak intensities at the oxygen K-edge, it can be deduced that similar amounts of MoO_3 are present in both films.

Since the features appearing in the image of the cooled sample look similar to the features of the CBP sample doped with $0.6\ \text{vol}\%$ (see Figure 4.1 (d)) it could be supposed that in the case of the cooled sample, also filaments with a comparable diameter have formed, but with a shorter length compared to the filaments of the room temperature sample. However, unless no electron tomography is acquired, this is just a speculation and filaments which are smaller in diameter or even completely dispersed MoO_3 dopants are also conceivable.

To address this issue, another sample with $9\ \text{vol}\%$ MoO_3 concentration was fabricated in the FTIR tool at a substrate temperature of $120\ \text{K}$ and a tilt series was acquired. Slices

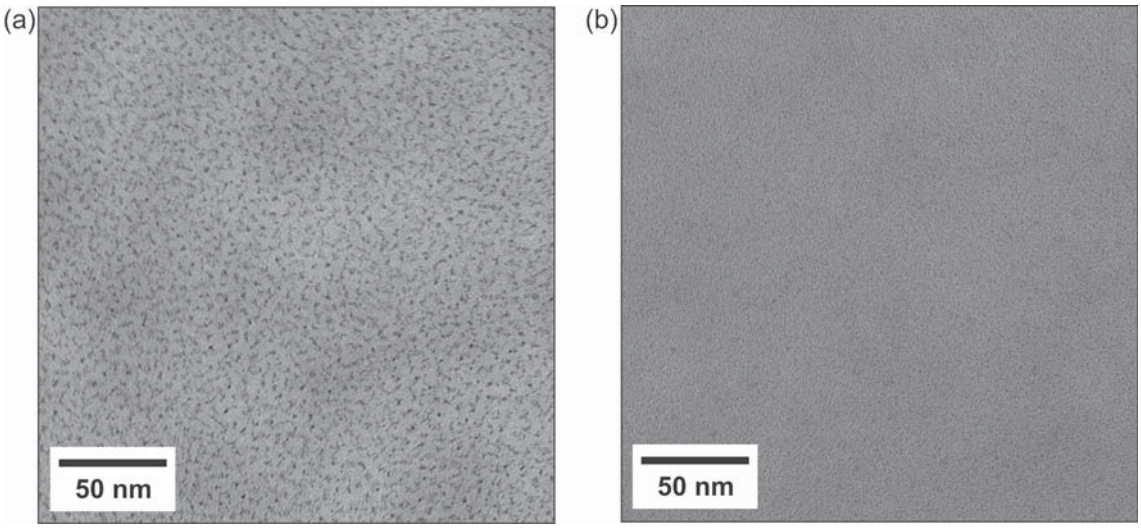

Figure 4.17: Bright-field images of 30 nm thick samples with 9 vol% doping concentration, evaporated onto (a) a substrate kept at room temperature and (b) a substrate which was cooled down to about 120 K during the evaporation process. No clear features can be identified in the cooled sample, compared to the room temperature film.[130]

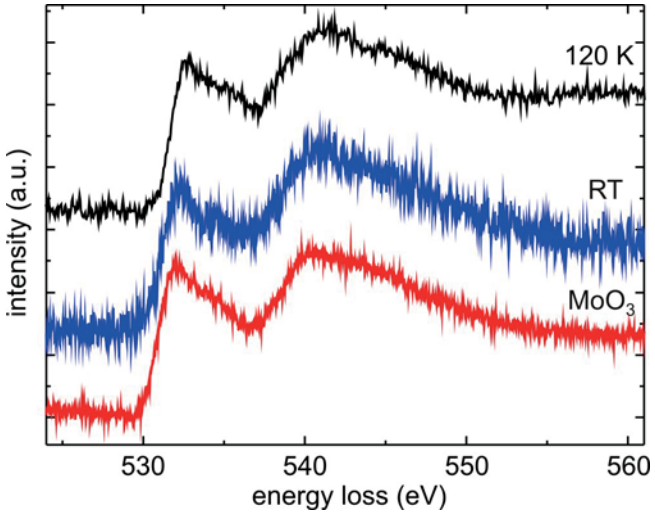

Figure 4.18: Background-corrected EEL spectra of a pure MoO_3 film with 70 nm film thickness (red), as well as doped films (9 vol%, 30 nm), evaporated onto substrates kept at room temperature (blue) and cooled down to about 120 K during the deposition process (black).[130]

through the obtained reconstruction are shown in Figure 4.19. The slice in the xy-plane looks similar to the same view of the room temperature sample shown in Figure 4.10. The slices in the xz- and yz-plane also reveal filaments preferentially oriented perpendicular to the substrate, however with a shorter length than the filaments in the room temperature specimen. A very rough estimation using the line measurement tool of Fiji, as described in section 4.1.3, revealed filament lengths ranging from $1.3\ \mathrm{nm}$ to $16.2\ \mathrm{nm}$ with an average length of $4.8 \pm 3.5\ \mathrm{nm}$. For comparison, the sample with the same doping concentration but evaporated onto the substrate at room temperature had an average filament length of $35 \pm 13\ \mathrm{nm}$. To allow a better comparison, the isosurface representations of the reconstruction for the samples prepared at room temperature and at $120\ \mathrm{K}$ are depicted in Figure 4.20 (a) and (b). For the cooled sample, longer filaments can be identified in the top part compared to the bottom part[4]. This directs towards a thickness-dependent temperature gradient, so that the top part employed higher filament lengths due to a higher temperature.

In some parts of the tilt series, and therefore also in the reconstruction, large features could be observed as shown in Figure 4.21. These features are probably due to the fact that the sample was not completely warmed up to room temperature before it was brought from UHV to air so that water could condense and infiltrate into the film. However, this happened after film growth and only at some areas of the sample. However, no difference in CBP:MoO_3 topology could be identified between the positions where the large features occur and where they do not appear. Therefore, the water infiltration should not have affected the film topology.

Influence of Substrate Temperature on the Topology inferred from FTIR Measurements

Also from FTIR spectroscopy information about the influence of the substrate temperature on the topology of the doped films can be inferred. In the experimental setup used here, the advantage of FTIR over TEM is that in FTIR it is also possible to gain informa-

[4] Since clear orientation information was lost during preparation, measurement and reconstruction of the samples, the assignment which side of the reconstruction was the top part was made with the assumption that the top part exhibits a higher roughness than the bottom part.

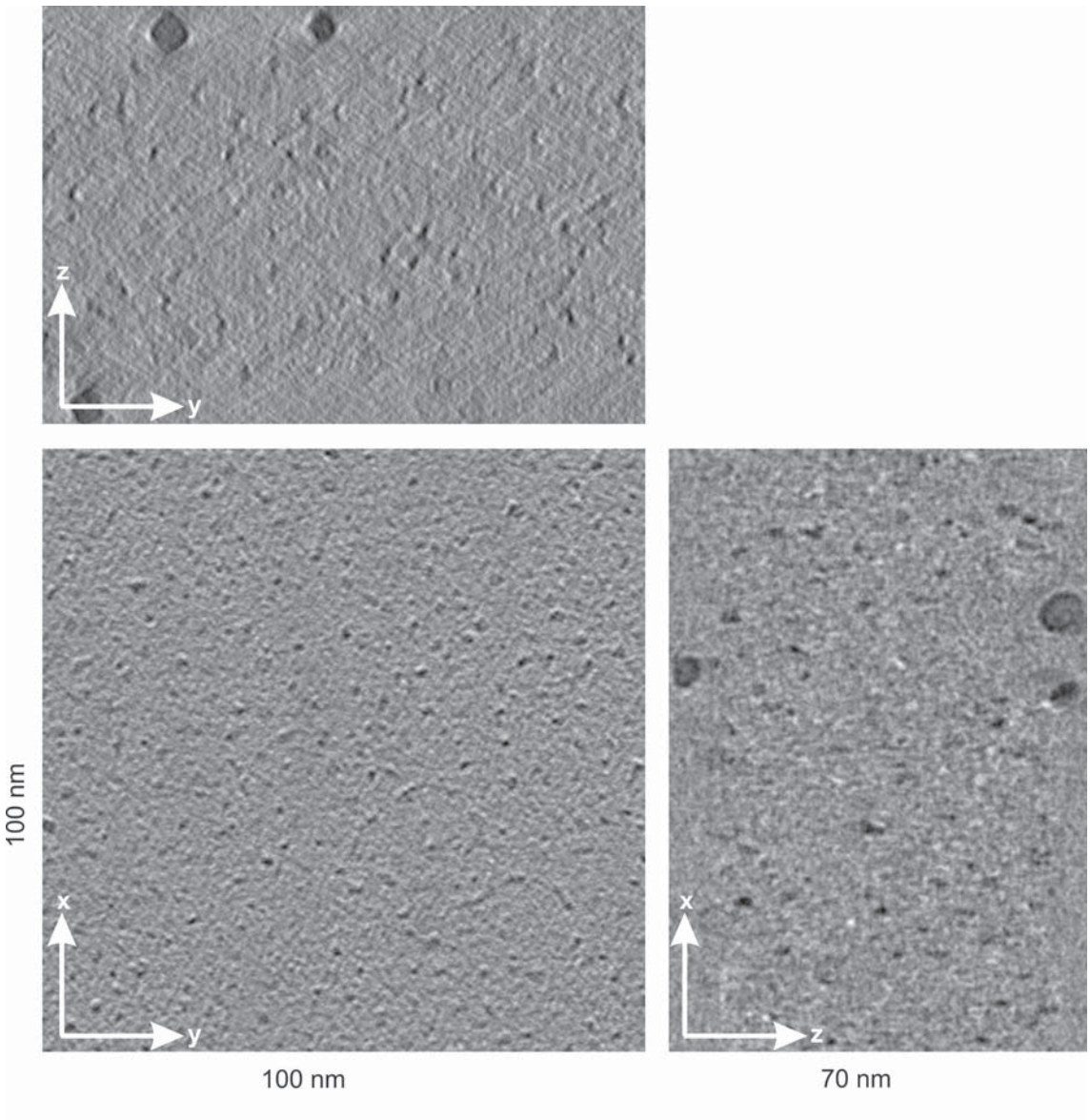

Figure 4.19: Slices through reconstruction from a tilt series of a $100\ \mathrm{nm}$ thick CBP film with $9\ \mathrm{vol}\%$ MoO_3 concentration deposited onto a substrate cooled down to about $120\ \mathrm{K}$ during evaporation. Compared to the reconstruction of the sample with the same doping concentration where the film was deposited at room temperature (see Figure 4.10) much shorter MoO_3 filaments can be seen in the xz- and yz-plane. However, the slice in the xy-plane also reveals dark spots with a diameter of about $1\ \mathrm{nm}$ similar to the reconstruction of the room temperature sample.

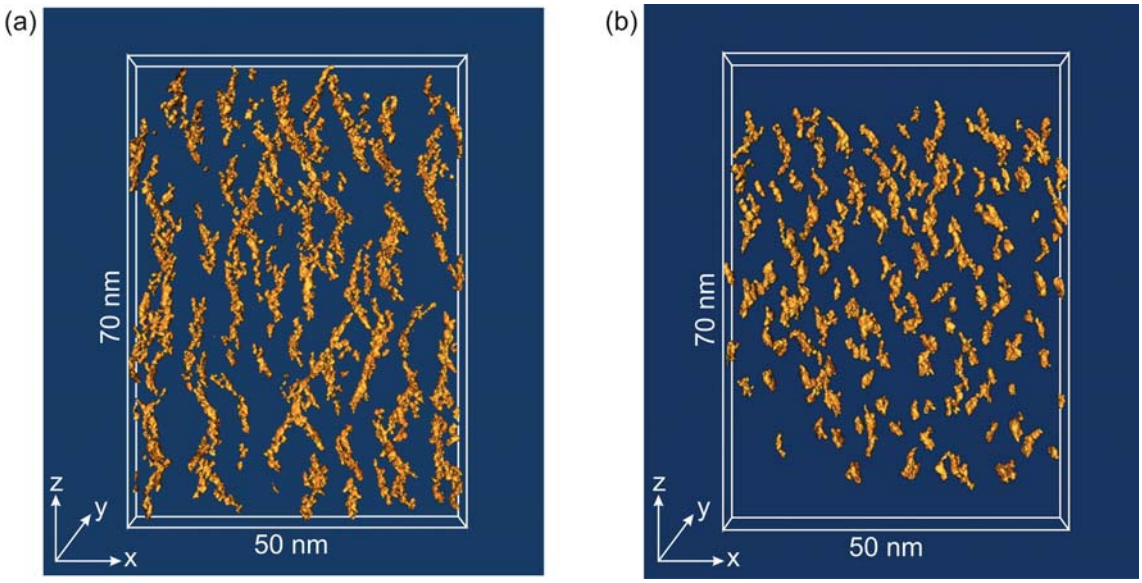

Figure 4.20: Isosurface representation of reconstructions shown in Figures 4.10 and 4.19 of CBP films doped with $9\ \mathrm{vol}\%$ MoO_3 doping concentration and (a) the substrate kept at room temperature during the evaporation process and (b) cooled down to about $120\ \mathrm{K}$. The length in y-direction is $5\ \mathrm{nm}$.

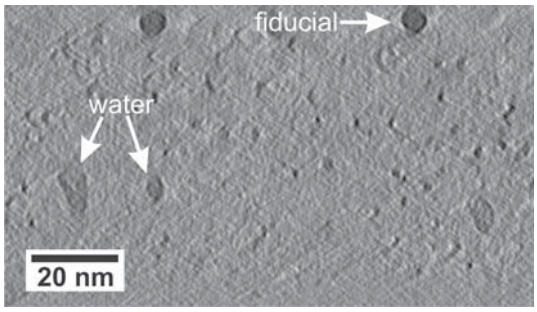

Figure 4.21: In some parts of the reconstruction large features can be seen, which are most likely due to water infiltration.

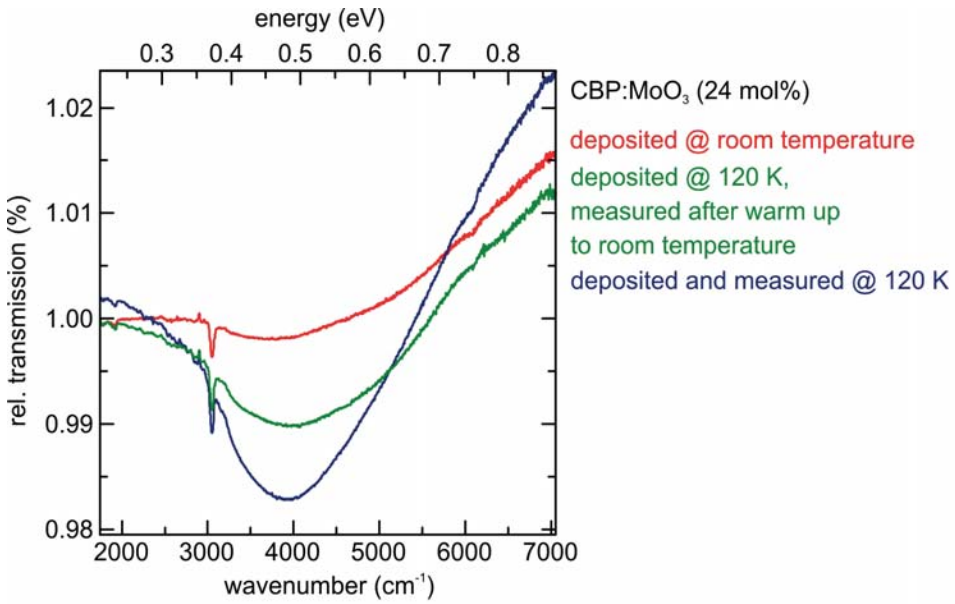

Figure 4.22: FTIR spectra of the electronic absorption of CBP samples with $24\ \mathrm{mol\%}$ MoO_3 concentration (a) evaporated onto a substrate at room temperature and measured at room temperature (red), evaporated onto a substrate cooled down to about $120\ \mathrm{K}$ and measured while it was still cold (blue) and measured after warm up to room temperature (green). The displayed data was measured and analyzed by T. Glaser.

tion about samples prepared onto a cooled substrate while they are still cooled down and not only when they are already warmed up to room temperature.

Therefore, samples were prepared with the substrates cooled down to about $120\ \mathrm{K}$ during film deposition. Then, FTIR spectra were taken while the sample was still cooled down, after warming up to room temperature and after it was again cooled down to about $120\ \mathrm{K}$. FTIR spectra for the wavenumber range from about $2000\ \mathrm{cm}^{-1}$ to $7000\ \mathrm{cm}^{-1}$ are displayed in Figure 4.22. There, a comparison of a thin film with $24\ \mathrm{mol\%}$ (i.e. $10.5\ \mathrm{vol\%}$) prepared and measured at the above mentioned temperatures is shown. Additionally, a sample with the same doping concentration, that was evaporated onto a substrate at room temperature and measured at room temperature, is depicted for comparison. As explained in more detail in section 4.2.2.1 the intensity of this broad electronic absorption can be seen as a measure of the MoO_3/CBP interface area. Figure 4.22 shows that the intensity of the broad electronic excitation for the sample evaporated onto a substrate at room

temperature and measured at room temperature (red spectrum) is lower than for the sample evaporated onto the cooled substrate that was measured at room temperature (green spectrum). This indicates that the interface area is higher for the cooled sample than for the room temperature one and is in accordance with the tomography results presented in Figure 4.20 where significantly shorter filaments could be found for the cooled film. Fitting the intensity of these measurements (see section 4.2.2.1) revealed that the cooled sample, which was warmed up to room temperature, has a 1.7 fold intensity compared to the sample evaporated and measured at room temperature[112], i.e. the cooled sample has 1.7 fold more interface area than the room temperature sample.
Comparing the electronic absorption of the sample which was cooled during deposition and also measured while it was still cooled down (blue spectrum) with the measurement after warming it up to room temperature (green spectrum) reveals a higher intensity for the measurement taken at $120\ \mathrm{K}$. This finding indicates that, after warming up the cold deposited sample to room temperature, a post-clustering process takes place where the high interface area is reduced, which indicates that the agglomerates increase in size. However, the interface area is still bigger than for deposition at room temperature. Glaser et al. found that no significant changes could be observed when the sample was cooled down again after warming up. This suggests that the system reaches kind of an equilibrium state after warm-up, which does not change if the sample is cooled down again. Since the pre- and post-clustering processes take place when the temperature is changed, probably diffusion-driven processes are involved.

4.1.5 Discussion of Filament Diameter

In section 4.1.1 the mean diameter of the agglomerates, as well as the mean distance between the filaments, was derived from the bright-field images. Assuming straight filaments with a radius r and a mean distance d, the volume ratio of MoO_3 V_r of a total volume V_total can be calculated for a mean height of the filaments h and a sample thickness H with the following relation:

$$V_\mathrm{r} = \frac{V_{\mathrm{MoO_3}}}{V_\mathrm{total}} = \frac{\pi r^2 h}{d^2 H}. \tag{4.1.2}$$

The ratio F of the filament diameter and the sample thickness can then be calculated as follows:

$$\frac{h}{H} = \frac{V_r d^2}{\pi r^2} =: F. \tag{4.1.3}$$

With the values, which were determined in section 4.1.1 for filament diameters and distances, the filament height is calculated to amount to 4.1 , 5.7 and 9.1 times the height of the sample thickness, for 2 vol%, 9 vol% and 33 vol%, respectively. Since the length of the filaments cannot be larger than the sample thickness, the assumptions made above must be wrong. Possible explanations for the observed discrepancies might be that the dark spots which can be seen in the bright-field images do not represent all of the MoO_3, because, for example, the contrast between the carbon and the nitrogen atoms of CBP and the oxygen atoms of MoO_3 is quite weak. The discrepancy becomes even worse since it was shown that most of the filaments do not extend through the whole film thickness. On the other hand the filament diameter determined from the bright-field results might even be smaller, since because of bended filaments the projection might show bigger filament diameters.

To gain more information about the real filament diameter TEM spectroscopy could be applied, as described in section 4.1.2.1 and 4.1.2.2. Since the result for the core loss regime is quite noisy, only the low loss measurements could be used for answering this question. Indeed, a PSD of the image in Figure 4.6 (b) revealed a slightly higher filament diameter of about 1.15 nm. However also this result might be arguable for the same reasons as the bright-field measurements, since parts of bended filaments might be assigned to the MoO_3 class although there is only a fraction of MoO_3 present in the projection. Therefore, also this analysis cannot explain the observed discrepancies of applied doping concentration and the doping amount determined via TEM measurements. The most likely explanation is that not all of the Mo_3O_9 clusters form nanofilaments but that a quite high fraction is also dispersed homogeneously in the organic matrix or forms filaments which are too short or too small in diameter to give contrast in the bright-field images.

This assumption can be supported by determining the amount of dopants from the isosurface representation of the electron tomography results. The doping concentration can be calculated from the number of pixels assigned to MoO_3. For the samples with 0.6 vol% and 9 vol% (see Figures 4.11 (a) and 4.11 (b)), fabricated onto a substrate at room temperature, the doping concentration determined via electron tomography is

$0.27\ \%$ and $1.48\ \%$, whereas for the sample with $9\ \mathrm{vol}\%$, evaporated onto the cold substrate, it amounts to $0.73\ \%$. However, one has to consider that this is only a very rough estimate, since the tomography contains a couple of artifacts and the isosurface representation is quite subjective. Therefore, this analysis might only give an additional hint that not all of the Mo_3O_9 dopants are incorporated in the observed filament structure.

4.1.6 Description of MoO_3 Filament Growth

In the previous sections it was investigated how the topology of MoO_3 agglomerations depends on the doping concentration and how it can be influenced by changing the substrate temperature during the deposition process. Now the question arises which processes lead to the observed nanofilament structure and which energetic factors influence the filament growth. This issue will be addressed in the present section.
For inorganic semiconductors growth is understood quite well and models exist to quantitatively explain the processes which lead to certain structures and morphologies. This enables to control and predict the crystal growth for such systems. For a detailed description about thin film growth see, for instance, Ref. [137]. Regarding the growth of organic thin films, additional factors have to be taken into account, which make the description more complex. The most elementary difference is the fact that organic molecules are extended objects. This additionally leads to various internal degrees of freedoms that have to be considered[138]. A detailed list of differences between organic and inorganic growth and influencing factors can be found in Ref. [138].
For describing the growth of CBP:MoO_3 composites, the issue that two species which are deposited simultaneously have to be taken into account, additionally. To make the process even more complicated, one of the employed materials is inorganic, whereas the other one is organic. As could be seen from the electron tomography results presented in section 4.1.3 and 4.1.4, a quite disordered topology is observed which does not consist of a defined structure with comparable agglomeration lengths and defined orientations with respect to the substrate. Instead, filaments with varying lengths and orientations occur which often also branch out. However, several conclusions can be drawn which allow for a better understanding of the observed nanofilament growth.
It was shown in section 4.1.4 that cooling down the substrate during the evaporation process leads to shorter filaments than growth with the substrate at room temperature. There-

fore, it can be assumed that the growth process which leads to the observed MoO_3 agglomeration is diffusion driven. This assumption is also supported by the findings of Lee et al.[131] who found that the distribution of cluster sizes for films grown at room temperature obey a log-normal trend, which indicates a diffusion process on the substrate surface. It has to be said that this interpretation does not seem to be an appropriate explanation for their assumption of spherically shaped clusters homogeneously distributed over the sample volume. However, it seems to be applicable for the agglomeration structure found in this work. Nonetheless, as already discussed in section 4.1.5, the different agglomeration sizes, which they observed, might also be due to the fact that the filaments do not grow exactly perpendicular to the substrate which might in the projection give the impression of different agglomeration sizes.

As already mentioned in section 3.3.1, it was found by mass spectroscopy that MoO_3 vapor consists mainly of Mo_3O_9 clusters. The growth process of the CBP:MoO_3 composites can be suggested as follows. Since MoO_3 forms the observed nanofilament structure, it is assumed in the following that only the behavior of MoO_3 is crucial for the growth description and CBP just serves as filling material. CBP and Mo_3O_9 impinging on the surface can diffuse for a certain amount of time. In the initial stage of growth, the nucleation stage, several processes can pass off. When two Mo_3O_9 clusters meet they stick together and can diffuse on the surface. Possibly they meet either single Mo_3O_9 clusters or also larger Mo_3O_9 clusters they can agglomerate with. Depending on which growth mode prevails, this process proceeds until either the whole layer is filled, so that diffusion within the layer is not possible anymore, or until they are buried by species coming from above. Since filaments arise which are also extended in the direction perpendicular to the substrate the advanced growth stage must be a growth mode where the already available Mo_3O_9 clusters serve as seed crystals. Therefore, when additional Mo_3O_9 clusters impinge on the surface they either come directly down at an existing filament fragment and immediately stick there or they diffuse until they meet an underlying initial nucleus on top of which they get stuck. Before they stick to an existing nucleus after diffusion, of course also nucleation processes like described above can occur. Besides, as will be described below, they can also form a new initial nucleus from where further filament growth can occur.

For low doping concentrations only short filaments were observed which were concluded from XPS measurements to grow in length for increasing doping concentration until they reach a certain length at about $9\ \mathrm{mol}\%$ doping concentration. This can be explained as follows. If no incoming Mo_3O_9 exists whose diffusion length is sufficient to reach a certain Mo_xO_y filament fragment, growth of this filament stops. For higher doping concentrations, there are of course more dopants available. Therefore, assuming a constant diffusion length, independent of the doping concentration, the probability is higher for higher rates that a certain filament can be reached by one or several dopants and continues to grow. Therefore, for increasing doping concentrations the filament length increases until at about $9\ \mathrm{mol}\%$ the filament length stays constant since on average all filaments are met by incoming dopants. Even then, due to the statistic nature of the growth process, it happens from time to time that no Mo_3O_9 cluster can reach certain filaments and they stop growing. Of course this consideration might be somehow simplified since higher evaporation rates also yield lower diffusion lengths, since processes like filling layers or burying by species coming from above occur within a shorter time frame. From the observations made it seems that this effect is cancelled by the fact that the filament distance decreases with increasing doping concentration.

It was shown in section 4.1.4 for a sample with $9\ \mathrm{mol}\%$ MoO_3 doping concentrations that the filament length decreases when the substrate temperature is lowered. This is probably due to the fact that the energy of the molecules, which arrive onto a substrate at a lower temperature, is quicker dissipated into the substrate than for a substrate at a higher temperature. Therefore, for lower temperatures the diffusion length decreases and therefore the probability that incoming dopants reach an existing filament fragment, which then leads to shorter filaments.

Electron tomography reveals that there are also filaments starting to grow in between and also the three-dimensional reconstruction of the sample with the CBP interlayer (see Figure 4.14) shows that filament growth can start on CBP. This implies that the nucleation stage is independent from the substrate and nucleation can also start in between the growth onto CBP Since a discrepancy of evaporated dopants and dopants detected in the three-dimensional reconstruction was shown in section 4.1.5 to exist it might also happen that Mo_xO_y clusters stick in between where they do not give contrast in bright-field or electron tomography measurements.

Now the question arises by which factors the diameter of the nanofilaments is determined. This question can be addressed referring to three results, presented in the previous sections. First, since for constant substrate temperatures the diffusion lengths of the molecules on the surface would be expected to stay constant, lower doping concentrations should lead to smaller agglomeration diameters. Nonetheless, in section 4.1.3 the agglomeration diameters for 0.6 vol% and a fifteen times higher doping concentration of 9 vol% were found to be constant. Secondly, it would be expected that for higher evaporation rates the diffusion lengths decrease since there is less time for the molecules to diffuse onto the surface and agglomerate with other molecules until they are buried by the next layer. Still, FTIR measurements revealed that a three times higher evaporation rate does not influence the interface area. Therefore, this measurement suggests that the evaporation rate does not have a major impact on the topology, including the filament diameter. Thirdly, it would be expected that cooling down the substrate during evaporation would decrease the diffusion length and therefore cause smaller feature sizes with decreased filament diameter. Indeed, as shown in section 4.1.4, a comparison of two samples evaporated at room temperature and onto a substrate at 120 K, this is the case regarding the length of the filaments. Nonetheless, lowering the temperature still results in a constant filament diameter. In summary, neither the doping concentration, nor the deposition rate, nor the substrate temperature seems to influence the agglomeration diameter within one layer of the organic film. Instead, all observations point to the fact that there is an ideal agglomeration size which is probably from an energetic point of view the most stable size, so that larger as well as smaller agglomeration sizes might not be stable.
Still, probably choosing extremely high or low values as parameters for thin film growth would be expected to lead to smaller agglomeration diameters. For example extreme lowering of the substrate temperature would result in a significant decrease of the diffusion length. Very low doping concentrations, where the probability for Mo_xO_y clusters to meet other clusters of the same species to agglomerate with would be very unlikely, would also lead so smaller agglomeration diameters. And also an extreme enhancement of the evaporation rate should have the same effect since the condition that the dopant becomes immobile due to overlying molecules and molecules in the same layer is reached much faster, which implies a lower diffusion length. However, smaller agglomeration diameters could not be observed for doping concentrations, temperatures and rates which were

applied in the experiments within the scope of this work, which are in the range of typical parameters used for thin film and device fabrication. Therefore, considering commonly used parameters in the field of organic electronics, a common stable filament diameter for the observed material system can be concluded.

The optimal agglomeration diameter might also be determined by the dopant. It can be supposed that the optimal cluster size depends on the material. Indeed, Lee et al.[131] could show that different TMOs exhibit different agglomeration diameters. Since different agglomeration sizes in the projection of the bright-field images can also indicate different filament lengths and also the size of a single dopant might have an influence on the observed agglomeration size this would require further research and electron tomography of different material systems, doping concentrations and substrate temperatures had to be studied to fully answer this question.

The fact that FTIR measurements revealed a post-clustering process upon warm up of the cold deposited film (see section 4.1.4), directs towards the point that after growth the thin film does not exhibit the thermodynamically most stable configuration. Instead it seems as if the molecules already incorporated in the film are still mobile within the film, at least to a certain extent, and can be thermally activated by adding energy, i.e. temperature, to reach a energetically more favorable structural configuration.

Also the question arises why MoO_3 agglomerates within the CBP matrix and is not dispersed homogeneously. Possible explanations would be that MoO_3 is accumulated at domain boundaries of CBP nanocrystals as packing for the molecules to maximize pi-orbital overlap might be energetically favorable[110]. Another probable explanation is the high surface energy of MoO_3 which leads to the tendency to decrease its surface. This can be expected since inorganic materials normally posses higher surface energies than organic molecules. This is due to the presence of dangling bonds at the surface of inorganics which leads to high surface energies, whereas organic materials normally exhibit a closed-shell, which leads to low surface energies[138]. Also the observation made from FTIR that adding more energy by warming up the film leads to an increased MoO_3 surface (see section 4.1.4) supports this theory.

4.2 Electronic Properties

In the following section XPS and FTIR spectroscopy experiments, which give insight into the electronic properties of CBP films doped with MoO_3, are summarized. All measurements presented in this section were performed and analyzed by M. Kühn[49] (PES) or T. Glaser[112,118] (FTIR spectroscopy) within the scope of their respective diploma and PhD thesis in their respective working groups at the University of Darmstadt and the University of Heidelberg. Most of the FTIR spectroscopy results were already published in Ref. [118]. The first part of this section gives an overview on measurements of the CBP/MoO_3 interface, whereas in the second part investigations about doped films are presented.

4.2.1 The CBP/MoO_3 Interface

The interface of CBP and MoO_3 was investigated using an interface experiment, where CBP was deposited onto MoO_3 in a stepwise fashion and PES spectra were acquired after each deposition step[49]. The C1s, O1s, Mo3d and N1s emission lines as well as the secondary electron cutoff and the HOMO onset were measured in dependence of the film thickness. Because the energetic positions of the O1s and Mo3d emission lines do not shift, it can be concluded that the Fermi level in the MoO_3 layer stays constant, i.e. no band bending occurs at this side of the interface. The situation is different in the CBP phase. The binding energy of the respective emission lines, C1s, N1s and HOMO-onset, increases with increasing CBP coverage and all emission lines shift by the same amount. This behavior, with a maximum shift of $0.85\ \mathrm{eV}$, indicates band bending, because a space charge region forms in the CBP phase. The devolution of the secondary electron cutoff reveals an interface dipole of $1.15\ \mathrm{eV}$. This interface dipole lowers the work function difference of neat CBP and MoO_3, which was determined to amount to $2\ \mathrm{eV}$, and therefore reduces the driving force for the charge transfer. The remaining work function difference of $0.85\ \mathrm{eV}$ is compensated by a long range charge transfer which leads to the already above mentioned formation of a space charge region in the CBP phase in order to align the Fermi level. The resulting band diagram with all measured energy values is depicted in Figure 4.23.

Charged CBP and MoO_3 species, as result of charge transfer from CBP to MoO_3, can also be observed during the interface experiment. Regarding CBP, the C1s spectra ex-

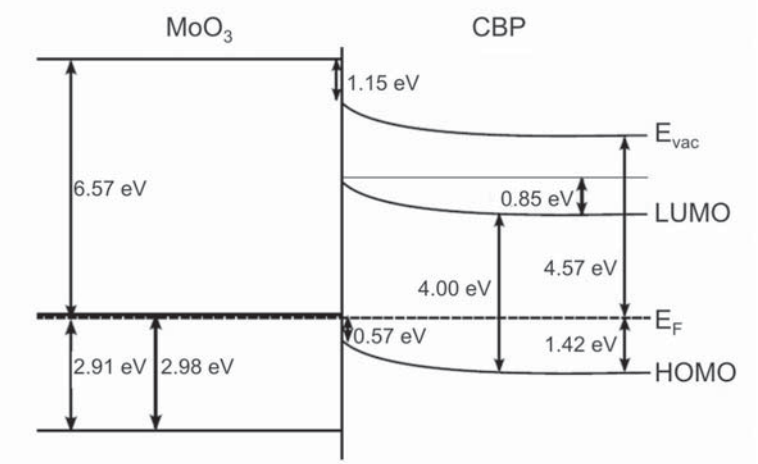

Figure 4.23: Band energy diagram of a CBP/MoO_3 bilayer. The image is taken from Ref. [49].

hibit a shoulder at higher binding energies whose intensity increases for increasing CBP thickness. Comparison with DFT calculations reveals that this shoulder is due to the presence of CBP cations. On the other hand, the measurements of the Mo3d-spectra reveal a shoulder at lower binding energies[49] which can be assigned to the reduced species of molybdenum oxide, i.e. $Mo^{+17/3}$ (see section 4.1.3).
To determine the vertical distribution of MoO_3 anions more precisely, angle-resolved PES measurements were performed additionally. The Mo3d and C1s emission peaks of a sample consisting of MoO_3 with a 9 Å thin CBP layer on top were measured under different tilt angles of the sample surface with respect to the analyzer. Since the PES measurements are very surface sensitive the probed sample depth changes with different tilt angles so that with higher angles one can see deeper into the MoO_3 layer, assuming that the mean free path of the electrons is angle-independent. For MoO_3 it turned out that for decreasing tilt angles, i.e. lower penetration depth, the amount of the reduced MoO_3 species increases. Since lower measurement angles imply higher surface sensitivity, this result shows that the reduced molybdenum oxide species $Mo^{+17/3}$ is confined to the interface.

4.2.2 Electronic Investigations of Doped Films

After revealing the energetic situation at the CBP/MoO_3 interface in the previous section, the current section will deal with the energetic issues of doped films. It will be shown that the process of p-type doping, which goes along with charge transfer from CBP to MoO_3, cannot only be deduced from the fact that the conductivity increases with increas-

ing doping concentration, but can be observed on an electronic level using PES and FTIR spectroscopy.

4.2.2.1 Influence of Charge Transfer on Electronic Properties

PES

Using PES, doped films with different MoO_3 concentrations were investigated. The C1s, N1s, Mo3d and O1s lines, as well as the HOMO onset, were found to shift towards lower binding energies with increasing molybdenum oxide content. The maximum shift between the pristine CBP layer and the sample with the highest doping concentration was found to amount to $1\ \mathrm{eV}$. Since all shifts run parallel, the Fermi energy moves within the band gap towards the HOMO indicating p-type doping of the organic CBP matrix. According to the internal interface charge transfer model, presented in section 2.3.3, the value the maximum Fermi level shift of doped films lies in between the values determined from a dopant/matrix interface experiment with both layer sequences when dopant agglomerations are present. Due to charging effects no values for MoO_3 grown on CBP could be determined. Nonetheless, it can be concluded that a quite good agreement of interface experiment and investigation of the doped films was found. For the Fermi level shift a slight difference of $1\ \mathrm{eV}$ for doped films and $0.85\ \mathrm{eV}$ for the interface experiment was measured. This directs towards the applicability of the internal interface charge transfer doping model.

In Figure 4.24 the energetic shifts of the C1s and the Mo3d line, as well as the HOMO onset, are exemplary plotted against the doping concentration. For low doping concentrations, a steep decrease of all three quantities can be identified. From the steepness, information about the doping efficiency, i.e. how many dopants are needed for a certain Fermi level shift, can be inferred. A saturation is found for high doping concentrations.

FTIR Spectroscopy: Electronic Excitations

From FTIR spectroscopy measurements also evidence for charge transfer from CBP to MoO_3 can be inferred. Two energy ranges were considered: the fingerprint region ($600\ \mathrm{cm}^{-1}$ to $1700\ \mathrm{cm}^{-1}$) where excitations due to molecular vibrations can be examined, and the transition region between mid IR and near IR, where electronic excitations can be

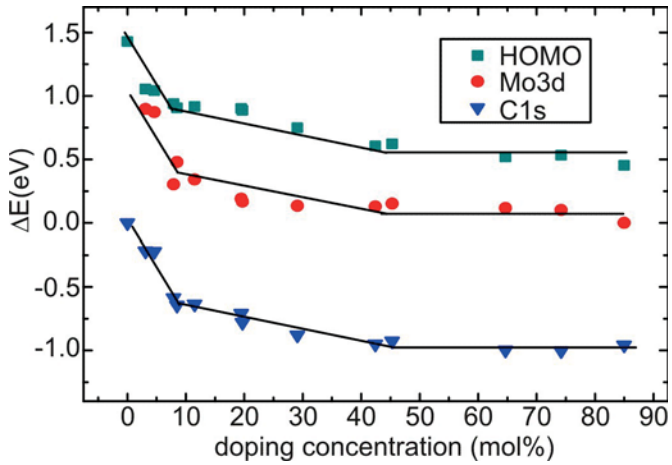

Figure 4.24: Energetic shift of the C1s, the Mo3d line and the HOMO onset in dependence of the MoO_3 doping concentration. The displayed data was measured and analyzed by M. Kühn.

identified. In both energy regimes changes in the spectra of the doped films occur which get more pronounced with increasing doping concentration.

In section 2.3.2 it was already pointed out that for various material combinations of doped organic films, measurements were performed that direct towards the formation of charge transfer complexes. Glaser et al.[118] examined CBP films doped with MoO_3 for different doping concentrations. They found that spectra of doped films exhibit a broad excitation in the transition region of mid and near IR above $2000\ \mathrm{cm}^{-1}$ which does not appear in the spectra of the pure materials. The intensity of this excitation was found to increase with increasing doping concentration. According to its energetic position and its distinct width this band must be due to an electronic excitation. It indicates that charge transfer complexes are formed and that the electronic excitation is due to the optical excitation of an electron from the binding into the antibinding hybrid orbital[112] (see section 2.3.2). Since the charge transfer complexes can only occur at the interface of CBP and the MoO_3 filaments, the intensity of this broad excitation can also be used as a measure for the CBP/MoO_3 interface in the doped layers[112] (see also section 4.1.4). The electronic excitation was shown to be a superposition of three bands located at $3805\ \mathrm{cm}^{-1}$, $5187\ \mathrm{cm}^{-1}$ and $7090\ \mathrm{cm}^{-1}$. The fact that excitations at different energies are detected might be due to different relative orientations of CBP and MoO_3, which cause different energy levels of binding and antibinding orbitals. This assumption is also supported by the fact that

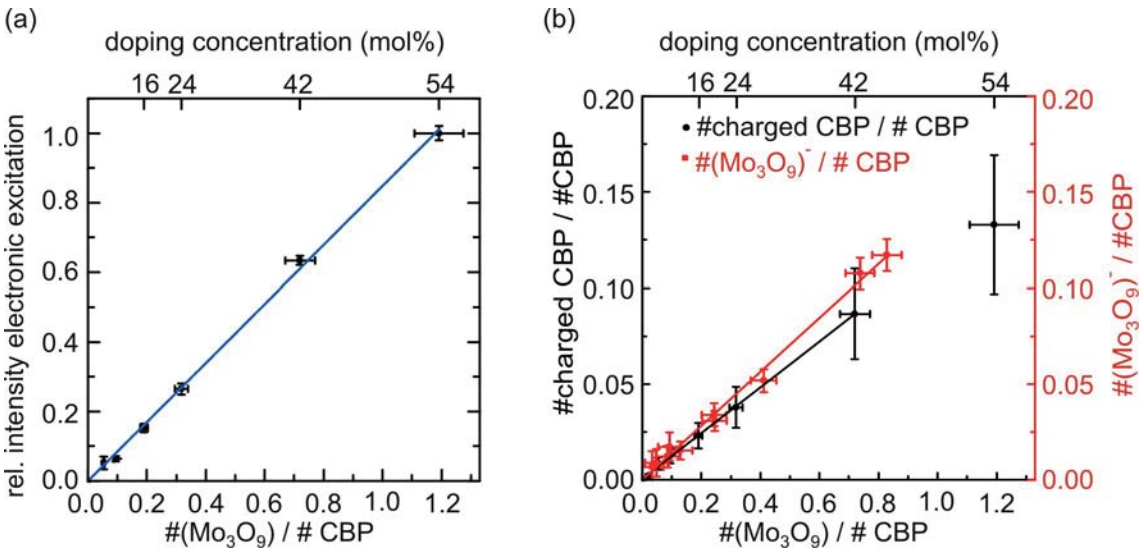

Figure 4.25: (a) Relative intensity of the electronic excitation of MoO_3-doped CBP films as a function of the doping concentration.
(b) Ratio of the number of charged CBP molecules respective Mo_3O_9 clusters and the total number of CBP molecules as a function of the ratio of Mo_3O_9 clusters and CBP molecules inferred from FTIR spectroscopy respectively PES measurements.
The displayed data was measured and analyzed by T. Glaser and the image is taken from Ref. [112].

an intensity decrease for the band corresponding to the lowest energy ($3805\ \mathrm{cm}^{-1}$) was found when samples evaporated onto cooled substrates were annealed[112]. This implies that the relative orientation of the molecules can be influenced by the temperature which leads to energetically more favorable positions for higher temperatures. As described in Ref. [112], fitting of the electronic absorption was performed by using three Lorentz oscillators, whose position, ratios of oscillator strengths and damping values were determined by a fit of the sample with $54\ \mathrm{mol}\%$. For the other concentrations, the only fitting parameter was a factor by which the oscillator strengths of the three Lorentz oscillators were scaled. The square of this scaling factor is then proportional to the area of the broad absorption and also proportional to the interface area of MoO_3 filaments and CBP[112]. Since all fits are in good agreement with the measured data it can be concluded that the electronic structure at the interface does not depend on the doping concentration[112].

In Figure 4.25 (a) the intensity of the broad absorption is plotted against the ratio of the number of Mo_3O_9 clusters and the number of CBP molecules. Compared to the doping concentration in mol%, this quantity has the advantage, that it increases linearly with the number of Mo_3O_9 clusters. Up to $54\ \mathrm{mol\%}$ the intensity of the electronic absorption increases linearly with doping concentration. Since the hybrid orbitals can only form at the MoO_3/CBP interface this means that the interface also increases linearly with the amount of Mo_3O_9.

FTIR Spectroscopy: Fingerprint Region

Considering the fingerprint region ($600\ \mathrm{cm^{-1}}$ to $1700\ \mathrm{cm^{-1}}$), additional absorption bands can be identified in the doped films which do not appear in the spectra of the pristine materials. The intensity of these additional peaks increases with the doping concentration. Comparing the experimental spectra with spectra obtained from quantumchemical calculations, it turned out that these additional peaks can be assigned to CBP cations (CBP^+) which evolve from the charge transfer from CBP to MoO_3 [112]. Since MoO_3 does not show any features above $1000\ \mathrm{cm^{-1}}$ these modes cannot be due to vibration modes of MoO_3. The spectra of neutral CBP and the CBP cation differ from each other since the removal of one electron causes a change in the electronic structure. This leads to changes of bonding lengths and bonding strengths in the molecule causing a modified FTIR spectrum [112]. At the same time the intensity of bands which can be assigned to neutral CBP molecules decreases with increasing doping concentration. It was found that both, the increase of CBP cations and the decrease of neutral CBP molecules, is proportional to the amount of Mo_3O_9 clusters in the doped layers, as it would be expected for a charge transfer.

The CBP cation spectrum was extracted from the experimental spectra of the film with $54\ \mathrm{mol\%}$ MoO_3 concentration as described in Ref. [112]. The good correlation of the cation spectrum extracted from the measurement and the quantumchemically calculated spectrum of CBP^+indicates that within a charge transfer complex one electron is transferred from the CBP molecule to MoO_3 [112].

Spectra of the doped films were simulated, using a superposition of the spectra of neutral CBP and the CBP cation for the frequency range from $1100\ \mathrm{cm^{-1}}$ - $1700\ \mathrm{cm^{-1}}$. For this simulation the relative ratio c of the CBP cation spectrum, which is proportional to the number of CBP cations, was used as fit parameter. Since there is a very good correlation

of experimentally measured and simulated spectra, the spectral changes in the films with different doping concentrations can be explained by a charge transfer from CBP to MoO_3 and indicate that no interaction between neutral CBP molecules and CBP cations takes place. The quantitative analysis of these results will be presented in section 4.2.2.2.
In section 4.1.4 it was already mentioned that the intensity of the electronic excitation indicates a 1.7 fold higher interface area for a sample which was evaporated onto a substrate kept at $120\ \mathrm{K}$, compared to a sample where the substrate was held at room temperature during evaporation. Regarding the fingerprint region, increasing intensity for cooled films was also observed for absorption bands which can be assigned to the CBP cations. For a sample with $24\ \mathrm{mol\%}$ doping concentration the fit revealed that 1.4 times more CBP cations are present in the cooled sample as in the room temperature one. Since for $24\ \mathrm{mol\%}$ an increase of 1.7 was found for the surface-to-volume ratio determined via the intensity of the electronic absorption, but only a 1.4 fold increase of CBP cations determined via the intensity of the vibrational modes, the number of CBP seems not to be proportional to the organic/filament interface.

4.2.2.2 Doping Efficiency

As already mentioned in section 1.1, the doping efficiency of the material system CBP:MoO_3 was found to be unexpected low. Information about the doping efficiency can also be inferred from XPS and FTIR spectroscopy measurements.
From FTIR spectroscopy measurements the ratio of charged CBP molecules to the total number of CBP molecules could be determined in dependence of the ratio of the amount of Mo_3O_9 clusters to the overall number of CBP molecules. As described in the previous section, this was done by fitting the spectra of the doped layers using a superposition of the spectra of pure CBP and the CBP cation.
To get information about the other species involved in the doping process, i.e. MoO_3, additionally the ratio between charged Mo_3O_9 clusters and the overall number of CBP molecules was determined in dependence of the ratio of the amount of Mo_3O_9 clusters to the total number of CBP molecules using XPS measurements (see section 4.1.3). As already explained in section 4.1.3, d-orbital aromaticity was assumed, which leads to an oxidation state of +17/3 for charged MoO_3 [136]. Other than for CBP cations there is no band bending present at the MoO_3 side of the interface experiment depicted in section

4.2.1. Therefore, it can be assumed that all charged dopants are located at the interface and the shoulder in the Mo3d spectra is both, a measure for the interface area (see section 4.1.3) and a measure for the total amount of charged MoO_3 species. This is different for the FTIR spectroscopy results related to CBP, since band bending was measured in the PES interface experiment at the CBP side. Therefore, the vibrational excitations of the CBP cation cannot be seen as a measure for the interface, since they include both, free charges and charge transfer complexes.

A comparison of the XPS and FTIR spectroscopy measurements is depicted in Figure 4.25 (b). Both measurements reveal a linear relationship of CBP cation respectively MoO_3 anion content with increasing doping concentration. From the results in Figure 4.25 (b) a slope of 0.14 ± 3 was extracted from the XPS results[49], whereas the slope obtained by the FTIR spectroscopy measurements amounts to 0.11 ± 3 [112]. Since both measurement techniques reveal a very good agreement, this result indicates that in a first approximation all charge carriers which are in the scope of the doping process transferred from CBP to MoO_3 can indeed be found at the MoO_3. For both techniques a deviation from this linear relation can be identified for higher doping concentrations, which can, according to section 4.1.3, be explained by formation of a MoO_3 network and was not taken into account for determining the slope[5].

As already mentioned in section 1.1, Hamwi et al. determined a doping efficiency of $1 - 2\ \%$ for MoO_3-doped CBP[37]. These values were deduced from Kelvin probe measurements that reveal the number of free charge carriers. The discrepancy between these values and the results obtained from FTIR spectroscopy and XPS, which were presented above, is probably due to the fact that Kelvin probe analysis determines the number of free charge carriers, whereas FTIR spectroscopy and XPS determine the overall number of charged species. The latter consists of both, charges which are localized at the filament interface and are bound there as charge transfer complexes due to the high Coulomb interaction between the transferred charge and the resulting countercharge and charge carriers which were dissociated and can move freely through the material thereby increasing the number of free charge carriers[112] and inducing the Fermi level shift observed by XPS. From the values stated above, a dissociation probability of $17\ \%$ (using the FTIR

[5] In section 4.1.3 for low doping concentrations a regime with decreasing doping efficiency was found. The fact that this regime cannot be detected in Figures 4.25 (a) and (b) is due to the different scaling.

results) can be calculated, which implies that only $17\ \%$ of the transferred charges which are initially present as charge transfer complexes can dissociate and increase the conductivity. On the other hand the remaining $83\ \%$ of the transferred charges stay bound at the CBP/MoO_3 interface and cannot contribute to the current flow. Since the analysis applied in Ref. [37] relies on a model valid for inorganic semiconductors, the exact value of this dissociation probability might be arguable.

4.3 Electrical Measurements

In the following section, electrical measurements on MoO_3-doped CBP films are presented. The electrical anisotropy is investigated and activation energies for different doping concentrations are determined. Beside, also the influence of the substrate temperature during evaporation on the electrical properties is examined. Only the measurement results are shown in this section, while a conclusive interpretation will be presented in section 4.4.

4.3.1 Probing the Electrical Anisotropy

It was shown in section 4.1.3, that MoO_3 forms a filamentous dopant structure with a preferential orientation, when co-deposited with the organic semiconductor CBP. Hence, the question arises, if this anisotropic topology has an influence on the electrical properties and leads to orientation dependent effects regarding charge transport.
To investigate this issue, hole-only devices with two different device structures were fabricated, as described in section 3.3.4.1. These allow to probe the electrical properties in two directions perpendicular to each other. For the stripe structure (see Figure 4.26 (a)), current flow occurs perpendicular to the substrate, when a voltage is applied between the two contacts. This leads to charge transport parallel to the nanofilaments (Figure 4.26 (b)). In contrast, for the finger structure, depicted in Figure 4.26 (c), current transport takes place parallel to the substrate. This corresponds to current flowing perpendicular to the nanofilaments (Figure 4.26 (d)). A series of hole-only devices was fabricated. The active layers consisted of neat CBP respectively MoO_3, as well as CBP:MoO_3 composites with varying doping levels ranging from $1.6\ \mathrm{mol}\%$ to $68.4\ \mathrm{mol}\%$ MoO_3.

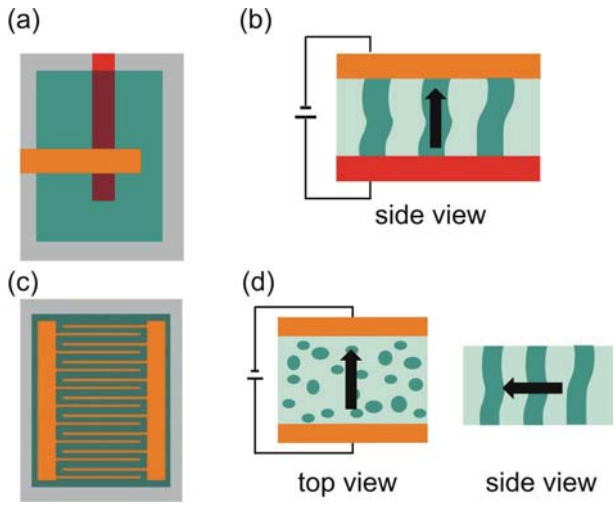

Figure 4.26: To measure electrical properties in different directions, two different device layouts were used.
(a) and (b): With the so called stripe structure, current flow occurs perpendicular to the substrate, i.e. parallel to the MoO_3 filaments.
(c) and (d): The finger structure allows to investigate the electrical properties parallel to the substrate, i.e. perpendicular to the filaments.

The measured electrical characteristics for finger and stripe devices are shown in Figures 4.27 (a) and (b). To allow for comparison of both structures, as well as varied active layer sizes, instead of plotting the applied voltage U versus the measured current I, current density j is plotted against electrical field E.
In Figures 4.27 (a) and (b) the log-log representation of the j-E characteristics is depicted. It exhibits a linear dependence with a slope of 1 at low fields, indicating ohmic charge transport (see section 2.4). For each doping concentration, the conductivity σ was derived from a linear fit of this ohmic regime according to equation (2.4.1). The calculated conductivity σ is displayed as a function of the doping concentration in Figure 4.28. The mean conductivity for all devices on one substrate is depicted by one data point and the discrepancy between the conductivities of the single devices is given as standard deviation. For some doping concentrations, several samples were prepared, providing the possibility to estimate the reproducibility of the samples.
For finger as well as stripe structures a saturation of the conductivity towards the value of neat MoO_3 was found for high doping concentrations and the conductivity could be varied by over 6 orders of magnitude. However, one has to mention that the value for the neat

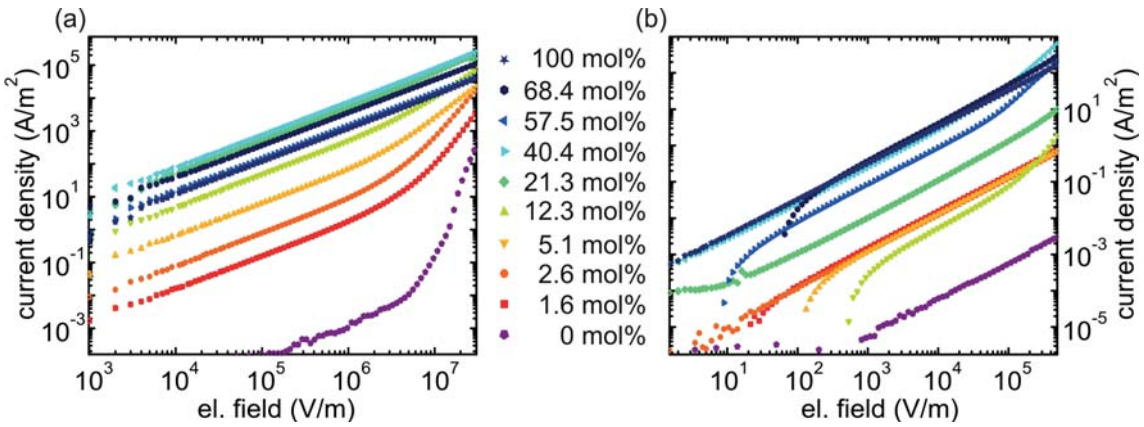

Figure 4.27: IV characteristics of hole-only devices of CBP doped with different concentrations of MoO_3 with (a) current flow parallel to the MoO_3 filaments and (b) current transport perpendicular to the MoO_3 filaments. For each doping concentration only one IV characteristic is displayed to ensure a good overview.

CBP devices might be debatable since degradation (i.e. crystallization and finally dewetting) of neat CBP occurs on a short timescale. The degradation process can be suppressed to a great extent by incorporation of MoO_3 dopants. This can already be observed by eye and was also confirmed by AFM measurements (not shown here). The observed conductivity dependence is in quite good accordance with Ref. [36] where also an increase in conductivity was observed for CBP samples with MoO_3 doping concentrations up to about $20\ \mathrm{mol\%}$. Doping MoO_3 into other matrices, namely TCTA respectively α-NPD, led to the observation that, also in this case, the conductivity saturates towards the value of neat MoO_3 for high doping concentrations and charge transport perpendicular to the substrate[139]

For the stripe structure, a rapid increase of the conductivity is found for low MoO_3 concentrations up to $21.3\ \mathrm{mol\%}$, followed by saturation towards the value of neat MoO_3. For the finger devices the behavior of the conductivity is different. Between $1.6\ \mathrm{mol\%}$ and $12.3\ \mathrm{mol\%}$ the conductivity does not change within the measurement accuracy. This constant regime is followed by a significant conductivity increase for concentrations up to $40.4\ \mathrm{mol\%}$. Finally, the conductivity value also saturates towards the MoO_3 value within the measurement accuracy.

To summarize, a different behavior of the conductivity as a function of doping concentration was identified for different orientations of charge transport. This observation in-

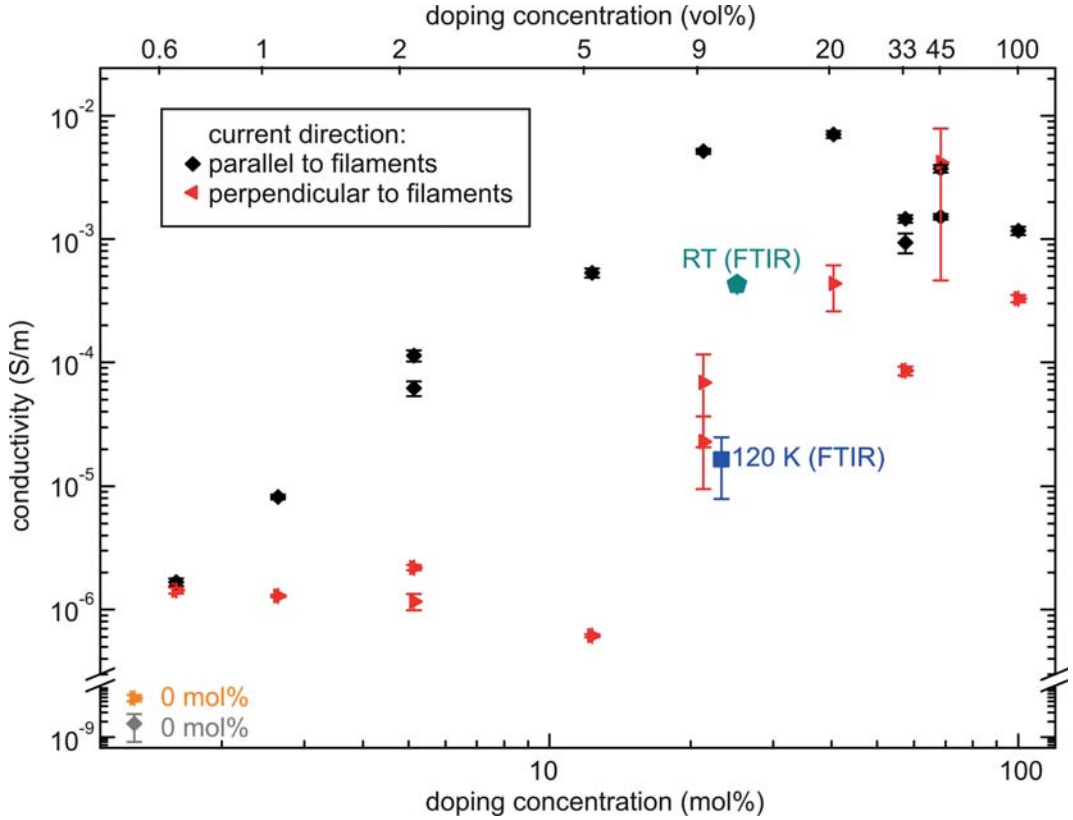

Figure 4.28: Conductivity of CBP films with varied MoO_3 concentrations for current flow parallel (black diamonds) and perpendicular (red triangles) to the filaments. The samples were evaporated in organic chamber 2 of the clustertool. Also the conductivity values for charge transport parallel to the filaments are depicted, where the active layer was evaporated in the FTIR tool with the substrate at room temperature (green pentagon) respectively 120 K (blue square). The mean conductivity for all devices on one substrate is depicted by one data point and the discrepancy between the conductivities of the single devices is given as standard deviation.

dicates that current transport must strongly be influenced by the observed nanofilament topology. A more detailed discussion on this observation will be presented in section 4.4.2.

4.3.2 Determination of Activation Energies from Temperature-Dependent IV Measurements

As described in section 3.2.3.1, temperature-dependent IV measurements were conducted to obtain activation energy values for different doping concentrations. The data presented in this section were acquired and analyzed within the scope of Alexander Müller-Brand's[140] and Markus Gölz's master thesis[141]. Each sample was first measured in ambient air at room temperature, as described in the previous section. This allows for comparison with the measurements inside the cryostat. Temperatures were varied from $320\ \mathrm{K}$ to $80\ \mathrm{K}$ and back to $320\ \mathrm{K}$ in $10\ \mathrm{K}$ steps. Since slight deviations were found for the two measurement directions, which were assigned to degradation and charging effects, only the measurements from $320\ \mathrm{K}$ to $80\ \mathrm{K}$ were considered for data analysis. Measurements for each temperature were started automatically as soon as the temperature varied by less than $50\ \mathrm{mK}$ for at least $2\ \mathrm{min}$. To validate reproducibility, usually at least two devices were measured.

As an example, the temperature dependent IV characteristics of samples with $2.6\ \mathrm{mol\%}$ and $68.4\ \mathrm{mol\%}$ doping concentration are depicted in Figures 4.29 (a) and (b). These measurements visualize the presence of a stronger temperature dependence for lower than for higher doping concentrations. To quantify the temperature dependence, the currents for each temperature were extracted for different voltage levels to determine the activation energy according to equation (2.3.4).

As it is expected for doped systems (see section 2.3.4), it was found that the observed temperature dependence can be better described using a $\log j \propto 1/T$ than a $\log j \propto 1/T^2$ dependence. For data analysis, the current was plotted logarithmical against the inverse temperature $1/T$. The activation energy E_a could then be determined according to equation (2.3.4) by a linear fit to this plot. A linear dependence of $\log j$ on $1/T$ is only present for moderate temperatures, whereas for high and low temperatures a significant deviation from this trend can be identified. As already pointed out in section 3.3.4.1, this is due

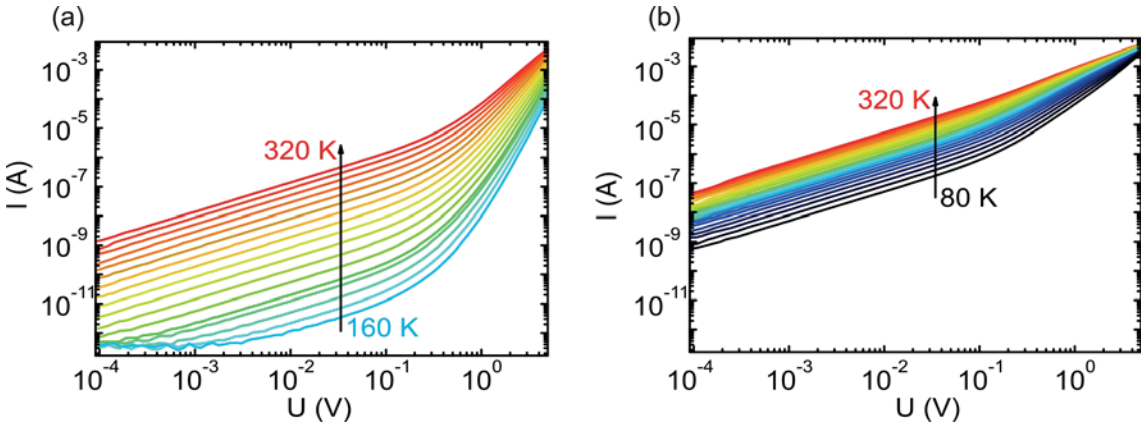

Figure 4.29: Temperature-dependent IV characteristics of hole-only devices with (a) 2.6 mol% and (b) 68.4 mol% MoO_3 concentration.

to the fact that the charging current (related to the RC time) has a significant influence for low currents, whereas for high currents contact resistance effects influence the measurements. Therefore, only data points from the linear regime were considered for the determination of activation energies. Since for high electric fields an electric field dependence of the activation energy was found, as expected and already outlined in section 2.2, only very low electric fields were considered for determination of the activation energy.
The results are summarized in Figure 4.30, where the activation energies are plotted as a function of the doping concentration. As for the conductivity values, presented in the previous section, each data point in the diagram depicts the mean value of all devices measured on one substrate and the discrepancy between the conductivities of the single devices is given as standard deviation. Since the temperature-dependent measurements are very time consuming and device degradation may affect the results when devices are too old, up to two devices were measured on each substrate.
Regarding the stripe structures (current flow along MoO_3 filaments), an activation energy of 411 meV was determined for the undoped CBP sample. As for the conductivity values, also here the value for the pristine CBP device might be debatable because of degradation effects. A strong decrease of activation energies was found for doping concentrations from 2.6 mol% to 40.4 mol%. For higher MoO_3 concentrations the activation energy values were constant within the measurement accuracy and approximately equal to the activation energy of pristine MoO_3.

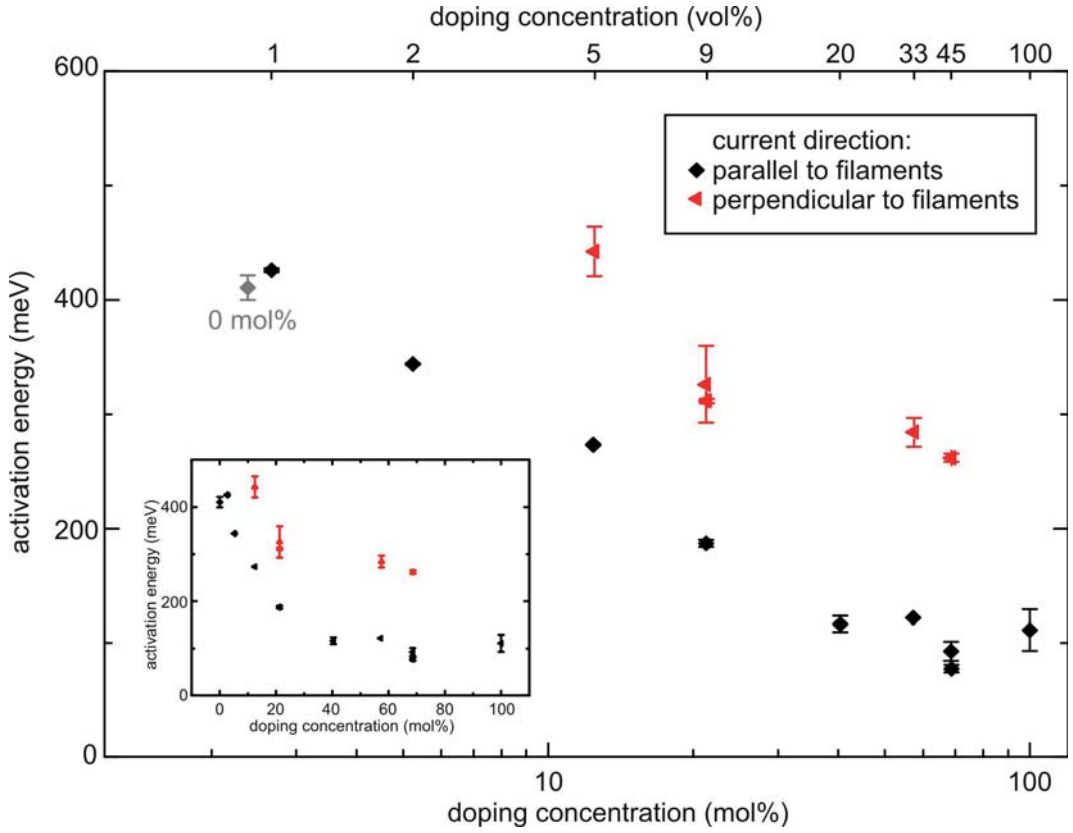

Figure 4.30: Activation energies derived from temperature-dependent IV measurements as a function of the MoO_3 concentration for current flow parallel (black diamonds) and perpendicular to the filaments (red triangles). The mean conductivity for all devices on one substrate is depicted by one data point and the discrepancy between the conductivities of the single devices is given as standard deviation.

Activation energies were also determined for finger devices[6]. As can be seen in Figure 4.30, activation energies for current transport perpendicular to the filaments also decreased for increasing doping concentrations and consistently higher values were found compared to current transport along the filaments.

These results can be compared to UPS measurements, presented in section 4.2.2.1, which provided information about the difference between Fermi level and HOMO onset as a function of the doping concentration. In section 2.3.4 it was pointed out that the activation energy for high doping concentrations approximately equals the difference between Fermi level and transport energy. Both techniques provide information about the Fermi level shift, but relative to the HOMO onset in the case of PES and relative to the transport energy in the case of cryo-IV measurements. Comparing the results (see Figures 4.24 and 4.30), a discrepancy of the absolute values and the amount of Fermi level shift exists. This is due to the fact that the HOMO onset is not compulsory equal to the transport energy. Beside, in the case of cryo-IV measurements, a current is measured and charge carriers take the energetically most favorable conduction paths, which exhibit the lowest activation energies. Because this selection does not occur for PES measurements the observed discrepancy can be expected. However, the two measurement techniques reveal a very good correlation, since for both measurement techniques a strong shift of the Fermi level towards the HOMO onset respectively the transport energies is observed, whereas from about $40\ \mathrm{mol}\%$ on the Fermi level saturates and equals approximately the value of pristine MoO_3.

To conclude, similar to the effect observed for the conductivity, also the activation energy was found to depend on the current direction. Additionally, also a good correlation of UPS and cryo-IV measurements was found.

[6] Since the measurements shown here were the first cryo-IV measurements ever conducted at Innovationlab and initially used for testing the measurement setup, many different issues had to be resolved. Various parts of the used measurement setup had to be constructed. This was done within the scope of Alexander Müller-Brand's master thesis [140]. A contact possibility for the finger devices was not available from the beginning. Hence, only for very few doping concentrations activation energies of finger devices could be determined. Additionally, for low doping concentrations and low temperatures, the currents were too low to be measured with the existing experimental setup and device layout.

4.3.3 Influence of Substrate Temperature on Electrical Properties

In section 4.1.4 it was shown that the substrate temperature during the evaporation process influences the topology and that MoO_3 filaments become shorter in the case of the cooled substrate. This correlates very well with the FTIR spectroscopy results presented in section 4.2.2.1 where for a CBP:MoO_3 film with $24\ \mathrm{mol\%}$ MoO_3 concentration and evaporated onto a cooled substrate, the number of CBP cations increased by a factor of 1.4 , when compared to a sample with the substrate kept at room temperature during deposition. This is expected because for better distributed dopants one expects a higher dopant/matrix interface and therefore more charge carriers. Since, according to equation (2.3.1), the conductivity is proportional to the charge carrier density, also a higher conductivity would be expected for the cooled film. To investigate whether this assumption is true, the influence of the substrate temperature on the electrical properties was studied. Two samples were prepared, one at room temperature, the other one with the substrate cooled down to about $120\ \mathrm{K}$ during the deposition process. The active layers were both grown in the FTIR tool. The sample with the cooled substrate exhibited a doping concentration of $23.1\ \mathrm{mol\%}$ and a thickness of $110\ \mathrm{nm}$, whereas the sample on the substrate held at room temperature during evaporation, had a doping concentration of $25.4\ \mathrm{mol\%}$ and a thickness of $93\ \mathrm{nm}$. Because the FTIR chamber does not allow for in-situ control of the evaporated thicknesses (see section 3.1) a slight difference in doping concentration and active layer thickness exists. Other than the organic active layers, the aluminum contacts and the MoO_3 injection layers were evaporated in the metal chamber of the clustertool with the substrate kept at room temperature for both devices.
Figure 4.31 shows IV characteristics of the two samples. It turned out that the cooled sample exhibited a conductivity which was about one and a half orders of magnitude lower than the sample where the active layer was evaporated at room temperature. The calculated conductivity values are shown in Figure 4.28. The result is not expected on the first sight, since the cold sample exhibits a higher amount of free charge carriers (according to FTIR spectroscopy), but still exhibits a lower conductivity. This reveals that a change in topology strongly influences the electrical properties and points towards the fact that the nanofilament topology facilitates current transport instead of hindering it.

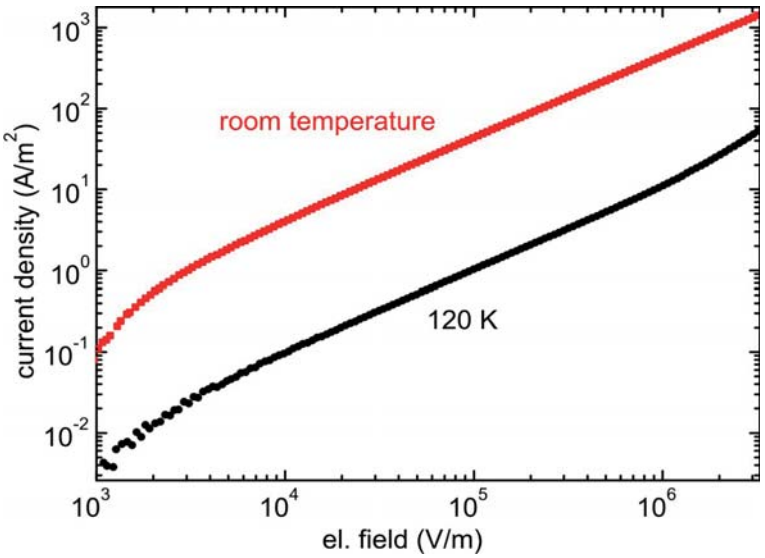

Figure 4.31: IV characteristics of CBP films doped with about 10 vol% MoO_3 concentration evaporated onto a substrate kept at room temperature and a substrate cooled down to about 120 K during the evaporation process.

4.4 Doping Model Based on Structural, Electronic and Electrical Findings

In this section the structural investigations shown in section 4.1, the electronic findings obtained from XPS and FTIR measurements (see section 4.2), as well as the electrical measurements presented in section 4.3, will be correlated. In the first part, all factors which might lead to a low doping efficiency of TMO-doped organic films are summarized, while in the second part a model for charge transport in MoO_3-doped CBP layers is presented.

4.4.1 Factors Influencing the Doping Efficiency

The origin of the low doping efficiency observed for MoO_3-doped CBP films can be attributed to different factors. FTIR and XPS results, presented in section 4.2, revealed that the doping efficiency amounts to only 11 % respectively 13 %, when all charged species, regardless of whether they are bound at the interface or present as free charge carriers, are considered. This points towards the fact that not for all dopants a charge transfer

takes place. One explanation would be that there exists a significant amount of MoO_3, which is not in contact with the organic matrix. It was shown in section 4.1.3, that MoO_3 forms nanofilaments. Assuming that dopants are present inside the agglomerations which do not have contact to the CBP, this would decrease the doping efficiency, since not for all dopants a charge transfer can take place. The filament diameter was determined to amount to about $1\ \mathrm{nm}$. However, as discussed in section 4.1.5, the observable contrast in the bright-field images might lead to an underestimate of the real filament diameter. Since the size of one Mo_3O_9 cluster was found to be about $7 - 8\ \text{Å}$ in size[136] it is questionable if really MoO_3 is present inside the agglomerations, which does not have contact with the organic matrix.

Also energetic explanations for the low doping efficiencies are possible. Lee et al.[131] found that the number of MoO_3 agglomerations agrees with the number of charge carriers determined from C-V measurements. Hence, it would also be conceivable that, due to Coulomb interactions, only a certain amount of charges can be transferred on one filament. As pointed out in section 2.3.2, the formation of charge transfer complexes might lead to an energetic situation at the interface, where only a fraction of the charge transfer complexes can be ionized at room temperature, leading to free charge carriers. Some of the transferred charges would then be bound to the interface in localized charge transfer complexes. Hence, these charge carriers are immobile, cannot contribute to the charge transport and therefore reduce the doping efficiency. This could be concluded from the discrepancy of Kelvin Probe analysis, which gives information about the number of free charge carriers, and FTIR respectively XPS measurements, which include all transferred charges (see section 4.2.2.2). The existence of charge transfer complexes could be inferred from the presence of an electronic excitation which was observed in FTIR spectra at high wavenumbers and its intensity increase with increasing doping concentration (see section 4.2.2.1). In the XPS measurements, the charge transfer complexes manifest themselves as interface dipoles which form upon Fermi level alignment at the interface and therefore reduce the driving force for the charge transfer. The presence of the mobile charge carriers can also be concluded from the XPS measurements, shown in section 4.2, and present itself as Fermi level movement respectively band bending.

4.4.2 Description of Charge Transport in MoO_3-Doped CBP Layers

It was shown in section 4.3.1, that current transport properties are different for current flowing along and perpendicular to the filaments. Therefore, the topology must play an important role for the description of charge transport in MoO_3-doped CBP films and such films may not be considered as being uniform, but also local effects regarding charge transport have to be considered. This assumption is also supported by the finding that activation energies have different values for different current directions (see section 4.3.2).
The results shown in section 4.3.3 revealed, that a lower substrate temperature during film deposition leads to a lower conductivity of the doped layers. This was surprising on first sight, since electron tomography and FTIR measurements revealed that the interface and also the amount of charge carriers increased for the cooled sample, compared to the sample which was deposited at room temperature (see section 4.1.4).
A similar situation was also observed for bulk-heterojunction (BHJ) solar cells. There, excitons can only dissociate at interfaces of donor and acceptor domains. Still, a higher interface area, implying more separated charges, does not mandatorily lead to an increase in photocurrent. Instead, it is also essential that conduction paths exist, so that the charge carriers can be transported to the contacts and contribute to the photocurrent[142]. In the case of BHJ solar cells, these conduction paths are formed by connected donor respectively acceptor domains. Also for the doped films under investigation in this work, the concept of conduction paths seems to be important, since it is apparently not sufficient for good charge transport that high interface areas exist, which cause a high number of charge carriers.
Because XPS measurements revealed that both, CBP cations and MoO_3 anions, are located close to the interface (see section 4.2.1), it can be expected that charge transport takes place along the filaments. Considering the internal interface charge transfer model (see sections 2.3.3 and 4.2.2.1) the energetic situation at the organic/filament interface is similar to the interface determined by the interface experiment on layers of the single materials. This would mean that an extended space charge region is present at the organic side, which extends about $20\ \mathrm{nm}$ into the organic matrix (see section 4.2.1). This space charge region is expected to contain free holes originating from the charge transfer between MoO_3 and CBP. Since the band bending decreases exponentially, this would also

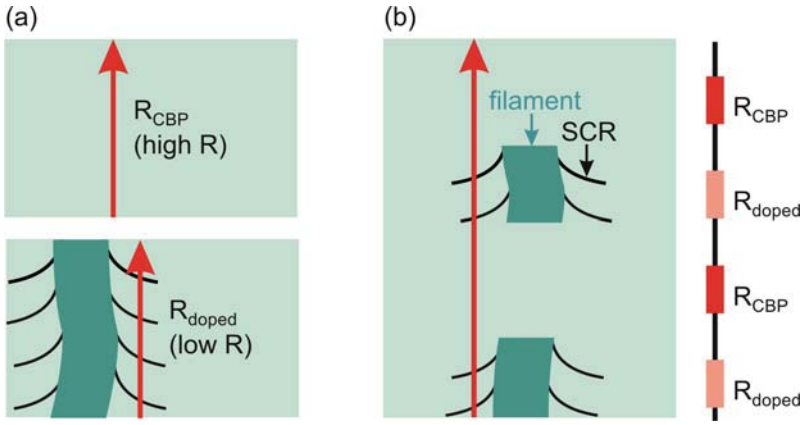

Figure 4.32: Model for charge transport in MoO_3-doped CBP films.
(a) Hole conduction within the space charge regions (SCR) of CBP exhibits a lower resistance than hole conduction within undoped CPB.
(b) For low doping concentrations, where short MoO_3 filaments are present, conduction paths, consisting of a series connection with low and high resistances, can be expected.

mean that the charge carrier density decreases exponentially, making charge transport less likely for higher distances from the filament/matrix interface.

In a first step, current transport along the filaments is considered. Assuming hole transport in the CBP matrix, it can be expected that the space charge regions serve as favored paths for holes, because of an increased charge carrier density, which leads to higher conductivities (see Figure 4.32 (a)). As for all figures in this section, conduction paths of holes are denoted as red arrows and blue arrows are used for electrons. The pathways of the conduction paths are strongly simplified. They will of course not be straight, but charge carriers will take the energetically most favorable paths. According to the electron tomography results (see section 4.1.3), no continuous conduction paths consisting of MoO_3 can be expected for low doping concentrations. In this case, a series connection with low and high resistances is supposable. This means that hole transport takes place along the interface where filaments are present, but must also be conducted partially through neat CBP which exhibits a much lower conductivity (see Figure 4.32 (b)).

In the literature it was also suggested that charge transport proceeds via hopping of electrons between the MoO_3 dopants. Qiao et al.[139] investigated Alq_3 doped with MoO_3 and found an increase of about one order of magnitude in conductivity for a doping concentration of $10\ \mathrm{wt\%}$ ($\approx 5\ \mathrm{vol\%}$) compared to a neat Alq_3 device. However, compared to

the steep conductivity increase of about five orders of magnitude, observed in this work for CBP doped with a comparable amount of MoO_3, it still seems to be unlikely that hopping between MoO_3 agglomerations is an explanation. Assuming also MoO_3 filament growth in an Alq_3 matrix, it would also be supposable that at this high doping concentration already a few continuous MoO_3 filaments exist, so that charge transport can proceed via continuous MoO_3 paths. On the other hand, the electron conductor TPBi doped with $30\ \mathrm{mol\%}$ of WO_3 revealed no significant change of the IV characteristics[23].

In section 4.3.1 it was shown that the conductivity increases significantly with the doping concentration up to $21.3\ \mathrm{mol\%}$. Filament lengths for low MoO_3 concentrations were shown from XPS measurements to increase with increasing doping concentration (see section 4.1.3). Therefore, an increasing fraction of the charge transport path can proceed via the highly conductive space charge regions for increasing doping concentrations as depicted in Figure 4.33 (a) and (b). For $1.6\ \mathrm{mol\%}$ no electrical anisotropy was measured. This can perhaps be attributed to the fact that the filaments are quite short for this doping concentration and distances between the filaments are similar in both transport directions. With increasing doping concentration it can also be expected, that at a certain doping concentration, the density and number of filaments becomes so high that conduction paths can be formed by overlapping of space charge regions of neighboring filaments (see Figure 4.33 (b)). Electron transport on MoO_3 filaments can only occur when continuous MoO_3 paths are present. This can be expected for high doping concentrations (see Figure 4.33 (c)). However, also then hole transport can proceed via CBP, as long as the amount of MoO_3 is still so low that continuous CBP paths exist.

Considering charge transport for very high doping concentrations, it was found for other material systems, that a high doping concentration can hinder charge transport. A decrease of conductivity for doping concentrations exceeding a certain threshold level was, for example, reported for α-NPD doped with F_4-TCNQ[143], for TCTA doped with WO_3[56] and also for Alq_3 n-doped with LiF[144]. However, none of these studies covered the whole range of possible doping concentrations and no further investigations were carried out at higher doping concentration than the threshold value. Doping MoO_3 into another matrix, i.e. α-NPD, led to the observation that high doping concentrations of up to 50%[7] do

[7] Since many authors do not indicate whether they specify doping concentrations in mol% or in vol% this information can also not be given here.

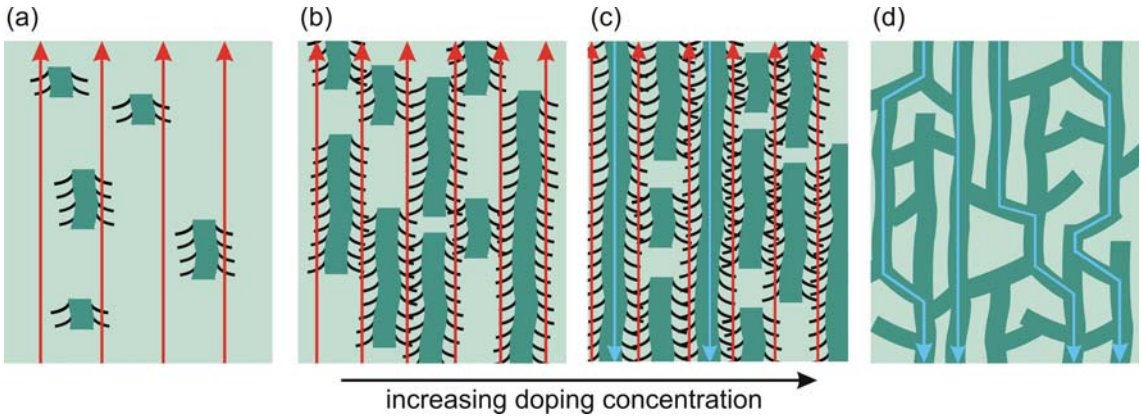

Figure 4.33: Model for conduction along to the MoO_3 filaments in dependence of the doping concentration. Conduction paths of holes are denoted as red arrows and blue arrows are used for electrons.
(a) For short filaments only a small part of the hole conduction can proceed via the dopant/matrix interface area where highly conductive space charge regions are present.
(b) For increasing filament length, a higher fraction of the hole transport is channeled via the highly conductive space charge regions around the filaments. From a certain filament density on, overlap of the space charge regions can occur which can lead to continuous low-resistance conduction paths for holes.
(c) For even higher doping concentrations continuous MoO_3 filaments occur which extend through the whole film thickness and also electron conduction on MoO_3 can take place.
(d) A MoO_3 network is formed for very high doping concentrations, where no continuous conduction paths on CBP are available anymore. Instead, charge transport takes place via electron transport on MoO_3. To provide a better overview, space charge regions are omitted in this subfigure.

not hinder charge transport[32]. Also polymers were studied as matrices. In Ref. [145] P3HT, PFB, TFB and F8BT were doped with F_4-TCNQ. A saturation for doping concentrations in the order of $10\ \mathrm{w/w}$ (dopant to polymer weight ratio) was found, but very high concentrations were not considered in the measurements. Only for P3HT doped with F_4-TCNQ high doping concentrations up to about $85\ \mathrm{mol\%}$ were studied[146]. Similar to the CBP:MoO_3 system, a steep increase of conductivity was found for increasing doping concentrations. However, for very high doping concentrations a strong decrease of conductivity was observed in this case.

With the assumption that current transport always takes place in the organic matrix, one would also expect a drop in conductivity for high MoO_3 concentrations, since at a certain MoO_3 concentration, no continuous CBP paths should be present anymore. However, for MoO_3-doped CBP films it was found that the conductivity saturates towards the value of the dopant for both current directions (see section 4.3.1). This leads to the conclusion that for high doping concentrations the amount of dopants is so high that no continuous CBP paths are present anymore but electron transport via highly conductive MoO_3 can take place (see Figure 4.33 (d)). Also from XPS measurements the presence of a MoO_3 network could be deduced (see section 4.1.3).

The model presented above can also be correlated to the activation energies, determined in section 4.3.2. In the case of current transport along the filaments, high activation energies were found for low doping concentrations, whereas they decreased for higher doping concentrations towards the value of pristine MoO_3. Since for finger and stripe structures different values were found for the activation energies, also the activation energies seem to be correlated with the nanofilament topology. As already pointed out in section 2.3.4, doping leads to filling of traps, which causes the Fermi level to move towards the transport energy and thus leads to a decrease of the activation energy. It can be expected that not only the conductivity is a local quantity, but also the activation energy and that the amount of trap filling is higher at the interface due to the increased charge carrier density in this region. That high activation energies were found for low MoO_3 concentrations, might be connected to the fact that transport mainly proceeds via regions of neat CBP which has a high activation energy, whereas for higher doping concentrations a higher fraction of the conduction path can proceed via the space charge regions, which exhibit lower activation energies. Because the activation energies saturate towards the value for MoO_3 it can also

be inferred from these measurements that conduction in CBP:MoO_3 films transitions into current transport on MoO_3 for higher doping concentrations.
Higher activation energy values were found for current transport perpendicular to the filaments than parallel to it for the investigated doping concentrations (see section 4.3.2). This can perhaps be explained by the fact that for current transport perpendicular to the filaments no favored paths via highly conductive space charge regions, which exhibit low activation energies, are present for the largest fraction of the transport path, which leads to lower conductivities and higher activation energies for charge transport perpendicular to the filaments. For current transport perpendicular to the filaments and doping concentrations from 0.6 vol% to 5 vol%, it was found that the conductivities stayed almost constant for low doping concentrations and the increase in filament number does not seem to have a significant impact on the charge transport. It can therefore be expected that the distance between the filaments is so high that current transport mainly takes place through neat CBP so that the increase in filament density does not have a significant influence on the charge transport (see Figure 4.34 (a) and (b)). For higher doping concentrations, the conductivity also increases and then saturates towards the values of neat MoO_3. Since the formation of a MoO_3 network is expected to also occur in the current direction perpendicular to the current transport, also here the charge transport seems to change from hole transport on CBP for low doping concentrations to electron transport on MoO_3 for high doping concentrations (Figure 4.34 (d)). Also here it is supposable that low-resistance paths form as soon as the MoO_3 filaments are in close vicinity to each other so that overlap of the space-charge region leads to an increase in conductivity (Figure 4.34 (c)).
The above presented model can also explain why the cooled device, with interrupted MoO_3 filaments, has a much lower conductivity than the room temperature one, which exhibited longer filaments, but less transferred charges. For the room temperature sample longer filaments are present, so that charge transport can mainly proceed via highly conductive paths along the MoO_3 filaments (Figure 4.35 (a)). The device with the active layer deposited onto a cooled substrate exhibits shorter filament fragments, than the one which was only deposited at room temperature. Therefore, a higher fraction of the conduction path consists of high-resistance CBP (Figure 4.35 (b)).

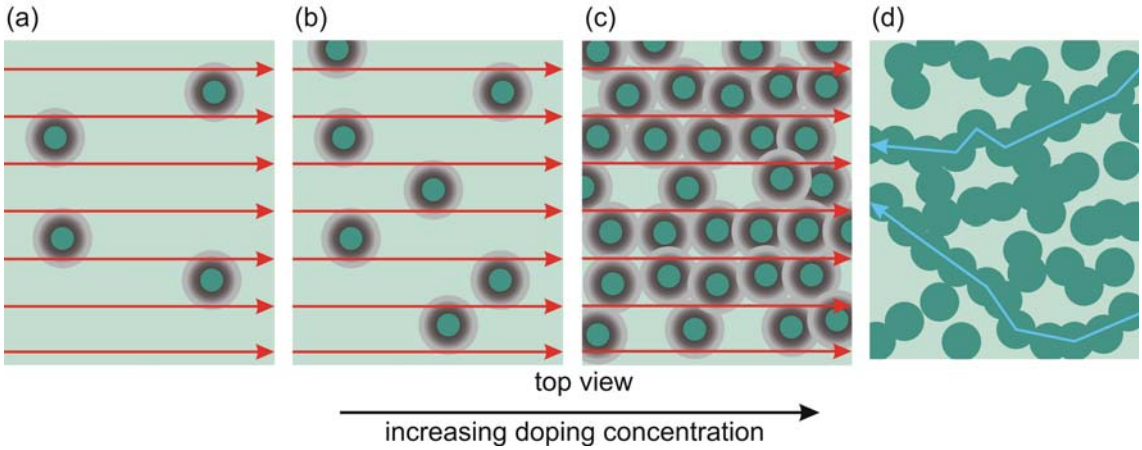

Figure 4.34: Model for conduction perpendicular to the MoO_3 filaments in dependence of the doping concentration in top view.
(a) and (b) For low doping concentrations an increase in filament number has no significant impact on the charge transport, due to the fact that current transport mainly takes place through neat CBP so that the increase in filament density does not have a significant influence on the conductivity.
(c) For higher doping concentrations also overlap of space-charge regions might occur so that continuous conduction paths through highly conductive space charge regions exist.
(d) For very high doping concentrations current transport takes place via electron transport on MoO_3, since no continuous CBP paths are present for hole conduction. To provide a better overview, space charge regions are omitted in this subfigure.

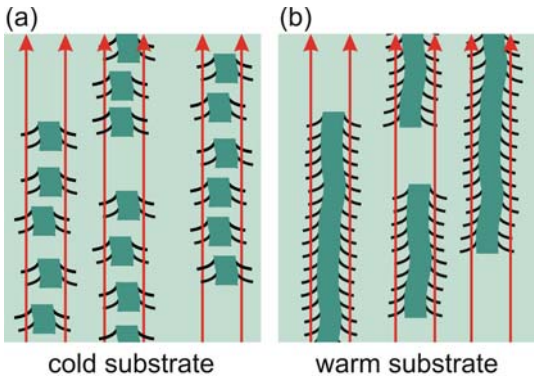

Figure 4.35: Schematic illustration of charge transport in doped films with a different topology.
(a) Only a small part of the hole conduction can take place at the highly conductive space charge regions of the CBP/MoO_3 interface when short MoO_3 fragments exist.
(b) For longer filaments a bigger part of the hole conduction can proceed along the space charge regions.

5 Angle Dependence of LiF/TPBi Interface

Effusion cells in evaporation chambers are usually mounted in such a way that the molecular beam impinges almost perpendicular onto the substrate. Since for devices like OLEDs, several layers consisting of different materials are required, normally evaporation cells are mounted at a certain angle to be able to install a multitude of materials in one chamber. Because the geometry of different chambers have varying deposition angles, the question arises, if angular dependent effects occur, which might influence the device performance. In the present chapter the influence of the deposition angle on the performance of OLEDs, particularly on the energetic properties at the cathode/organic interface, is investigated. However, this was not the initial question the presented measurement series was designed for. The original goal of this project was fabrication of OLEDs onto AFM cantilevers with an enhanced light output at the cantilever tip to allow for a scanning near-field microscopy (SNOM) setup[147]. Most of the results presented in this chapter were developed within the framework of the diploma thesis of B. Martini[97]. XPS measurements were conducted in close collaboration with E. Mankel (TU Darmstadt).

5.1 Performance of OLEDs with Different Deposition Angles

The OLED stack used for this study was based on the stack introduced in section 2.6.2. The deposition sequence was ITO-glass : MoO_3 (10 nm) : TCTA (50 nm) : TPBi:Ir(ppy)$_3$ (20 nm, 7 vol% Ir(ppy)$_3$) : TPBi (30 nm) : LiF (2 nm) : Alu (100 nm). For deposition, OLED substrates were mounted at angles of $0°$, $42°$ and $72°$[1] relative to the incident beam. The deposition geometry is depicted in Figure 5.1. The OLEDs with $0°$ deposition angle were fabricated as normal with shadow masks fixed with screws. For the tilted devices, a metal block with filed lateral surfaces, providing angles of $42°$ and $72°$, was screwed

[1] Since the cantilevers used for the initial project of depositing OLEDs onto AFM cantilevers had pyramid angles of $42°$ and $72°$ these values were also chosen for the tilted OLEDs[97,148].

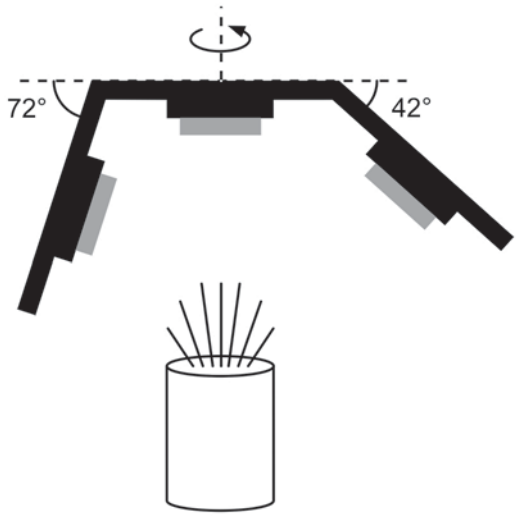

Figure 5.1: Schematic overview on the geometry for tilted OLEDs.

onto the sample holder[2]. The OLED substrates were then fixed onto the metal block by conductive double-sided adhesive carbon tape, which is suitable for vacuum applications, and shadow masks were fixed with kapton tape.

Variation of the deposition angle influences the film thickness so that higher deposition angles lead to thinner layers[147]. Therefore, the influence of the LiF layer thickness, as well as the thickness of the organic layers, was examined first.

In a first step, OLEDs at $0°$ deposition angle were fabricated with different LiF thicknesses which were varied from $2\ \mathrm{nm}$ to $12\ \mathrm{nm}$. The LIV characteristics of these devices are displayed in Figure 5.2. Since LiF has isolating properties[149], it would be expected that for high LiF thicknesses the devices fail to work. However, this was not the case for the examined LiF thicknesses. For thicknesses from $2\ \mathrm{nm}$ to $8\ \mathrm{nm}$ an increase in LiF thickness only led to a slight decrease in luminance as well as in current density and onset voltages were almost constant for these devices. Only the device with $12\ \mathrm{nm}$ LiF thickness showed a significant higher onset voltage of about $8\ \mathrm{V}$ (not shown here).

In a second measurement series, the LiF thickness was kept constant ($8\ \mathrm{nm}$) and the thickness of the organic layer was varied. The term "organic layer" describes the layer sequence TCTA : TPBI:$Ir(ppy)_3$: TPBi.

Two OLEDs were prepared at a deposition angle of $0°$ with organic layer thicknesses of

[2]Since the metal block was filed by hand the accuracy of the angle amounts to about $\pm\ 2°$ [97].

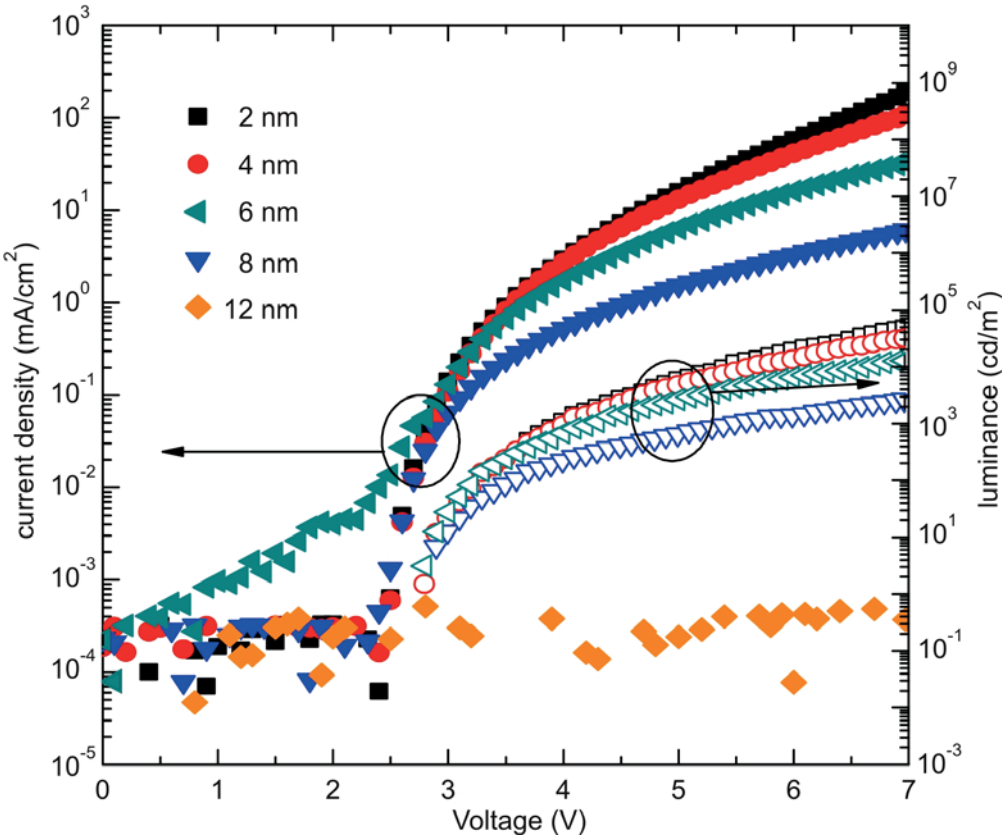

Figure 5.2: LIV characteristics of OLEDs with different thicknesses of the LiF injection layers.

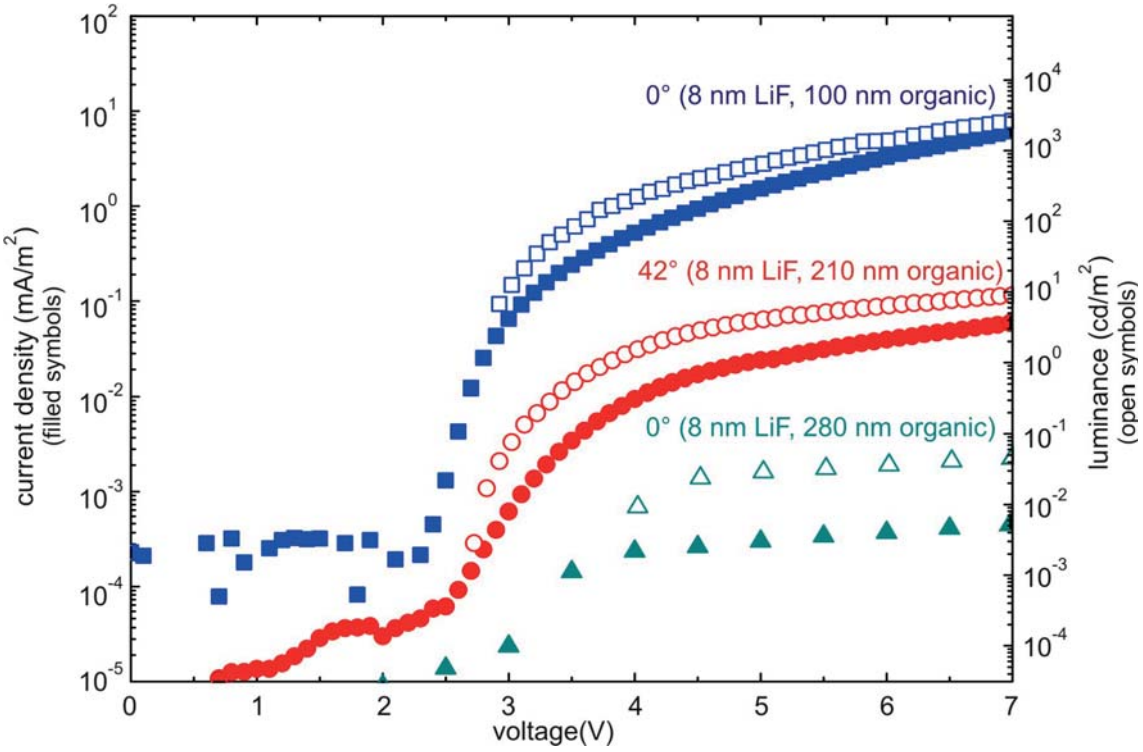

Figure 5.3: LIV characteristics of OLEDs, where the thicknesses of the organic layers and the deposition angles were varied.

100 nm and 280 nm. As can be seen in Figure 5.3, current density and luminance significantly drop by about five orders of magnitude when the thickness is increased from 100 nm to 280 nm. A decrease in current density for higher film thicknesses is expected since, according to Child's law (see equation (2.4.3)), an increased film thickness d leads to a decreased injection current density j for a space charge limited current.

Additionally, the electro-optical characteristic of a device with an about 210 nm thick organic layer[3], which was deposited at an evaporation angle of 42° is depicted in Figure 5.3. This device shows higher current and light output than the device with 280 nm (0°) but worse characteristics than for 100 nm (0°) organic layer thickness. From these results it can be concluded that the thinner the organic layer, the better the device characteristics. Nevertheless, it will be shown below, that also other aspects might play a role, which in-

[3]The values of the devices with 0° deposition values were determined by oscillating crystals. The thicknesses for the tilted devices were derived from profilometer measurements of 100 nm thick layers of the single materials.

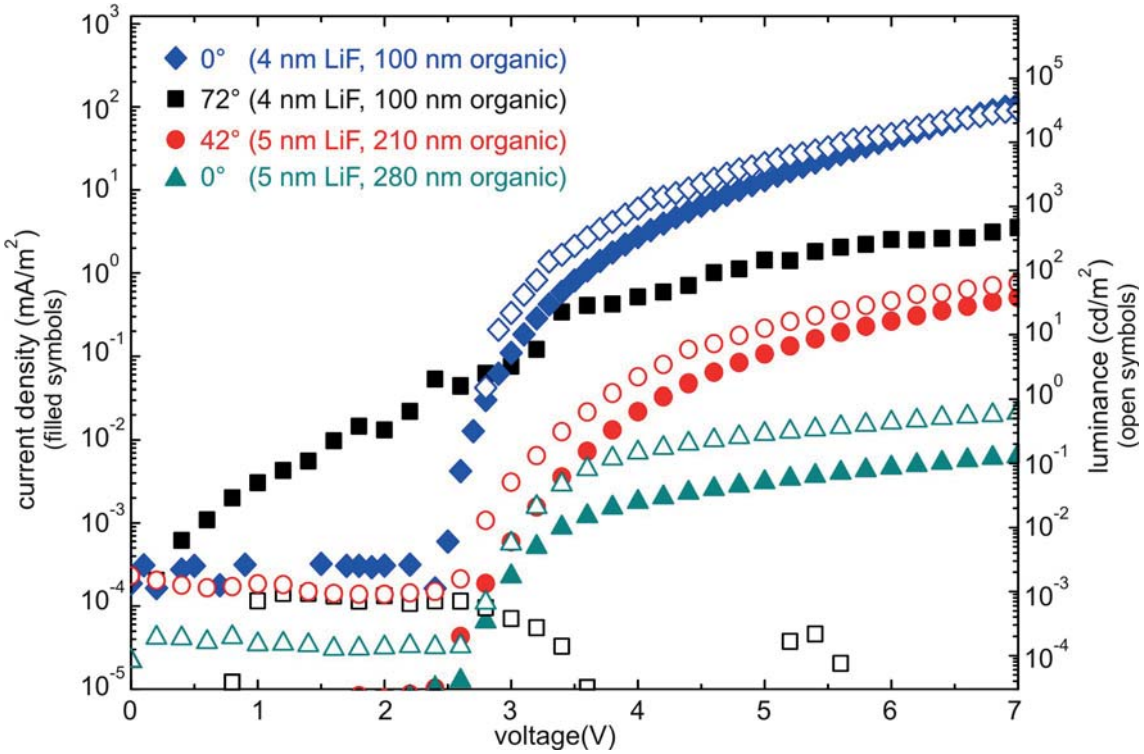

Figure 5.4: LIV characteristics of OLEDs, where the organic layers were grown at different deposition angles.

fluence the electro-optical characteristics of devices deposited at different angles and the interpretation of these results does not need to be as straight-forward as it seems to be on the first sight.

In a third step, the deposition angle was varied systematically. Figure 5.4 shows the LIV characteristics for three OLEDs deposited at $0°$, $42°$ and $72°$. The nominal thickness measured by the quartz microbalance was $280\ \mathrm{nm}$. This led to thicknesses of about $280\ \mathrm{nm}$, $210\ \mathrm{nm}$ and $100\ \mathrm{nm}$ for the organic layer and about $5\ \mathrm{nm}$, $5\ \mathrm{nm}$ and $4\ \mathrm{nm}$ for the LiF layers for $0°$, $42°$ and $72°$, respectively. Additionally, the characteristic for a device evaporated at $0°$ with a thickness of $100\ \mathrm{nm}$ for the organic layer and $4\ \mathrm{nm}$ for the LiF layer is depicted. It was shown above that reducing the organic layer thickness from $280\ \mathrm{nm}$ to $100\ \mathrm{nm}$ improves the LIV characteristics. The same effect was also observed for a reduction of the LiF thickness from $8\ \mathrm{nm}$ to $2\ \mathrm{nm}$, but only with a minor influence. Considering the OLED deposited at $0°$ with $280\ \mathrm{nm}$ organic layer thickness and the device fabricated

at $42°$ with an $210\ \mathrm{nm}$ thick organic layer, it could be seen that the electro-optical characteristics improved with higher deposition angle. This can be expected since the device evaporated at $0°$ had a higher organic layer thickness. Also that the OLED with $100\ \mathrm{nm}$ organic layer thickness, which was deposited at $0°$, shows even better performance is consistent with the results presented above, because it has an even lower layer thickness and additionally a slightly lower LiF thickness.
Since the OLED fabricated at $72°$ also exhibits an organic layer thickness of $100\ \mathrm{nm}$ and also the lowest LiF thickness of $4\ \mathrm{nm}$, it would be expected that this device possesses a similar performance as the device with $100\ \mathrm{nm}$, which was deposited at $0°$. However, no turn-on voltage can be identified, as it would be expected for a diode with a pn-junction and already at low voltages a significant current density can be measured. Therefore, the IV characteristics indicates that this OLED behaves like a single-carrier device. Additionally, the luminance output lies below the detection limit of about $<10^{-4}\ \mathrm{cd/m^2}$. This indicates that not only the layer thickness influences the device performance in this case, but there must be other factors to be taken into account. The unipolar behavior implies that charge injection from one of the two contacts is not sufficient.
Regarding the anode contact, the thickness of the MoO_3 injection layer should not have a major impact on the performance of the devices. In section 2.5.1 a model for charge injection with MoO_3 injection layers was presented. Since no chemical reaction is involved and due to the fact that the conductivity of MoO_3 is quite high (see section 4.3.1) it seems to be unlikely that hole injection is influenced by the deposition angle. Besides, it was found that even when up to $50\ \mathrm{nm}$ thick MoO_3 layers are applied for organic solar cells, devices are still working[80,150].
However, the process leading to a working organic/LiF/aluminum contact is still not understood in detail (see section 2.5.2). Therefore, it could be supposed that the reason for the failure of the OLED evaporated at $72°$ is due to energetic issues at this interface.

5.2 Investigation of the TPBi/LiF Interface using XPS

To investigate the influence of the deposition angle on the energetic conditions at the cathode contact, XPS measurements were performed. The XPS results shown in this section were conducted by E. Mankel from the TU Darmstadt.

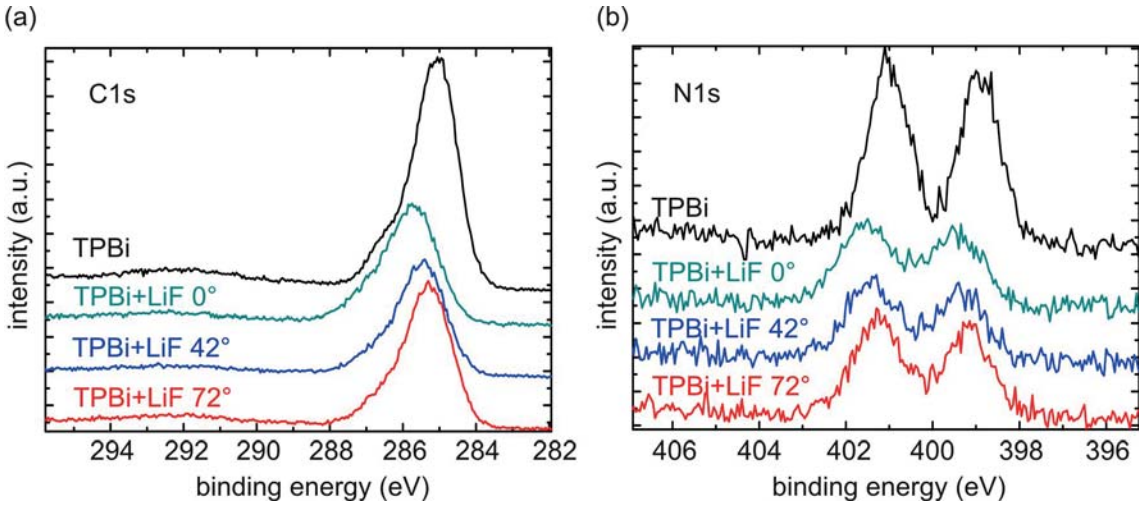

Figure 5.5: (a) C1s and (b) N1s emission lines of TPBi obtained from XPS measurements. A neat TPBi sample, as well as specimens where a thin layer of LiF was evaporated at different deposition angles of $0°$, $42°$ and $72°$ were measured.

For these measurements, the TPBi/LiF cathode contact was grown on ITO-glass. In the first step, $30\ \mathrm{nm}$ TPBi was deposited simultaneously onto four substrates at a tilt angle of $0°$, to eliminate effects due to different sample thicknesses and deposition angles. Afterwards, all samples were transferred directly from the UHV into the inert atmosphere of the glovebox, which is attached to the clustertool (see section 3.1), to ensure comparable environmental conditions. Then samples were mounted onto their respective sample holders for deposition at different angles. In the last preparation step, a thin LiF layer was evaporated onto each individual substrate. In Figures 5.5 (a) and (b) the C1s and the N1s peaks of TPBi are depicted for all samples. The exact layer thicknesses of LiF was determined from XPS by measuring the substrate peak damping. The mean free electron path was calculated with the computer program NIST Electron Inelastic-Mean-Free-Path Database, which applies equations from Ref. [151]. The measured LiF thicknesses were calculated using equation (3.2.4) and amounted to $1.5\ \mathrm{nm}$, $1.9\ \mathrm{nm}$ and $1.2\ \mathrm{nm}$ for $0°$, $42°$ and $72°$, respectively. The N1s peak revealed a characteristic double structure. This is due to a chemical shift, since different binding partners of nitrogen in the TPBi molecule lead to different oxidation states and therefore to different binding energies. Also the C1s peak exhibits a double structure, since carbon atoms in TPBi are bound to nitrogen atoms,

but also to other carbon and hydrogen atoms[4]. To determine the peak energies, two voigt-functions (see section 3.2.2.1) were fitted to each measured spectrum, to account for the chemical shift. For the fits, the difference between the two components was kept constant as well as their relative intensities, which can be calculated by counting the number of the respective binding partners. The peak position energy of the component with the highest binding energy is indicated in the following.

Because the shape of the N1s and C1s peaks did not change upon deposition of LiF, it can be concluded that no chemical reaction took place. It can be inferred from the experiments, that the full width at half maximum increases upon deposition of LiF. This directs towards an increased energetic disorder upon doping, as it is also expected from theory (see section 2.3.4). The observed peak broadening of the core levels implies that also broadening of the LUMO DOS occurred. However, since no significant angle dependence was found, this effect cannot explain why the device, where the organic layer was grown at $72°$, failed to work.

Comparing the samples deposited at $0°$ with and without the LiF layer, it can be observed that the C1s and N1s peak of TPBi shift by almost the same amount of $0.64\ \mathrm{eV}$ respectively $0.57\ \mathrm{eV}$ to higher binding energies, when the LiF layer is deposited on top of the organic layer. This directs towards an energetic interaction between TPBi and LiF takes place and implies that the Fermi energy of TPBi shifts towards the LUMO upon deposition of LiF, indicating n-doping of the organic layer. In Ref. [90] a similar value for the Fermi level shift was found for depositing at least about $2.5\ \mathrm{nm}$ LiF onto Alq_3. The sample with the LiF layer, which was evaporated at $42°$, also shows a shift to higher binding energies, compared to pure TPBi, but in this case the shift only amounts to $0.37\ \mathrm{eV}$ (C1s) and $0.43\ \mathrm{eV}$ (N1s) in comparison with the pure TPBi layer. For the sample with the LiF layer evaporated at $72°$ an even smaller shift in binding energy was observed leading to a Fermi level shift of only $0.21\ \mathrm{eV}$ (C1s) respectively $0.26\ \mathrm{eV}$ (N1s) compared to TPBi without LiF coverage. In summary, for all deposition angles a shift of the C1s and N1s peaks to higher binding energies can be observed, but the value of this shift decreases with increasing deposition angle. The LiF thickness might influence the Fermi level shift. Be-

[4]The peak position difference for carbon atoms bound to hydrogen and to other carbon atoms cannot be resolved with the measurement setup used here.

cause the intermediate angle of $42°$ exhibits the highest thickness, the trend in the Fermi level shift is not a LiF thickness dependent effect.
Since the OLED deposited at $72°$ does not show typical OLED characteristics it is suggested that the change in the observed Fermi level shift is crucial for the functionality of the OLED device. The results indicate, that the interaction process, taking place at the interface, becomes weaker with increasing deposition angle, so that at $72°$ only a minor interaction takes place, which leads to weaker n-type doping causing a lower conductivity and also worse injection properties at the contact due to a higher injection barrier.
An explanation might be that the interaction process of TPBi and LiF is due to diffusion of Li or F into the electron transport layer. Since with increasing deposition angle the impulse component perpendicular to the substrate decreases, the penetration depth of LiF into TPBi might also decrease. Then, higher deposition angles would lead to less diffusion into the organic layer which might decrease the number of dopants and consequentially the amount of doping. Therefore, for OLEDs deposited at $72°$ only a negligible amount of injection barrier lowering occurs so that no electrons can be injected through the cathode, but only holes via the anode. Hence, the IV characteristics becomes unipolar and the device cannot emit light.
Another explanation might be a different growth behavior for varied deposition angles. For a variety of different materials, e.g. MgF_2 [152], CaF_2, Cr, Ti [153] or silicon [154], the so-called glancing angle deposition (GLAD) was applied. There, shadowing effects lead to sculptured thin films, whose morphology can be influenced by the deposition angle, the rotation speed during evaporation and the substrate temperature. Such effects might also occur for LiF and provide an explanation for the failure of the OLED evaporated onto a tilted substrate with a tilt angle of $72°$.
It can be supposed that the observed Fermi level shift leads to a higher injection barrier of $0.6\ \mathrm{eV}$ into the aluminum for $0°$ deposition angle compared to $72°$. So far, the influence of aluminum deposition was not investigated but might, according to Ref. [91], also play an important role for the contact formation at the TPBi/LiF/aluminum interface.

6 Conclusion

In the first part of this chapter all experimental findings of this thesis are summarized. The second part gives an outlook on possible future work.

6.1 Summary

Electrochemically doped organic layers are commonly applied in organic state-of-the-art devices like organic light emitting diodes or organic solar cells, to significantly enhance their efficiency. However, a comprehensive understanding of the doping process in organic semiconductors is still missing. For instance, it is not understood why very high doping concentrations of several volume per cent are needed, whereas for inorganic semiconductors doping concentrations in the range of ppm are sufficient to obtain a significant rise of conductivity. This question is related to the observation that very low doping efficiencies of only a few per cent were found for a variety of different material systems, both organic:organic and organic:inorganic composites. In this work, various measurement techniques were applied to obtain information about structural, electronic and electrical properties of doped organic thin films with the objective to improve the understanding of fundamental processes taking place in such composites. As material system the organic semiconductor CBP doped with the transition metal oxide MoO_3 was used.
In the first step, the structural properties of the co-evaporated thin films were studied using different TEM measurement techniques. Dark spots were found in the bright-field images of doped films. Using TEM spectroscopy in the low loss and in the core loss regime, it could be proven that these dark spots consist of MoO_3, thus confirming that the dopant MoO_3 agglomerates within the organic matrix CBP. Three-dimensional information was obtained using electron tomography. These measurement revealed that MoO_3 filaments, preferentially oriented perpendicular to the substrate, occur in the doped films. Furthermore, the influence of the substrate temperature on the topology was examined and it was found that by cooling down the substrate during film deposition the filament length

decreases, while its filament diameter stays the same, compared to film deposition onto a substrate at room temperature. Based on these observations, a description of the MoO_3 filament growth was developed.

Since the dopant topology was found to be anisotropic, the question arised whether this structural anisotropy is related to an electrical anisotropy. Therefore, electrical measurements of hole only devices, consisting of CBP with different MoO_3 concentrations, were conducted. Two different device structures were fabricated which allowed for investigation of the electronic properties along the MoO_3 filaments and perpendicular to them. Conductivity as well as activation energy values were found to depend on the current direction.

The results of the structural and electrical investigations were combined with results on electronic properties inferred from photoelectron spectroscopy and FTIR spectroscopy measurements. Based on all results, a model for charge transport in CBP:MoO_3 composites was developed. From XPS measurements it could be inferred that CBP cations and MoO_3 anions are located close to the interface and that a space charge region is present at the organic/dopant interface. Therefore, it was proposed that charge transport preferentially occurs at the CBP/MoO_3 interface and space charge regions serve as favored paths for hole conduction. Charge transport for composites with filaments which do not extend through the whole film thickness can then be explained by a series connection of highly-resistive paths of pure CBP and low-resistive conduction paths through the space charge regions. Since for high doping concentrations conductivities and activation energies saturated towards the value for neat MoO_3 films, it was concluded that for high doping concentrations a transition from hole conduction on CBP to electron conduction on MoO_3 takes place.

In the last part of this work, n-type doping was investigated by fabricating OLEDs where the dopant LiF was incorporated as thin film between the electron conductor TPBi and the cathode, consisting of aluminum. It was found that the thickness of the LiF layer does not significantly influence the device performance of OLEDs when it is varied from $2\ \mathrm{nm}$ to $8\ \mathrm{nm}$. Furthermore, the influence of the deposition angle on the device performance of OLEDs was investigated. Compared to the OLEDs which were fabricated at $0°$ and $42°$ deposition angle, the OLED which was deposited at $72°$ did not emit light and IV characteristics which are typical for a single-carrier device were found. The latter indi-

cated that charge injection from one of the two contacts was not sufficient. Therefore, the LiF/TPBi interface was investigated using XPS and a decreasing Fermi level shift towards the LUMO of TPBi was found for increasing deposition angle, compared to pristine TPBi. This directs towards a weaker amount of n-type doping for increasing deposition angle.

6.2 Outlook

Since a large variety of measurement techniques could be applied due to the very fruitful cooperations at Innovationlab in Heidelberg, a good step forward was made in understanding the fundamentals of doping in organic semiconductors. However, there are still unresolved issues. Since XPS could only indirectly give insight into the topology of the doped films, it would be helpful to conduct electron tomography measurements for additional doping concentrations. Electron tomography, as it was conducted here, is a very time-consuming method. Therefore, it would be helpful to establish either the possibility of automated tilt series acquisition or the application of reconstruction algorithms, which require the acquisition of a smaller number of images, like DART[135]. The latter would also have the advantage that beam damage would be reduced. Since it was shown that the thickness is affected by the floating process, which is commonly applied to prepare TEM samples, other preparation techniques like microtome slices[155] or preparation of TEM lamellae[156] would be favorable. Besides, there is still the unresolved question why there exists a discrepancy between the amount of incorporated dopants and the amount of dopants which can be detected by TEM. One explanation would be that some of the MoO_3 dopants are homogeneously dispersed in the CBP matrix or present as clusters which are so small that they cannot be detected with TEM. To resolve this issue, EEL spectra could be acquired where only an area without the visible MoO_3 agglomerations is analyzed, which can be compared to EEL spectra of an area which contains agglomerations. However, this would require a suitable measurement setup, for example nanobeam[157] or scanning transmission electron microscopy (STEM)[134], which was not available during the presented thesis.

Regarding the electrical properties, it would be interesting to obtain separated information about the physical quantities which determine the conductivity, namely charge carrier density and mobility, in dependence of the doping concentrations. Charge carrier densities

could, for example, be obtained from CV measurements[38] or Kelvin Probe analysis[37]. Mobility values can be derived from C-f[158], time-of-flight (TOF)[159,160] or CELIV[1] measurements[161,162]. To confirm the proposed model, it is of great interest to determine the majority carrier species for different doping concentrations. For inorganic semiconductors this is commonly done with Hall effect measurements. However, for organic materials, successful Hall effect results were so far only obtained for highly crystalline materials[163]. Besides, more experiments of cooled samples would be helpful, to obtain a deeper understanding on how the choice of the substrate temperature influences the topology and the charge transport. A cryostat which can be incorporated into organic chamber 1 or 2 of the clustertool will therefore be installed soon.

Furthermore, it would be interesting to conduct similar studies as presented in this thesis for other material systems and find out, if conclusions drawn for CBP:MoO_3 are valid in general or specific for this material system. From the measurements, which were conducted on different organic matrices doped with MoO_3, very similar results were obtained. For α-NPD and TCTA doped with MoO_3 a similar behavior was found regarding the electrical properties, i.e. the conductivity saturates towards the value of neat MoO_3 for high doping concentrations in the case of charge transport perpendicular to the substrate[139]. For α-NPD doped with MoO_3 also agglomeration could be detected, however, no tomography was applied. Therefore, it can be expected so far, that, regarding topography and charge transport, no severe changes occur upon choosing a different matrix material.

For many doped systems a decrease in conductivity was found for high doping concentrations. One explanation would be, that, other than for MoO_3 in CBP, no filaments form, but the dopants are more or less homogeneously dispersed in the matrix, so that at higher doping concentrations they serve as scattering centers and hinder charge transport. Mayer et al. found clustering of WO_3 in CuPc and concluded from the fact that WO_3:CuPc and F_4-TCNQ:CuPc composites behaved similarly, regarding the electronic properties, that also F_4-TCNQ agglomerates within CuPc. However, no clear evidence was found for clustering of small molecules in organic matrices so far. For example, Ha et al. found evidence from STM measurements for clustering of MoO_3 evaporated onto pentacene[129], but not for F_4-TCNQ on pentacene[164]. Lee et al. acquired HAADF images of α-NPD films doped with F_4-TCNQ and $Mo(tfd)_3$ and also found no evidence for clustering of

[1] carrier extraction by linearly increasing voltage

these small molecule dopants[35]. That clustering of TMOs was found, but no agglomeration could be detected for organic dopants does not mandatorily imply that organic dopants do not agglomerate. Instead, it can be expected that a better contrast is obtained for TMO:organic composites than for organic:organic mixtures and it can also be expected that the critical cluster size of organic dopants would be smaller, since organic materials exhibit smaller surface energies than inorganic species.

Beside the question about the fundamental properties, it might also be interesting to think about future concepts for doping and the question arises which kind of dopant might be the most favorable one. Organic dopants can be quite volatile[57], whereas large dopants like TMOs are also expected to be more stable, since they cannot move as easily in the organic matrix[24,165]. This was, for instance, shown in Ref. [67] where in pure CuPc films, which were evaporated in the same evaporation chamber as WO_3, the Fermi level was almost located in the middle of the band gap. However, when neat CuPc was evaporated in the same deposition chamber as F_4-TCNQ, the Fermi level of CuPc was found to be shifted towards the HOMO, indicating p-type doping by the volatile dopant.

On first sight one would expect that agglomeration of the dopants is a negative behavior, since it reduces the doping efficiency and organic dopants might therefore be advantageous. However, it was shown in this thesis that agglomerations can provide favored pathways for charge conduction, instead of hindering charge transport. Therefore, agglomeration might even be an advantage regarding charge transport. Designing new molecules, which tend to cluster in the right way, might be a promising concept for the future. An approach to enhance the doping efficiency might be to design molecules where the overlap of the molecular orbitals is reduced. This would cause less energy level splitting upon hybridization and therefore enhance the number of free charge carriers.

The insights gained for electrochemically doped organic layers might also be helpful for the design of dyes, used in the emission zone of OLEDs. Dyes are also commonly applied via co-evaporation and similar effects, regarding topology and charge transport, might occur for electrochemically and dye-doped thin films.

To conclude, enormous progress has been made in understanding the doping process in organic semiconductors due to the collaborative environment at Innovationlab. However, there are still a multitude of open questions and interesting experimental and theoretical results can be expected to be discovered in the future.

A Molecular Structures

For better readability only the common abbreveations were used throughout the thesis. This chapter provides the correct chemical formulae for all organic semiconductors which are mentioned throughout the text, as well as the molecular structures for all organic semiconductors used in this work.

1-TNATA:	4,40,400-tris(N-(1-naphthyl)-N-phenylamino)triphenylamine
2-TNATA:	4,4',4"-tris(N-(2-naphthyl)-N-phenylamino)-triphenylamine
α-NPD	1,4-bis[N-(1-naphthyl)-N'-phenylamino]-4,4' diamine
Alq_3:	8-quinolinolato) aluminum
CBP:	4,4'-Bis(N-carbazolyl)-1,1'-biphenyl
$CoCp_2$	bis(cyclopentadienyl)-cobalt(II)
CuPc	copper phthalocyanine
DDQ:	dicyano-dichloroquinone
F_4-TCNQ:	2,3,5,6-tetrafluoro-7,7,8,8-tetracyanoquinodimethane
F8BT	poly(9,9-di-n-octylfluorene-alt-benzothiadiazole)
$Ir(ppy)_3$:	fac tris (2-phenylpyridine) iridium
MEH-PPV:	poly(2-methoxy-5-(2'-ethylhexyloxy)-p-phenylene vinylene)
$Mo(tfd)_3$:	tri[1,2-bis(trifluoromethyl)ethane-1,2-dithiolene]
m-TDATA:	4,4',4"-tris(3-methylphenylphenylamino) triphenylamine
P3HT:	poly(3-hexylthiophene)
PEDOT:PSS:	poly(3,4-ethylenedioxythiophene):poly-(styrenesulfonate)
PFB:	poly(9,9-dioctylfluorene-co-bis-N,N-(4-butylphenyl)-bis-N,N-phenyl-1,4-phenylenediamine)
$[RuCp^*(mes)]_2$:	ruthenium(pentamethylcyclopentadienyl)(1,3,5-trimethylbenzene)
spiro-CBP:	2,7-bis(9-carbazolyl)-9,9-spirobifluorene
TCNQ:	tetracyanoquinodimethane

TCTA:	4,4',4"-Tri(N-carbazolyl)triphenylamine
TFB:	poly(9,9-di-n-octylfluorene-alt-(1,4-phenylene-((4-sec-butylphenyl) imino)-1,4-phenylene)
TPBi:	1,3,5-tris (2-N-phenylbenzimidazolyl) benzene
TTN:	Tetrathianaphthacene
VOPc:	vanadyl-phthalocyanine
ZnPc:	Zinc phthalocyanine

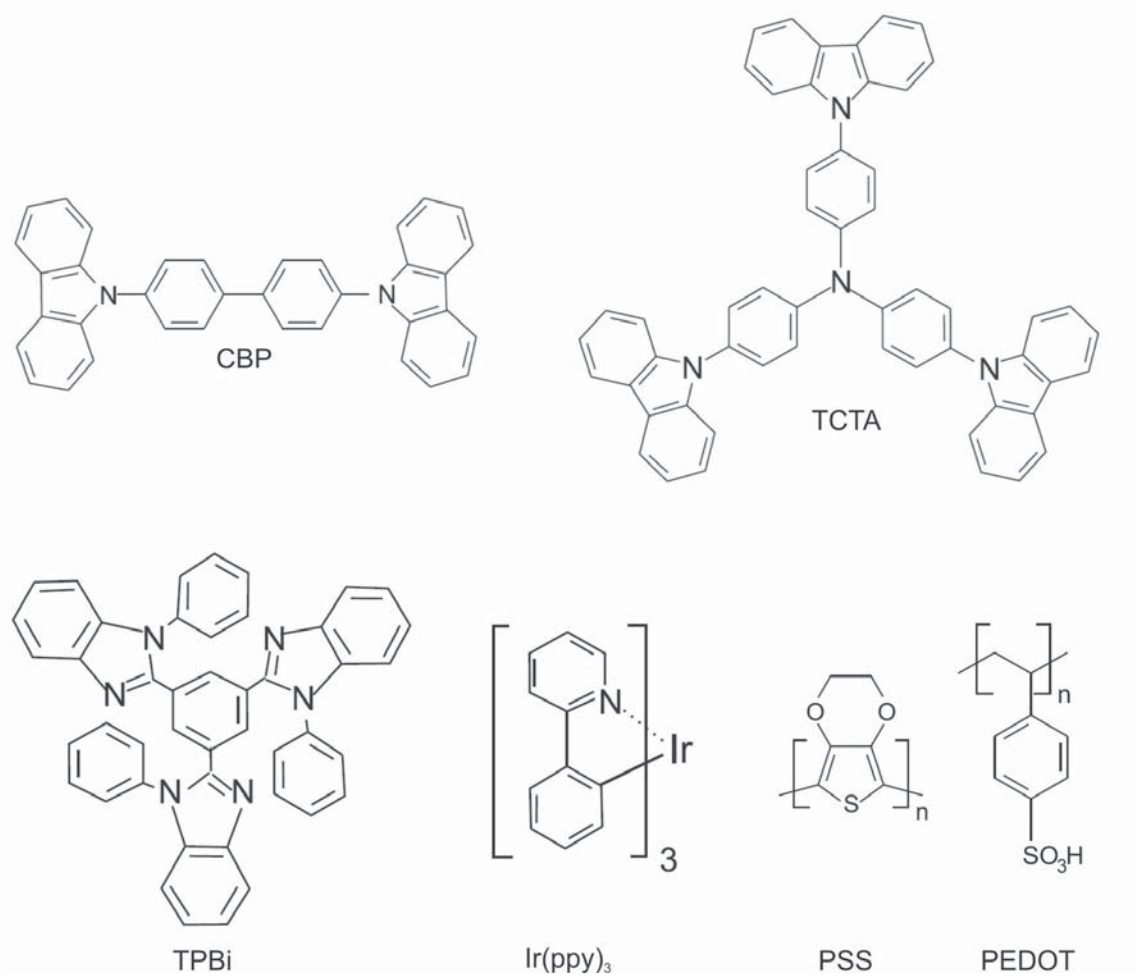

Figure A.1: Molecular structures of all organic materials used in this work.

B Journal Publications and Conference Presentations

Journal Publications

1. Observation of Filamentous Nanostructures in Organic-Inorganic Composite Thin Films Deposited By Co-Evaporation; D. Donhauser, M. Pfannmöller, L. Dieterle, K. Schultheiß, R. R. Schröder, W. Kowalsky, and M. Kröger, Adv. Funct. Mater., 23 (17), 2130 (2013)

2. Infrared study of the MoO_3 doping efficiency in 4,4'-bis(N-carbazolyl)-1,1'-biphenyl (CBP); T. Glaser, S. Beck, B. Lunkenheimer, D. Donhauser, A. Köhn, M. Kröger, and A. Pucci, Org. El., 14 (2), 575 (2012)

Patent

1. Title: Verfahren zur Herstellung eines elektrischen Bauteils, Kodepositionsanlage und elektrisches Bauteil
   Aktenzeichen: 3022-100 DE-1 (not yet accepted)

Conference Presentations

1. Applications and Physics of Transition Metal Oxides for Organic Light Emitting Devices; W. Kowalsky, S. Hamwi, K. Schultheiß, D. Donhauser, and M. Kröger. The 11th International Meeting on Information Display (IMID), Seoul, South Korea (2011)

2. Clustering of MoO_3 doped into organic thin films studied by IR-spectroscopy, AFM and TEM: D. Donhauser, M. Kröger, K. Schultheiß, M. Pfannmöller, R. R. Schröder,

T. Glaser, S. Tengeler, M. Alt, A. Pucci, B. Lunkenheimer, A. Köhn, and W. Kowalsky, U4.10. MRS fall meeting, Boston, USA (2011)

3. Agglomeration of MoO_3 doped into organic thin films studied by TEM-spectroscopy and Tomography: D. Donhauser, K. Schultheiß, L. Dieterle, M. Pfannmöller, R. R. Schröder, T. Glaser, B. Lunkenheimer, M. Kröger, and W. Kowalsky, HL 52.6. DPG Frühjahrstagung, Berlin (2012)

4. IR spectroscopic investigation of the MoO_3 doping efficiency in CBP: T. Glaser, S. Tengeler, S. Beck, D. Donhauser, B. Lunkenheimer, A. Köhn, and A. Pucci, HL 52.5. DPG Frühjahrstagung, Berlin (2012)

5. Toward the realization of a Scanning Near-field Optical Microscope deploying an Organic Light Emitting Device: I. Vladimirov, B. Martini, D. Donhauser, J. Ostermann, M. Kröger, and W. Kowalsky, DPG Frühjahrstagung, Berlin (2012)

6. IR spectroscopy on metal oxide p-doped thin films of organic semiconductors: S. Tengeler, T. Glaser, S. Beck, B. Lunkenheimer, D. Donhauser and A. Pucci, DPG Frühjahrstagung, Berlin (2012)

7. Charge Transport in organic solar cells studied by Scanning Probe Microscopy: M. Scherer, D. Daume, R. Saive, D. Donhauser, M. Kröger, I. Wacker, R. R. Schröder, and W. Kowalsky, DPG Frühjahrstagung, Berlin (2012)

8. IR spectroscopy on metal oxide p-doped thin films of organic semiconductors: S. Tengeler, T. Glaser, S. Beck, B. Lunkenheimer, D. Donhauser, and A. Pucci, DPG Frühjahrstagung, Berlin (2012)

9. Microstructural aspects of transition metal oxide p-type doping of organic semiconductors: L. Dieterle, K. Schultheiß, M. Pfannmöller, D. Donhauser, M. Kröger, R. R. Schröder, and W. Kowalsky, Symposium X. E-MRS, Straßbourg, France (2012)

10. Microstructural aspects of transition metal oxide p-type doping of organic semiconductors: L. Dieterle, K. Schultheiß, M. Pfannmöller, D. Donhauser, M. Kröger, R. R. Schröder, and W. Kowalsky, EMC, Manchester, Great Britain (2012)

11. The impact of MoO_3 agglomeration onto the doping efficiency in p-doped organic thin films for organic light emitting diodes: D. Donhauser, M. Pfannmöller, L. Dieterle, K. Schultheiß, T. Glaser, R. R. Schröder, M. Kröger, and W. Kowalsky. The 12th International Meeting on Information Display, Daegu, South Korea (2012)

12. Structural and Electronic Properties of Co-evaporated Doped Organic Thin Films: D. Donhauser, M. Pfannmöller, L. Dieterle, M. Al-Helwi, T. Glaser, A. Pucci, K. Schultheiß, R. R. Schröder, W. Kowalsky, and M. Kröger, MRS fall meeting, Boston, USA (2012)

13. Correlation of morphology and electronic properties of MoO_3 doped CBP layers I: TEM and electrical properties: D. Donhauser, L. Dieterle, P. Heimel, T. Glaser, M. Kühn, M. Al-Helwi, R. R. Schröder, E. Mankel, M. Kröger, and W. Kowalsky, DPG Frühjahrstagung, Regensburg (2013)

14. Correlation of morphology and electronic properties of MoO_3-doped CBP layers II: IR spectroscopic study: T. Glaser, S. Beck, D. Donhauser, M. Kühn, B. Lunkenheimer, A. Köhn, E. Mankel, and A. Pucci, DPG Frühjahrstagung, Regensburg (2013)

15. Correlation of morphology and electronic properties of MoO_3-doped CBP layers III: XPS and UPS study: M. Kühn, E. Mankel, D. Donhauser, T. Glaser, T. Mayer, and W. Jägermann, DPG Frühjahrstagung, Regensburg (2013)

16. Electrical characterization of selected matrix dopant systems via U-I measurements: M. Gölz, D. Donhauser, E. Mankel, W. Jägermann, and W. Kowalsky, DPG Frühjahrstagung, Regensburg (2013)

17. Effects of p-doping on charge carrier concentration and charge carrier transport in organic-inorganic composite thin layers: C. Leinweber, D. Nanova, D. Donhauser, E. Mankel, W. Kowalsky, U. Lemmer, and N. Mechau, DPG Frühjahrstagung, Regensburg (2013)

18. Morphology and electronic properties of co-evaporated organic-inorganic composites: D. Donhauser, L. Dieterle, M. Pfannmöller, M. Kühn, M. Kröger, E. Mankel,

T. Mayer, R. R. Schröder, W. Jägermann, and W. Kowalsky. ESPMI, Rehovot, Israel (2013)

19. Three dimensional characterization of nanofilamentous growth of transition metal oxide dopants in organic semiconductors: A. K. Kast, D. Donhauser, L. Dieterle, M. Pfannmöller, E. Mankel, R. Lovrinčić, M. Kühn, W. Kowalsky, and R. R. Schröder. MC 2013, Regensburg

20. Correlation between morphology and electrical properties of MoO_3-doped organic thin-films: D. Donhauser, M. Kröger, L. Dieterle, M. Pfannmöller, A. K. Kast, R. R. Schröder, R. Lovrinčić, and W. Kowalsky. JSAP-MRS Joint Symposia, Kyoto, Japan (2013)

Bibliography

[1] A. Bernanose, “Electroluminescence of organic compounds”, *Br. J. Appl. Phys.*, vol. 6, p. 54, 1955.

[2] W. Helfrich and W. G. Schneider, “Recombination Radiation in Anthracene Crystals”, *Phys. Rev. Lett.*, vol. 14, p. 229, 1965.

[3] C. W. Tang and S. A. VanSlyke, “Organic electroluminescent diodes”, *Appl. Phys. Lett.*, vol. 51, no. 12, p. 913, 1987.

[4] T. Sekitani, U. Zschieschang, H. Klauk, and T. Someya, “Flexible organic transistors and circuits with extreme bending stability”, *Nature Mater.*, vol. 9, p. 1015, 2010.

[5] J. Meyer, P. Görrn, S. Hamwi, H.-H. Johannes, T. Riedl, and W. Kowalsky, “Indium-free transparent organic light emitting diodes with Al doped ZnO electrodes grown by atomic layer and pulsed laser deposition”, *Appl. Phys. Lett.*, vol. 93, no. 7, p. 073308, 2008.

[6] Y. H. Kim, J. Lee, S. Hofmann, M. C. Gather, L. Müller-Meskamp, and K. Leo, “Achieving High Efficiency and Improved Stability in ITO-Free Transparent Organic Light-Emitting Diodes with Conductive Polymer Electrodes”, *Adv. Funct. Mater.*, DOI: 10.1002/adfm.201203449, 2013.

[7] J. M. Szarko, J. Guo, Y. Liang, B. Lee, B. S. Rolczynski, J. Strzalka, T. Xu, S. Loser, T. J. Marks, L. Yu, and L. X. Chen, “When Function Follows Form: Effects of Donor Copolymer Side Chains on Film Morphology and BHJ Solar Cell Performance”, *Adv. Mater.*, vol. 22, no. 48, p. 5468, 2010.

[8] K. Walzer, B. Maennig, M. Pfeiffer, and K. Leo, “Highly Efficient Organic Devices Based on Electrically Doped Transport Layers”, *Chem. Rev.*, vol. 107, no. 4, p. 1233, 2007.

[9] R. Meerheim, K. Walzer, M. Pfeiffer, and K. Leo, "Ultrastable and efficient red organic light emitting diodes with doped transport layers", *Appl. Phys. Lett.*, vol. 89, no. 6, p. 061111, 2006.

[10] H. Shirakawa, E. J. Louis, A. G. MacDiarmid, C. K. Chiang, and A. J. Heeger, "Synthesis of Electrically Conducting Organic Polymers: Halogen Derivatives of Polyacetylene, (CH_x)", *J.C.S. Chem. Comm.*, p. 578, 1977.

[11] T. D. Anthopoulos and T. S. Shafai, "Oxygen induced p-doping of alpha-nickel phthalocyanine vacuum sublimed films: Implication for its use in organic photovoltaics", *Appl. Phys. Lett.*, vol. 82, no. 10, p. 1628, 2003.

[12] A. Twarowski, "Oxygen doping of zinc phthalocyanine thin films", *J. Chem. Phys.*, vol. 77, no. 11, p. 5840, 1982.

[13] S. Chen, Y. Fang, S. Hou, C. Lin, C. Lin, W. Chang, and T. Chou, "The effect of doping iodine on organic light-emitting diode", *Org. Electron.*, vol. 6, no. 2, p. 92, 2005.

[14] Y. Yamamoto, K. Yoshino, and Y. Inuishi, "Electrical Properties of Phthalocyanine-Halogen Complexes", *J. Phys. Soc. Jpn.*, vol. 47, p. 1887, 1979.

[15] L. S. Hung, C. W. Tang, and M. G. Mason, "Enhanced electron injection in organic electroluminescence devices using an Al/LiF electrode", *Appl. Phys. Lett.*, vol. 70, no. 2, p. 152, 1997.

[16] J. Kido, K. Nagai, and Y. Okamoto, "Bright organic electroluminescent devices with double-layer cathode", *IEEE Trans. Electron Devices*, vol. 40, no. 7, p. 1342, 1993.

[17] G. Parthasarathy, C. Shen, A. Kahn, and S. R. Forrest, "Lithium doping of semiconducting organic charge transport materials", *J. Appl. Phys.*, vol. 89, no. 9, p. 4986, 2001.

[18] J. Kido and T. Matsumoto, "Bright organic electroluminescent devices having a metal-doped electron-injecting layer", *Appl. Phys. Lett.*, vol. 73, no. 20, p. 2866, 1998.

[19] F. Beniere, S. Haridoss, J. Louboutin, M. Aldissi, and J. Fabre, "Doping of polyacetylene by diffusion of iodine", *J. Phys. Chem. Solids*, vol. 42, no. 8, p. 649, 1981.

[20] S. Wang, K. Kanai, E. Kawabe, Y. Ouchi, and K. Seki, "Enhanced electron injection into tris(8-hydroxyquinoline) aluminum (Alq_3) thin films by tetrathianaphthacene (TTN) doping revealed by current-voltage characteristics", *Chem. Phys. Lett.*, vol. 423, p. 170, 2006.

[21] C. K. Chan and A. Kahn, "N-doping of pentacene by decamethylcobaltocene", *Appl. Phys. A*, vol. 95, no. 1, p. 7, 2009.

[22] M. Maitrot, G. Guillaud, B. Boudjema, J. J. Andre, and J. Simon, "Molecular material-based junctions: Formation of a Schottky contact with metallophthalocyanine thin films doped by the cosublimation method", *J. Appl. Phys.*, vol. 60, no. 7, p. 2396, 1986.

[23] J. Meyer, S. Hamwi, S. Schmale, T. Winkler, H.-H. Johannes, T. Riedl, and W. Kowalsky, "A strategy towards p-type doping of organic materials with HOMO levels beyond 6 eV using tungsten oxide", *J. Mater. Chem.*, vol. 19, p. 702, 2008.

[24] W. Gao and A. Kahn, "Electronic structure and current injection in zinc phthalocyanine doped with tetrafluorotetracyanoquinodimethane: Interface versus bulk effects", *Org. Electron.*, vol. 3, no. 2, p. 53, 2002.

[25] J. Huang, M. Pfeiffer, A. Werner, J. Blochwitz, K. Leo, and S. Liu, "Low-voltage organic electroluminescent devices using pin structures", *Appl. Phys. Lett.*, vol. 80, no. 1, p. 139, 2002.

[26] J. Blochwitz, M. Pfeiffer, T. Fritz, and K. Leo, "Low voltage organic light emitting diodes featuring doped phthalocyanine as hole transport material", *Appl. Phys. Lett.*, vol. 73, no. 6, p. 729, 1998.

[27] M.-H. Ho, T.-M. Chen, P.-C. Yeh, S.-W. Hwang, and C. H. Chen, "Highly efficient p-i-n white organic light emitting devices with tandem structure", *Appl. Phys. Lett.*, vol. 91, no. 23, p. 233507, 2007.

[28] D.-S. Leem, H.-D. Park, J.-W. Kang, J.-H. Lee, J. W. Kim, and J.-J. Kim, "Low driving voltage and high stability organic light-emitting diodes with rhenium oxide-doped hole transporting layer", *Appl. Phys. Lett.*, vol. 91, no. 1, p. 011113, 2007.

[29] L. Li, M. Guan, G. Cao, Y. Li, and Y. Zeng, "Highly efficient and stable organic light-emitting diodes employing MoO_3-doped perylene-3, 4, 9, 10-tetracarboxylic dianhydride as hole injection layer", *Appl. Phys. A*, vol. 99, no. 1, p. 251, 2010.

[30] S. D. Cai, C. H. Gao, D. Y. Zhou, W. Gu, and L. S. Liao, "Study of Hole-Injecting Properties in Efficient, Stable, and Simplified Phosphorescent Organic Light-Emitting Diodes by Impedance Spectroscopy", *ACS Appl. Mater. Interfaces*, vol. 4, no. 1, p. 312, 2012.

[31] K. Yamae, H. Tsuji, V. Kittichungchit, N. Ide, and T. Komoda, "66.2: Invited paper: Highly efficient white oleds with over 100 lm/w for general lighting", *SID Symposium Digest of Technical Papers*, vol. 44, no. 1, p. 916, 2013.

[32] W.-J. Shin, J.-Y. Lee, J. C. Kim, T.-H. Yoon, T.-S. Kim, and O.-K. Song, "Bulk and interface properties of molybdenum trioxide-doped hole transporting layer in organic light-emitting diodes", *Org. Electron.*, vol. 9, no. 3, p. 333, 2008.

[33] P. Pingel, R. Schwarzl, and D. Neher, "Effect of molecular p-doping on hole density and mobility in poly(3-hexylthiophene)", *Appl. Phys. Lett.*, vol. 100, no. 14, p. 143303, 2012.

[34] Y. Zhang, B. de Boer, and P. W. M. Blom, "Controllable molecular doping and charge transport in solution-processed polymer semiconducting layers", *Adv. Funct. Mater.*, vol. 19, no. 12, p. 1901, 2009.

[35] J.-H. Lee, H.-M. Kim, K.-B. Kim, R. Kabe, P. Anzenbacher, and J.-J. Kim, "Homogeneous dispersion of organic p-dopants in an organic semiconductor as an origin of high charge generation efficiency", *Appl. Phys. Lett.*, vol. 98, no. 17, p. 173303, 2011.

[36] M. Kröger, S. Hamwi, J. Meyer, T. Riedl, W. Kowalsky, and A. Kahn, "P-type doping of organic wide band gap materials by transition metal oxides: A case-study on Molybdenum trioxide", *Org. Electron.*, vol. 10, no. 5, p. 932, 2009.

[37] S. Hamwi, J. Meyer, T. Winkler, T. Riedl, and W. Kowalsky, "P-type doping efficiency of MoO_3 in organic hole transport materials", *Appl. Phys. Lett.*, vol. 94, no. 25, p. 253307, 2009.

[38] M. Lehnhardt, S. Hamwi, M. Hoping, J. Reinker, T. Riedl, and W. Kowalsky, "Charge carrier densities in chemically doped organic semiconductors verified by two independent techniques", *Appl. Phys. Lett.*, vol. 96, no. 19, p. 193301, 2010.

[39] V. Coropceanu, J. Cornil, D. A. da Silva Filho, Y. Olivier, R. Silbey, and J.-L. Brédas, "Charge Transport in Organic Semiconductors", *Chem. Rev.*, vol. 107, no. 4, p. 926, 2007.

[40] H. Bässler and A. Köhler, "Charge Transport in Organic Semiconductors", *Top. Curr. Chem.*, vol. 312, p. 1, 2012.

[41] N. I. Craciun, J. Wildeman, and P. W. M. Blom, "Universal Arrhenius Temperature Activated Charge Transport in Diodes from Disordered Organic Semiconductors", *Phys. Rev. Lett.*, vol. 100, p. 056601, 2008.

[42] H. Bässler, "Charge transport in disordered organic photoconductors a monte carlo simulation study", *Phys. Status Solidi B*, vol. 175, no. 1, p. 15, 1993.

[43] A. Miller and E. Abrahams, "Impurity Conduction at Low Concentrations", *Phys. Rev.*, vol. 120, p. 745, 1960.

[44] I. I. Fishchuk, A. Kadashchuk, H. Bässler, and M. Abkowitz, "Low-field charge-carrier hopping transport in energetically and positionally disordered organic materials", *Phys. Rev. B*, vol. 70, p. 245212, 2004.

[45] Y. Gartstein and E. Conwell, "High-field hopping mobility in molecular systems with spatially correlated energetic disorder", *Chem. Phys. Lett.*, vol. 245, p. 351, 1995.

[46] I. I. Fishchuk, V. I. Arkhipov, A. Kadashchuk, P. Heremans, and H. Bässler, "Analytic model of hopping mobility at large charge carrier concentrations in disordered organic semiconductors: Polarons versus bare charge carriers", *Phys. Rev. B*, vol. 76, p. 045210, 2007.

[47] I. I. Fishchuk, A. K. Kadashchuk, J. Genoe, M. Ullah, H. Sitter, T. B. Singh, N. S. Sariciftci, and H. Bässler, "Temperature dependence of the charge carrier mobility in disordered organic semiconductors at large carrier concentrations", *Phys. Rev. B*, vol. 81, p. 045202, 2010.

[48] M. Grundmann, *The Physics of Semiconductors*. 1st Ed. , Springer , New York, 2006.

[49] M. Kühn, "Korrelation morphologischer und elektronischer Eigenschaften von dotierten organischen Halbleitersystemen", diploma thesis, TU Darmstadt, 2012.

[50] I. Salzmann, G. Heimel, S. Duhm, M. Oehzelt, P. Pingel, B. M. George, A. Schnegg, K. Lips, R.-P. Blum, A. Vollmer, and N. Koch, "Intermolecular Hybridization Governs Molecular Electrical Doping", *Phys. Rev. Lett.*, vol. 108, p. 035502, 2012.

[51] S. Olthof, W. Tress, R. Meerheim, B. Lussem, and K. Leo, "Photoelectron spectroscopy study of systematically varied doping concentrations in an organic semiconductor layer using a molecular p-dopant", *J. Appl. Phys.*, vol. 106, no. 10, p. 103711, 2009.

[52] K. Harada, M. Riede, K. Leo, O. R. Hild, and C. M. Elliott, "Pentacene homojunctions: Electron and hole transport properties and related photovoltaic responses", *Phys. Rev. B*, vol. 77, p. 195212, 2008.

[53] J.-H. Lee, D.-S. Leem, H.-J. Kim, and J.-J. Kim, "Effectiveness of p-dopants in an organic hole transporting material", *Appl. Phys. Lett.*, vol. 94, no. 12, p. 123306, 2009.

[54] H. Ishii, K. Sugiyama, E. Ito, and K. Seki, "Energy Level Alignment and Interfacial Electronic Structures at Organic/Metal and Organic/Organic Interfaces", *Adv. Mater.*, vol. 11, no. 8, p. 605, 1999.

[55] Y. Gao, "Surface analytical studies of interfaces in organic semiconductor devices", *Mater. Sci. Eng., R*, vol. 68, no. 3, p. 39, 2010.

[56] S. Y. Kim, W. S. Jeon, T. J. Park, R. Pode, J. Jang, and J. H. Kwon, "Low voltage efficient simple p-i-n type electrophosphorescent green organic light-emitting devices", *Appl. Phys. Lett.*, vol. 94, no. 13, p. 133303, 2009.

[57] C.-C. Chang, M.-T. Hsieh, J.-F. Chen, S.-W. Hwang, and C. H. Chen, "Highly power efficient organic light-emitting diodes with a p-doping layer", *Appl. Phys. Lett.*, vol. 89, no. 25, p. 253504, 2006.

[58] J.-H. Lee, D.-S. Leem, and J.-J. Kim, "Effect of host organic semiconductors on electrical doping", *Org. Electron.*, vol. 11, no. 3, p. 486, 2010.

[59] T. Matsushima, Y. Kinoshita, and H. Murata, "Formation of ohmic hole injection by inserting an ultrathin layer of molybdenum trioxide between indium tin oxide and organic hole-transporting layers", *Appl. Phys. Lett.*, vol. 91, no. 25, p. 253504, 2007.

[60] A. Mityashin, Y. Olivier, T. Van Regemorter, C. Rolin, S. Verlaak, N. G. Martinelli, D. Beljonne, J. Cornil, J. Genoe, and P. Heremans, "Unraveling the Mechanism of Molecular Doping in Organic Semiconductors", *Adv. Mater.*, vol. 24, no. 12, p. 1535, 2012.

[61] C. Kittel, *Introduction to solid state physics*. 8th Ed., Wiley-VCH, Weinheim, 2004.

[62] D. Nanova, S. Beck, A. Fuchs, T. Glaser, C. Lennartz, W. Kowalsky, A. Pucci, and M. Kröger, "Charge transfer in thin films of donor-acceptor complexes studied by infrared spectroscopy", *Org. Electron.*, vol. 13, no. 7, p. 1237, 2012.

[63] E. F. Aziz, A. Vollmer, S. Eisebitt, W. Eberhardt, P. Pingel, D. Neher, and N. Koch, "Localized Charge Transfer in a Molecularly Doped Conducting Polymer", *Adv. Mater.*, vol. 19, no. 20, p. 3257, 2007.

[64] K.-F. Braun and S. W. Hla, "Charge transfer in the TCNQ-sexithiophene complex", *J. Chem. Phys.*, vol. 129, no. 6, p. 064707, 2008.

[65] F. Jäckel, U. G. E. Perera, V. Iancu, K.-F. Braun, N. Koch, J. P. Rabe, and S.-W. Hla, "Investigating Molecular Charge Transfer Complexes with a Low Temperature Scanning Tunneling Microscope", *Phys. Rev. Lett.*, vol. 100, p. 126102, 2008.

[66] P. Pingel, L. Zhu, K. S. Park, J.-O. Vogel, S. Janietz, E.-G. Kim, J. P. Rabe, J.-L. Brédas, and N. Koch, "Charge-Transfer Localization in Molecularly Doped Thiophene-Based Donor Polymers", *J. Phys. Chem. Lett.*, vol. 1, no. 13, p. 2037, 2010.

[67] T. Mayer, C. Hein, E. Mankel, W. Jägermann, M. M. Müller, and H.-J. Kleebe, "Fermi level positioning in organic semiconductor phase mixed composites: The internal interface charge transfer doping model", *Org. Electron.*, vol. 13, no. 8, p. 1356, 2012.

[68] V. I. Arkhipov, P. Heremans, E. V. Emelianova, G. J. Adriaenssens, and H. Bässler, "Charge carrier mobility in doped semiconducting polymers", *Appl. Phys. Lett.*, vol. 82, no. 19, p. 3245, 2003.

[69] S. Olthof, S. Mehraeen, S. K. Mohapatra, S. Barlow, V. Coropceanu, J.-L. Brédas, S. R. Marder, and A. Kahn, "Ultralow Doping in Organic Semiconductors: Evidence of Trap Filling", *Phys. Rev. Lett.*, vol. 109, p. 176601, 2012.

[70] V. I. Arkhipov, P. Heremans, E. V. Emelianova, G. J. Adriaenssens, and H. Bässler, "Weak-field carrier hopping in disordered organic semiconductors: the effects of deep traps and partly filled density-of-states distribution", *J. Phys.: Condens. Matter*, vol. 14, no. 42, p. 9899, 2002.

[71] R. Coehoorn, W. F. Pasveer, P. A. Bobbert, and M. A. J. Michels, "Charge-carrier concentration dependence of the hopping mobility in organic materials with Gaussian disorder", *Phys. Rev. B*, vol. 72, p. 155206, 2005.

[72] W. F. Pasveer, J. Cottaar, C. Tanase, R. Coehoorn, P. A. Bobbert, P. W. M. Blom, D. M. de Leeuw, and M. A. J. Michels, "Unified description of charge-carrier mobilities in disordered semiconducting polymers", *Phys. Rev. Lett.*, vol. 94, p. 206601, 2005.

[73] V. I. Arkhipov, P. Heremans, E. V. Emelianova, and H. Bässler, "Effect of doping on the density-of-states distribution and carrier hopping in disordered organic semiconductors", *Phys. Rev. B*, vol. 71, p. 045214, 2005.

[74] M. Schwörer and H. C. Wolf, *Organic Molecular Solids*. 1st Ed., Wiley-VCH, Weinheim, 2006.

[75] S. Tokito, K. Noda, and Y. Taga, "Metal oxides as a hole-injecting layer for an organic electroluminescent device", *J. Phys. D*, vol. 29, no. 11, p. 2750, 1996.

[76] Y. Han, D. Yanfeng, Z. Zhiqiang, and M. Dongge, "Improved performances of organic light-emitting diodes with metal oxide as anode buffer", *J. Appl. Phys.*, vol. 101, p. 026105, 2007.

[77] Z. B. Wang, M. G. Helander, J. Qiu, Z. W. Liu, M. T. Greiner, and Z. H. Lu, "Direct hole injection in to 4,4'-N,N'-dicarbazole-biphenyl: A simple pathway to achieve efficient organic light emitting diodes", *J. Appl. Phys.*, vol. 108, no. 2, p. 024510, 2010.

[78] C.-W. Chen, Y.-J. Lu, C.-C. Wu, E. H.-E. Wu, C.-W. Chu, and Y. Yang, "Effective connecting architecture for tandem organic light-emitting devices", *Appl. Phys. Lett.*, vol. 87, no. 24, p. 241121, 2005.

[79] C. Girotto, E. Voroshazi, D. Cheyns, P. Heremans, and B. P. Rand, "Solution-Processed MoO_3 Thin Films As a Hole-Injection Layer for Organic Solar Cells", *ACS Appl. Mater. Interfaces*, vol. 3, no. 9, p. 3244, 2011.

[80] Y. Kinoshita, R. Takenaka, and H. Murata, "Independent control of open-circuit voltage of organic solar cells by changing film thickness of moo_3 buffer layer", *Appl. Phys. Lett.*, vol. 92, no. 24, p. 243309, 2008.

[81] J. Meyer and A. Kahn, "Electronic structure of molybdenum-oxide films and associated charge injection mechanisms in organic devices", *J. Photon. Energy.*, vol. 1, no. 1, p. 011109, 2011.

[82] J. Meyer, S. Hamwi, M. Kröger, W. Kowalsky, T. Riedl, and A. Kahn, "Transition Metal Oxides for Organic Electronics: Energetics, Device Physics and Applications", *Adv. Mater.*, vol. 24, no. 40, p. 5408, 2012.

[83] M. Kröger, S. Hamwi, J. Meyer, T. Riedl, W. Kowalsky, and A. Kahn, "Role of the deep-lying electronic states of MoO_3 in the enhancement of hole-injection in organic thin films", *Appl. Phys. Lett.*, vol. 95, no. 12, p. 123301, 2009.

[84] H. Kanno, R. J. Holmes, Y. Sun, S. Kena-Cohen, and S. R. Forrest, "White Stacked Electrophosphorescent Organic Light-Emitting Devices Employing MoO_3 as a Charge-Generation Layer", *Adv. Mater.*, vol. 18, no. 3, p. 339, 2006.

[85] X. Qi, N. Li, and S. R. Forrest, "Analysis of metal-oxide-based charge generation layers used in stacked organic light-emitting diodes", *J. Appl. Phys.*, vol. 107, no. 1, p. 014514, 2010.

[86] G. E. Jabbour, B. Kippelen, N. R. Armstrong, and N. Peyghambarian, "Aluminum based cathode structure for enhanced electron injection in electroluminescent organic devices", *Appl. Phys. Lett.*, vol. 73, no. 9, p. 1185, 1998.

[87] R. Steim, F. R. Kogler, and C. J. Brabec, "Interface materials for organic solar cells", *J. Mater. Chem.*, vol. 20, p. 2499, 2010.

[88] J. Lee, Y. Park, S. K. Lee, E.-J. Cho, D. Y. Kim, H. Y. Chu, H. Lee, L.-M. Do, and T. Zyung, "Tris-(8-hydroxyquinoline)aluminum-based organic light-emitting devices with Al/CaF_2 cathode: Performance enhancement and interface electronic structures", *Appl. Phys. Lett.*, vol. 80, no. 17, p. 3123, 2002.

[89] Y. Park, J. Lee, S. K. Lee, and D. Y. Kim, "Photoelectron spectroscopy study of the electronic structures of Al/MgF_2/tris-(8-hydroxyquinoline) aluminum interfaces", *Appl. Phys. Lett.*, vol. 79, no. 1, p. 105, 2001.

[90] K. Ihm, T.-H. Kang, K.-J. Kim, C.-C. Hwang, Y.-J. Park, K.-B. Lee, B. Kim, C.-H. Jeon, C.-Y. Park, K. Kim, and Y.-H. Tak, "Band bending of LiF/Alq_3 interface in organic light-emitting diodes", *Appl. Phys. Lett.*, vol. 83, no. 14, p. 2949, 2003.

[91] H. Heil, J. Steiger, S. Karg, M. Gastel, H. Ortner, H. von Seggern, and M. Stößel, "Mechanisms of injection enhancement in organic light-emitting diodes through an Al/LiF electrode", *J. Appl. Phys.*, vol. 89, no. 1, p. 420, 2001.

[92] Z. T. Xie, W. H. Zhang, B. F. Ding, X. D. Gao, Y. T. You, Z. Y. Sun, X. M. Ding, and X. Y. Hou, "Interfacial reactions at Al/LiF and LiF/Al", *Appl. Phys. Lett.*, vol. 94, no. 6, p. 063302, 2009.

[93] M. Pfeiffer, K. Leo, X. Zhou, J. Huang, M. Hofmann, A. Werner, and J. Blochwitz-Nimoth, "Doped organic semiconductors: Physics and application in light emitting diodes", *Org. Electron.*, vol. 4, p. 89, 2003.

[94] Y. Sun and S. R. Forrest, "Organic light emitting devices with enhanced outcoupling via microlenses fabricated by imprint lithography", *J. Appl. Phys.*, vol. 100, no. 7, p. 073106, 2006.

[95] R. Bathelt, D. Buchhauser, C. Gärditz, R. Paetzold, and P. Wellmann, "Light extraction from OLEDs for lighting applications through light scattering", *Org. Electron.*, vol. 8, no. 4, p. 293, 2007.

[96] J. Meyer, S. Hamwi, T. Bulow, H.-H. Johannes, T. Riedl, and W. Kowalsky, "Highly efficient simplified organic light emitting diodes", *Appl. Phys. Lett.*, vol. 91, no. 11, p. 113506, 2007.

[97] B. Martini, "Studien zur Realisierung einer nanoskopischen organischen Leuchtdiode auf der Spitze einer Rasterkraftsonde", diploma thesis, TU München, 2012.

[98] D. B. Williams and C. B. Carter, *Transmission Electron Microscopy: A Textbook for Materials Science*. 2nd Ed., Springer, New York, 2009.

[99] R. F. Egerton, "Electron energy-loss spectroscopy in the TEM", *Rep. Prog. Phys.*, vol. 72, no. 1, p. 016502, 2009.

[100] R. Egerton and M. Malac, "EELS in the TEM", *J. Electron. Spectrosc. Relat. Phenom.*, vol. 143, p. 43, 2005.

[101] G. Kothleitner and F. Hofer, "Optimization of the Signal to Noise Ratio in EFTEM Elemental Maps with Regard to Different Ionization Edge Types", *Micron*, vol. 29, no. 5, p. 349, 1998.

[102] R. Egerton, *Electron Energy-Loss Spectroscopy in the Electron Microscope*. 2nd Ed., Springer, New York, 1996.

[103] C. Jeanguillaume, P. Trebbia, and C. Colliex, "About the use of electron energy-loss spectroscopy for chemical mapping of thin foils with high spatial resolution", *Ultramicroscopy*, vol. 3, p. 237, 1978.

[104] M. Pfannmöller, H. Flügge, G. Benner, I. Wacker, C. Sommer, M. Hanselmann, S. Schmale, H. Schmidt, F. A. Hamprecht, T. Rabe, W. Kowalsky, and R. R. Schröder, "Visualizing a Homogeneous Blend in Bulk Heterojunction Polymer Solar Cells by Analytical Electron Microscopy", *Nano Letters*, vol. 11, no. 8, p. 3099, 2011.

[105] J. Frank, *Electron Tomography: Methods for Three-Dimensional Visualization of Structures in the Cell*. 2nd Ed., Springer, New York, 2010.

[106] B. Goris, S. Bals, W. V. den Broek, J. Verbeeck, and G. V. Tendeloo, "Exploring different inelastic projection mechanisms for electron tomography", *Ultramicroscopy*, vol. 111, no. 8, p. 1262, 2011.

[107] I. Kazantsev, "The weighted backprojection techniques of image reconstruction", *Lecture Notes in Comput. Sci.*, vol. 970, p. 521, 1995.

[108] M. Radermacher, *Weighted Back-projection Methods. In: Electron Tomography: Three-Dimensional Imaging with the Transmission Electron Microscope (Mathematical Concepts and Methods in Science and Engineering)*. Plenum Press, New York, 1992.

[109] A. Lawrence, J. C. Bouwer, G. Perkins, and M. H. Ellisman, "Transform-based backprojection for volume reconstruction of large format electron microscope tilt series", *J. Struct. Biol.*, vol. 154, no. 2, p. 144, 2006.

[110] D. Donhauser, M. Pfannmöller, L. Dieterle, K. Schultheiß, R. R. Schröder, W. Kowalsky, and M. Kröger, "Observation of Filamentous Nanostructures in Organic-Inorganic Composite Thin Films Deposited by Co-Evaporation", *Adv. Funct. Mater.*, vol. 23, no. 17, p. 2130, 2012.

[111] L. Reimer, U. Zepke, J. Moesch, S. Schulze-Hillert, M. Ross-Messmer, and W. Probst, *EELS-Spectroscopy: A Reference Handbook of Standard Data for Identification and Interpretation of Electron Energy Loss Spectra and for Generation of Electron Spectroscopic Images*. Carl Zeiss, Electron Optics Division , Oberkochen, 1992.

[112] T. Glaser, *Infrarotspektroskopische Untersuchung der p-Dotierung organischer Halbleiter mit Übergangsmetalloxiden*. PhD thesis, Universität Heidelberg, 2012.

[113] M. P. Seah and W. A. Dench, "Quantitative electron spectroscopy of surfaces: A standard data base for electron inelastic mean free paths in solids", *Surf. Interface Anal.*, vol. 1, no. 1, p. 2, 1979.

[114] E. Mankel, *Elektronische Eigenschaften von Heterosystemen organischer und anorganischer Halbleiter: Präparation, Modifikation und Charakterisierung von Grenzflächen und Kompositen*. PhD thesis, TU Darmstadt, 2011.

[115] C. Hein, *Anpassung der elektronischen Struktur an organischen Heterokontakten*. PhD thesis, TU Darmstadt, 2012.

[116] J. Maibach, *Preparation and Characterization of Solution Processed Organic Semiconductor Interfaces: Electronic properties of thiophene fullerene based donor acceptor systems*. PhD thesis, TU Darmstadt, 2013.

[117] R. Lovrinčić, *Über die Bestimmung der dynamischen Leitfähigkeit dünner Metallfilme auf der (1 0 0)-Diamantoberfläche mittels Infrarot-Spektroskopie*. PhD thesis, University of Heidelberg, 2009.

[118] T. Glaser, S. Beck, B. Lunkenheimer, D. Donhauser, A. Köhn, M. Kröger, and A. Pucci, "Infrared study of the MoO_3 doping efficiency in 4,4'-bis(N-carbazolyl)-1,1'-biphenyl (CBP)", *Org. Electron.*, vol. 14, no. 2, p. 575, 2013.

[119] C. C. Wu, C. I. Wu, J. C. Sturm, and A. Kahn, "Surface modification of indium tin oxide by plasma treatment: An effective method to improve the efficiency, brightness, and reliability of organic light emitting devices", *Appl. Phys. Lett.*, vol. 70, no. 11, p. 1348, 1997.

[120] J. Berkowitz, M. G. Inghram, and W. A. Chupka, "Polymeric Gaseous Species in the Sublimation of Molybdenum Trioxide", *J. Chem. Phys.*, vol. 26, p. 842, 1957.

[121] S. Hamwi, *Transition Metal Oxides in Organic Light Emitting Diodes*. PhD thesis, TU Braunschweig, 2010.

[122] M. A. Baldo, M. E. Thompson, and S. R. Forrest, "High-efficiency fluorescent organic light-emitting devices using a phosphorescent sensitizer", *Nature*, vol. 403, p. 750, 2000.

[123] G. J. McGraw, D. L. Peters, and S. R. Forrest, "Organic vapor jet printing at micrometer resolution using microfluidic nozzle arrays", *Appl. Phys. Lett.*, vol. 98, no. 1, p. 013302, 2011.

[124] J.-W. Kang, S.-H. Lee, H.-D. Park, W.-I. Jeong, K.-M. Yoo, Y.-S. Park, and J.-J. Kim, "Low roll-off of efficiency at high current density in phosphorescent organic light emitting diodes", *Appl. Phys. Lett.*, vol. 90, no. 22, p. 223508, 2007.

[125] J. Meyer, R. Khalandovsky, P. Görrn, and A. Kahn, "MoO_3 Films Spin-Coated from a Nanoparticle Suspension for Efficient Hole-Injection in Organic Electronics", *Adv. Mater.*, vol. 23, no. 1, p. 70, 2011.

[126] C.-T. Lin, C.-H. Yeh, M.-H. Chen, S.-H. Hsu, C.-I. Wu, and T.-W. Pi, "Influences of evaporation temperature on electronic structures and electrical properties of molybdenum oxide in organic light emitting devices", *J. Appl. Phys.*, vol. 107, no. 5, p. 053703, 2010.

[127] J. Meyer, A. Shu, M. Kröger, and A. Kahn, "Effect of contamination on the electronic structure and hole-injection properties of MoO_3/organic semiconductor interfaces", *Appl. Phys. Lett.*, vol. 96, no. 13, p. 133308, 2010.

[128] M. C. Gwinner, R. D. Pietro, Y. Vaynzof, K. J. Greenberg, P. K. H. Ho, R. H. Friend, and H. Sirringhaus, "Doping of Organic Semiconductors Using Molybdenum Trioxide: a Quantitative Time-Dependent Electrical and Spectroscopic Study", *Adv. Funct. Mater.*, vol. 21, no. 8, p. 1432, 2011.

[129] S. D. Ha, J. Meyer, and A. Kahn, "Molecular-scale properties of MoO_3-doped pentacene", *Phys. Rev. B*, vol. 82, p. 155434, 2010.

[130] Published with the kind permission of John Wiley and Sons from Ref. [110].

[131] J.-H. Lee, H.-M. Kim, K.-B. Kim, and J.-J. Kim, "Origin of charge generation efficiency of metal oxide p-dopants in organic semiconductors", *Org. Electron.*, vol. 12, no. 6, p. 950, 2011.

[132] W. Ma, C. Yang, and A. J. Heeger, "Spatial Fourier-Transform Analysis of the Morphology of Bulk Heterojunction Materials Used in Plastic Solar Cells", *Adv. Mater.*, vol. 19, no. 10, p. 1387, 2007.

[133] D. Wang, D. S. Su, and R. Schlögl, "Electron Beam Induced Transformation of MoO_3 to MoO_2 and a New Phase MoO", *Z. Anorg. Allg. Chem.*, vol. 630, no. 7, p. 1007, 2004.

[134] S. P. Pennycook and P. D. Nellist, *Scanning Transmission Electron Microscopy: Imaging and Analysis*. Springer, New York, 2011.

[135] B. Goris, T. Roelandts, K. J. Batenburg, H. H. Mezerji, and S. Bals, "Advanced reconstruction algorithms for electron tomography: From comparion to combination", *Ultramicroscopy*, vol. 127, p. 40, 2013.

[136] X. Huang, H.-J. Zhai, B. Kiran, and L.-S. Wang, "Observation of d-Orbital Aromaticity", *Angew. Chem. Int. Ed.*, vol. 44, no. 44, p. 7251, 2005.

[137] H. Ibach, *Physics of Surfaces and Interfaces*. Springer, New York, 2006.

[138] F. Schreiber, "Organic molecular beam deposition: Growth studies beyond the first monolayer", *Phys. Status Solidi A*, vol. 201, no. 6, p. 1037, 2004.

[139] X. Qiao, J. Chen, X. Li, and D. Ma, "Observation of hole hopping via dopant in moo_x-doped organic semiconductors: Mechanism analysis and application for high performance organic light-emitting devices", *J. Appl. Phys.*, vol. 107, no. 10, p. 104505, 2010.

[140] A. Müller-Brand, "Development of a Cryostat System and Its Subsequent Operation in Temperature-Dependent Conductivity Measurements on MoO_3-Doped CBP", Master's thesis, University of Heidelberg, 2013.

[141] M. Gölz, "Untersuchung der elektrischen Eigenschaften von MoO_3-dotieren CBP-Dünnfilmen", Master's thesis, University of Heidelberg, 2013.

[142] S. Günes, H. Neugebauer, and N. S. Sariciftci, "Conjugated Polymer-Based Organic Solar Cells", *Chem. Rev.*, vol. 107, no. 4, p. 1324, 2007.

[143] T. Matsushima and C. Adachi, "Enhancing hole transports and generating hole traps by doping organic hole-transport layers with p-type molecules of 2,3,5,6-tetrafluoro-7,7,8,8-tetracyanoquinodimethane", *Thin Solid Films*, vol. 517, no. 2, p. 874, 2008.

[144] K. R. Choudhury, J.-h. Yoon, and F. So, "LiF as an n-Dopant in Tris(8-hydroxyquinoline) Aluminum Thin Films", *Adv. Mater.*, vol. 20, no. 8, p. 1456, 2008.

[145] K.-H. Yim, G. L. Whiting, C. E. Murphy, J. J. M. Halls, J. H. Burroughes, R. H. Friend, and J.-S. Kim, "Controlling Electrical Properties of Conjugated Polymers via a Solution-Based p-Type Doping", *Adv. Mater.*, vol. 20, no. 17, p. 3319, 2008.

[146] D. T. Duong, C. Wang, E. Antono, M. F. Toney, and A. Salleo, "The chemical and structural origin of efficient p-type doping in P3HT", *Org. Electron.*, vol. 14, no. 5, p. 1330, 2013.

[147] Y. Zhao, K. H. An, S. Chen, B. O'Connor, K. P. Pipe, and M. Shtein, "Localized Current Injection and Submicron Organic Light-Emitting Device on a Pyramidal Atomic Force Microscopy Tip", *Nano Lett.*, vol. 7, no. 12, p. 3645, 2007.

[148] I. Vladimirov, "Entwicklung eines Nahfeld-Rastersondenmikroskops auf Grundlage Organischer Leuchtdioden", diploma thesis, University of Heidelberg, 2011.

[149] D. Roessler and W. Walker, "Electronic spectrum of crystalline lithium fluoride", *J. Phys. Chem. Solids*, vol. 28, no. 8, p. 1507, 1967.

[150] V. Shrotriya, G. Li, Y. Yao, C.-W. Chu, and Y. Yang, "Transition metal oxides as the buffer layer for polymer photovoltaic cells", *Appl. Phys. Lett.*, vol. 88, no. 7, p. 073508, 2006.

[151] T. Boutboul, A. Akkerman, A. Breskin, and R. Chechik, "Electron inelastic mean free path and stopping power modelling in alkali halides in the 50 eV-10 keV energy range", *J. Appl. Phys.*, vol. 79, no. 9, p. 6714, 1996.

[152] K. Robbie, J. Brett, and A. Lakhtakia, "Chiral sculptured thin films", *Nature*, vol. 384, p. 616, 1996.

[153] K. Robbie and M. J. Brett, "Sculptured thin films and glancing angle deposition: Growth mechanics and applications", *J. Vac. Sci. Technol. A*, vol. 15, no. 3, p. 1460, 1997.

[154] Y.-P. Zhao, D.-X. Ye, G.-C. Wang, and T.-M. Lu, "Novel Nano-Column and Nano-Flower Arrays by Glancing Angle Deposition", *Nano Lett.*, vol. 2, no. 4, p. 351, 2002.

[155] M. Scherer, R. Saive, D. Daume, M. Kröger, and W. Kowalsky, "Sample preparation for scanning Kelvin probe microscopy studies on cross sections of organic solar cells", *AIP Advances*, vol. 3, no. 9, p. 092134, 2013.

[156] P. Favia, E. Voroshazi, P. Heremans, and H. Bender, "Investigation of aged organic solar cell stacks by cross-sectional transmission electron microscopy coupled with elemental analysis", *J. Mater. Sci.*, vol. 48, no. 7, p. 2908, 2013.

[157] N. Rujisamphan, F. Deng, R. E. Murray, C. Ni, and S. I. Shah, "Focused ion beam assisted investigations of Al interface in polythiophene:Fullerene solar cells", *Sol. Energ. Mat. Sol.*, vol. 109, p. 56, 2013.

[158] S. W. Tsang, S. K. So, and J. B. Xu, "Application of admittance spectroscopy to evaluate carrier mobility in organic charge transport materials", *J. Appl. Phys.*, vol. 99, no. 1, p. 013706, 2006.

[159] P. M. Borsenberger, "Hole transport in tri-p-tolylamine-doped bisphenol-A-polycarbonate", *J. Appl. Phys.*, vol. 68, no. 12, p. 6263, 1990.

[160] R. U. A. Khan, D. Poplavskyy, T. Kreouzis, and D. D. C. Bradley, "Hole mobility within arylamine-containing polyfluorene copolymers: A time-of-flight transient-photocurrent study", *Phys. Rev. B*, vol. 75, p. 035215, 2007.

[161] G. Juška, K. Arlauskas, M. Viliūnas, and Kočka, "Extraction Current Transients: New Method of Study of Charge Transport in Microcrystalline Silicon", *Phys. Rev. Lett.*, vol. 84, p. 4946, 2000.

[162] A. J. Mozer, N. S. Sariciftci, L. Lutsen, D. Vanderzande, R. Österbacka, M. Westerling, and G. Juška, "Charge transport and recombination in bulk heterojunction solar cells studied by the photoinduced charge extraction in linearly increasing voltage technique", *Appl. Phys. Lett.*, vol. 86, no. 11, p. 112104, 2005.

[163] J.-F. Chang, T. Sakanoue, Y. Olivier, T. Uemura, M.-B. Dufourg-Madec, S. G. Yeates, J. Cornil, J. Takeya, A. Troisi, and H. Sirringhaus, "Hall-Effect Measurements Probing the Degree of Charge-Carrier Delocalization in Solution-Processed Crystalline Molecular Semiconductors", *Phys. Rev. Lett.*, vol. 107, p. 066601, 2011.

[164] S. D. Ha and A. Kahn, "Isolated molecular dopants in pentacene observed by scanning tunneling microscopy", *Phys. Rev. B*, vol. 80, p. 195410, 2009.

[165] W. Gao and A. Kahn, "Controlled p-doping of zinc phthalocyanine by coevaporation with tetrafluorotetracyanoquinodimethane: A direct and inverse photoemission study", *Appl. Phys. Lett.*, vol. 79, no. 24, p. 4040, 2001.